NAVAL POSTGRADUATE SCHOOL

MONTEREY, CALIFORNIA

THESIS

DEVELOPMENT OF A DIGITAL TRACKING ARRAY WITH SINGLE-CHANNEL RSNS AND MONOPULSE DIGITAL BEAMFORMING

by

ShihYuan Yeh

December 2010

Thesis Co-Advisors: David C. Jenn
Roberto Cristi

Approved for public release; distribution is unlimited

THIS PAGE INTENTIONALLY LEFT BLANK

REPORT DOCUMENTATION PAGE			Form Approved OMB No. 0704-0188
Public reporting burden for this collection of information is estimated to average 1 hour per response, including the time for reviewing instruction, searching existing data sources, gathering and maintaining the data needed, and completing and reviewing the collection of information. Send comments regarding this burden estimate or any other aspect of this collection of information, including suggestions for reducing this burden, to Washington headquarters Services, Directorate for Information Operations and Reports, 1215 Jefferson Davis Highway, Suite 1204, Arlington, VA 22202-4302, and to the Office of Management and Budget, Paperwork Reduction Project (0704-0188) Washington DC 20503.			
1. AGENCY USE ONLY ***(Leave blank)***	**2. REPORT DATE** December 2010	**3. REPORT TYPE AND DATES COVERED** Master's Thesis	
4. TITLE AND SUBTITLE Development of a Digital Tracking Array with Single-Channel RSNS and Monopulse Digital Beamforming		**5. FUNDING NUMBERS**	
6. AUTHOR(S) ShihYuan Yeh			
7. PERFORMING ORGANIZATION NAME(S) AND ADDRESS(ES) Naval Postgraduate School Monterey, CA 93943-5000		**8. PERFORMING ORGANIZATION REPORT NUMBER**	
9. SPONSORING /MONITORING AGENCY NAME(S) AND ADDRESS(ES) N/A		**10. SPONSORING/MONITORING AGENCY REPORT NUMBER**	
11. SUPPLEMENTARY NOTES The views expressed in this thesis are those of the author and do not reflect the official policy or position of the Department of Defense or the U.S. Government. IRB Protocol number _____.			
12a. DISTRIBUTION / AVAILABILITY STATEMENT Approved for public release; distribution is unlimited		**12b. DISTRIBUTION CODE**	

13. ABSTRACT (maximum 200 words)

Unmanned aerial vehicles (UAVs) are widely used in military applications, and one of the most common missions is remote sensing. Remote sensing requires UAVs equipped with different kinds of sensors. Information collected by remote sensors must be transmitted back to a ground control station (GCS) to conduct analysis. The majority of UAVs are controlled directly by GCS personnel using radio frequency (RF), line-of-sight (LOS) links. The ground antenna must acquire and then track the UAV signal. A digital phased array allows signal processing functions to be performed in the antenna processor as well as beamforming and tracking.

The development of a digital tracking array with single-channel robust symmetrical number system (RSNS) and monopulse digital beamforming (DBF) to track a UAV's transmitted signal is described in this thesis. The RSNS is used as the direction finding (DF) algorithm and can provide high angle resolution with two closely spaced elements. However, as is typical for an array, the angle accuracy is reduced at the two ends of the field-of-view (FOV). The monopulse DBF is used to precisely track the signals. The monopulse tracking technique provides precise angle accuracy within a FOV of approximately $\pm 45^{\circ}$. The tracking system is developed in LabView, and the performance of a six-element prototype array is demonstrated by measurement in an anechoic chamber.

14. SUBJECT TERMS UAV, Direction Finding, RSNS, Monopulse Tracking, Digital Tracking Array, Phased Array, Digital Beamforming			**15. NUMBER OF PAGES** 133
			16. PRICE CODE
17. SECURITY CLASSIFICATION OF REPORT Unclassified	**18. SECURITY CLASSIFICATION OF THIS PAGE** Unclassified	**19. SECURITY CLASSIFICATION OF ABSTRACT** Unclassified	**20. LIMITATION OF ABSTRACT** UU

NSN 7540-01-280-5500 Standard Form 298 (Rev. 2-89)
Prescribed by ANSI Std. 239-18

THIS PAGE INTENTIONALLY LEFT BLANK

Approved for public release; distribution is unlimited

DEVELOPMENT OF A DIGITAL TRACKING ARRAY WITH SINGLE-CHANNEL RSNS AND MONOPULSE DIGITAL BEAMFORMING

ShihYuan Yeh
Major, Taiwan Army (Chung-Shan Institute of Science & Technology)
B.S., National Defense University (Chung Cheng Institute of Technology), 2001

Submitted in partial fulfillment of the
requirements for the degree of

MASTER OF SCIENCE IN ELECTRICAL ENGINEERING

from the

NAVAL POSTGRADUATE SCHOOL
December 2010

Author: ShihYuan Yeh

Approved by: David C. Jenn
Thesis Co-Advisor

Roberto Cristi
Thesis Co-Advisor

R. Clark Robertson
Chairman, Department of Electrical and Computer Engineering

THIS PAGE INTENTIONALLY LEFT BLANK

ABSTRACT

Unmanned aerial vehicles (UAVs) are widely used in military applications, and one of the most common missions is remote sensing. Remote sensing requires UAVs equipped with different kinds of sensors. Information collected by remote sensors must be transmitted back to a ground control station (GCS) to conduct analysis. The majority of UAVs are controlled directly by GCS personnel using radio frequency (RF), line-of-sight (LOS) links. The ground antenna must acquire and then track the UAV signal. A digital phased array allows signal processing functions to be performed in the antenna processor as well as beamforming and tracking.

The development of a digital tracking array with single-channel robust symmetrical number system (RSNS) and monopulse digital beamforming (DBF) to track a UAV's transmitted signal is described in this thesis. The RSNS is used as the direction finding (DF) algorithm and can provide high angle resolution with two closely spaced elements. However, as is typical for an array, the angle accuracy is reduced at the two ends of the field-of-view (FOV). The monopulse DBF is used to precisely track the signals. The monopulse tracking technique provides precise angle accuracy within a FOV of approximately $\pm 45^{\circ}$. The tracking system is developed in LabView, and the performance of a six-element prototype array is demonstrated by measurement in an anechoic chamber.

THIS PAGE INTENTIONALLY LEFT BLANK

TABLE OF CONTENTS

LIST OF FIGURES

THIS PAGE INTENTIONALLY LEFT BLANK

LIST OF TABLES

THIS PAGE INTENTIONALLY LEFT BLANK

EXECUTIVE SUMMARY

This thesis is a continuation of the previous research on a digital tracking array. The objective of this project was to design, build and test a six-element phased array using robust symmetrical number system (RSNS) direction finding (DF) and monopulse digital beamforming (DBF) tracking. The tracking system was designed to have the ability to accurately acquire the transmitted signals from a unmanned aerial vehicle (UAV) and track the video signal source continuously. There are two parts to this thesis. The first illustrates the RSNS DF algorithm and demonstrates the concept with hardware tests. The theory of the RSNS DF algorithm is explained and the hardware simulation is described. In the second portion angle tracking techniques are examined, different types of tracking systems are considered and the RSNS DF with monopulse DBF tracking system is implemented. The theory of the tracking system is described, and the results of the tracking system demonstration are provided. The hardware components are commercial off-the-shelf (COTS) items to lower cost. Simulations are implemented in MATLAB and the calibration, control, data acquisition and beamforming modules are built using LabView software.

The first task simulated and validated the RSNS algorithms used in DF. The implementation was for the single-channel RSNS DF system. The received baseband in-phase (I) and quadrature (Q) signals were recovered by direct downconversion demodulation. A bench top setup for the RSNS DF method was used to measure angle-of-arrival (AOA) and then to conduct comparisons between the measured and true values (from the vector network analyzer (VNA)). The analysis was performed to assess the impact of noise on the AOA estimates. Different signal-to-noise ratios (SNRs) from 10 dB to 90 dB in increments of 20 dB were examined to see which SNR values were acceptable for the DF accuracy.

In the second task, angle tracking techniques were investigated, different types of tracking systems were examined, and the RSNS DF and monopulse DBF tracking algorithms were implemented. A six-element phased array was used for the tracking

system demonstration. The hardware of the digital tracking array with single-channel RSNS DF and monopulse DBF was assembled and tested. The tracking system used RSNS DF to first find the rough AOA and then passed the scan angle to the monopulse DBF module to conduct continuous tracking. The tracking measurements were taken in an anechoic chamber to reduce interference from multipath, and the measured data was stored to perform offline analysis. The first test was performed to find the maximum RSNS DF field-of-view (FOV) for a variety of element phase differences (one phase difference, or averaging three phase differences or five phase differences). A FOV from -80° to 80° was tested. The second test examined the pedestal movement effects and rotation steps for 2°, 5° and 10°. Finally, a comparison of changing monopulse slope constant versus fixed monopulse slope constant was conducted.

LIST OF ACRONYMS AND ABBREVIATIONS

ADC	Analog to Digital Converter
AOA	Angle of Arrival
ATC	Air Traffic Control
COTS	Commercial off-the-shelf
DAQ	Data Acquisition
DBF	Digital Beamforming
DC	Direct Current
DF	Direction Finding
EM	Electromagnetic
EW	Electronic Warfare
FDM	Frequency-Division Multiplexing
FM	Frequency Modulation
FOV	Field of View
G	Gain
GCS	Ground Control Station
HPBW	Half-Power Beamwidth
I	In-Phase
ISR	Intelligence, Surveillance and Reconnaissance
LNA	Low Noise Amplifier
LO	Local Oscillator
LOS	Line Of Sight
LPF	Low Pass Filter
NI	National Instruments

NPS	Naval Postgraduate School
NTSC	National Television Standards Committee
PGF	Path Gain Factor
PLL	Phased Locked Loop
Q	Quadrature
RCS	Radar Cross Section
RF	Radio Frequency
RMS	Root Mean Square
RSNS	Robust Symmetrical Number System
SNR	Signal to Noise Ratio
STT	Single Target Tracker
T/R	Transmit/Receive
TWS	Track While Scan
UAV	Unmanned Aerial Vehicle
VNA	Vector Network Analyzer

ACKNOWLEDGMENTS

First, I would like to thank my thesis advisor, Professor David C. Jenn, without whose help I could not write a single page. Next, I would like to thank my thesis co-advisor, Professor Roberto Cristi, without whose help I would not graduate on time. Finally, I would like to thank Robert Broadston, Director of the Microwave Laboratory, without whose help the hardware would remain software.

THIS PAGE INTENTIONALLY LEFT BLANK

I. INTRODUCTION

A. BACKGROUND

Unmanned aerial vehicles (UAVs) are operated indirectly by pilots and widely used in military applications such as reconnaissance, intelligence, electronic attack, strike, destruction of enemy air defense, communications relay and combat search. In Figure 1, a MQ-9 Reaper UAV is shown. It is equipped with hellfire missiles, laser guided bombs (GBU-12) and a 20 inch gimbal (AN/AAS-52) in the front of the plane fuselage. It provides continual intelligence, surveillance and reconnaissance (ISR) capability and also carries out over-the-horizon, medium-altitude and long-continuance weapons delivery, fully loaded, for up to 14 hours [1]. Besides these military applications, UAVs are also used for civil purposes such as border protection, traffic monitoring, firefighting and search and rescue. Using UAVs can avoid infringing on pilot safety and save costs when compared to traditional airplane employment [2].

Figure 1. MQ-9 Reaper (from [1]).

Among the applications carried out by UAVs, one of the most common missions is remote sensing. Remote sensing requires UAVs equipped with different kinds of sensors for different purposes, such as infrared motion cameras, picture cameras, laser

rangefinders, designators, illuminators and so on. Information collected by remote sensors must be transmitted back to a ground control station (GCS) to conduct advanced analysis by ground personnel. Some information requires significant bandwidth, such as video streams [1].

A few types of UAVs are flown by pre-programmed flight plans and receive GPS signals to navigate. The majority of UAVs are controlled directly by GCS personnel using radio frequency (RF) line-of-sight (LOS) links or using satellites to relay communication signals. In Figure 2, an illustrative diagram of communication signals between a UAV and a GCS is depicted. It is critical that the link between the GCS and UAV provides a high bandwidth, reliable and secure connection.

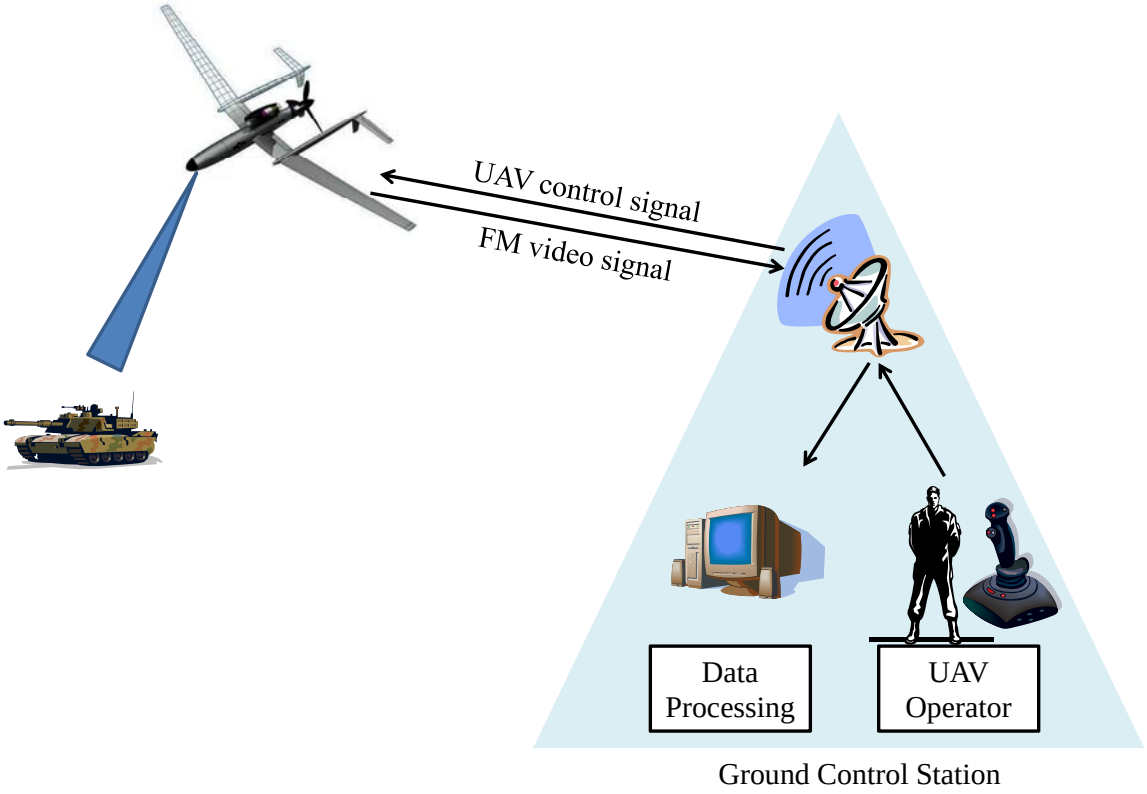

Figure 2. Communication and data link between a UAV and GCS.

To satisfy the requirements mentioned above, the ground antenna must first acquire and then track the UAV signal. Phased arrays are prime candidates for this

application. In particular, a digital phased array would allow signal processing functions to be performed in the antenna processor, as well as beamforming and tracking.

Digital phased arrays are collections of a number of individual antennas arranged to produce a directional radiation pattern. In Figure 3, a block diagram of the components and architecture of a digital phased array is depicted. Each array element has an individual transmit/receive (T/R) module [3]. By adjusting phase, a digital phased array can point its main beam electronically to a desired azimuth or elevation angle without actually moving or rotating an antenna. Further, steering the main beam to the signal source can reduce interference and improve signal-to-noise ratio (SNR). The phase shifting of each array element is controlled by the digital beamformer (DBF) which allows the array to scan at the speed of the processor. With this characteristic it becomes possible to track multiple signals in a sequential (time-shared) manner [4].

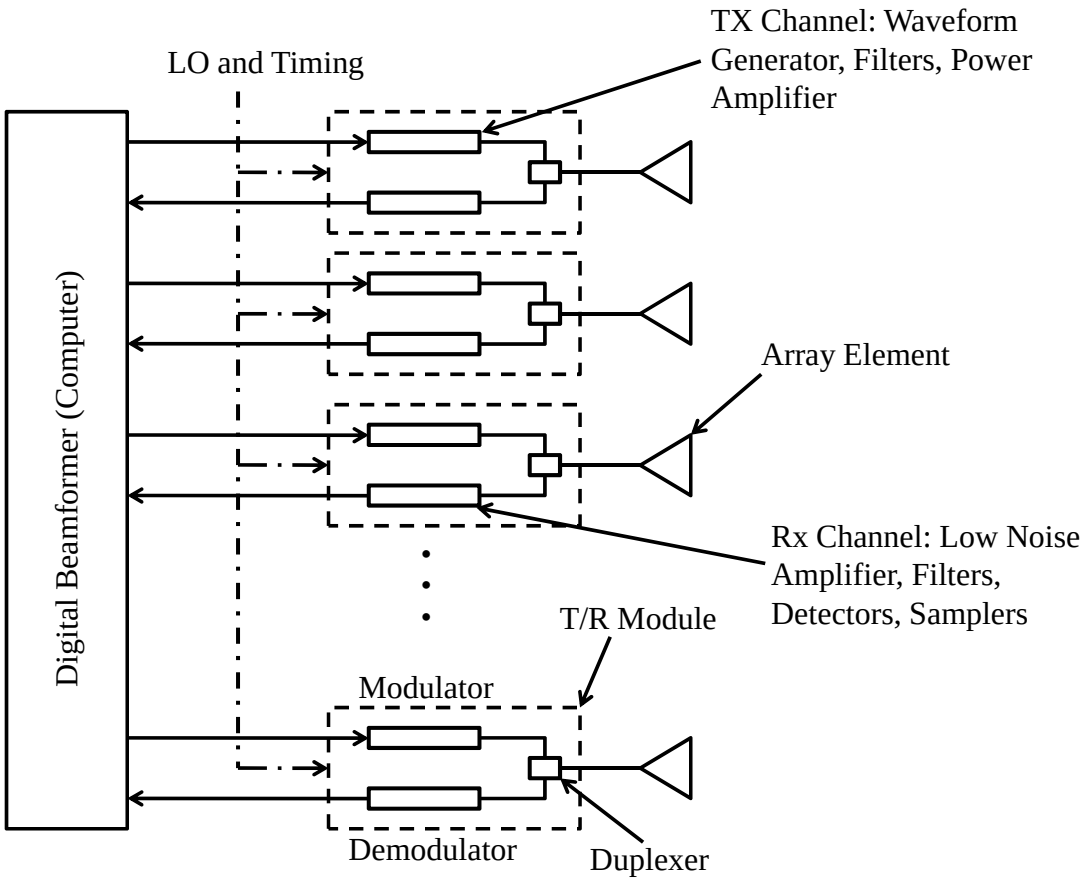

Figure 3. Components and architecture of digital phased arrays (from [5]).

Besides the advantages mentioned above, there are several others that can be illustrated. First, traditional analog antenna processing is based on integrals but digital phased arrays can be analyzed using simple summations. It is easier to design summation circuitry than integration circuitry [4]. Second, new solid-state transmitters are more convenient to integrate into digital phased arrays. Third, it is easier to control beam shapes and half-power beamwidth (HPBW) in digital processing. Fourth, with a proper design, a lower radar cross section (RCS) is possible [4].

Despite the many advantages, there are limitations and concerns associated with digital phased array implementations. Of note, digital phased arrays have a greater degree of complexity and a higher cost when compared to traditional antenna systems. Additionally, there are other issues of concern, like bandwidth limitations and mutual coupling between elements [3].

Passive direction finding (DF) is a technique that can be used for initial signal acquisition. It has been widely used in a variety of fields such as communication, navigation and electronic warfare (EW). It is a method used to receive an electromagnetic (EM) wave which comes from a signal source or target and then calculate the angle-of-arrival (AOA). Different DF algorithms can achieve different angle resolutions. Even using the same DF algorithm but with different parameters can lead to different results. The goal is to use a DF algorithm that optimizes angle resolution, accuracy, and can resolve ambiguities [6].

Note that DF is used to derive the AOA but not the range to an emitter. This is unlike a common radar system which provides range and angle information to a target. DF systems can use high gain antennas or multiple baselines to provide better angle accuracy but then antenna size becomes prohibitive. Even without high resolution, DF has been able to recognize and identify an emitter by its general nature or behavior in space. Because of its passive receive characteristics, it alone cannot be used for tracking the range to an emitter. However, a DF method can be used cooperatively with other tracking systems to provide a military air-defense radar system [6].

After the signal is acquired by the DF algorithm, it can be tracked. Most tracking radars adopt a pencil beam to achieve high accuracy in angle resolution. Typically, the beamwidth of the pencil beam is less than a few degrees in both the azimuth and elevation planes [7]. Monopulse tracking is the most efficient technique. The receive antenna forms a difference beam, and the null of the difference beam is kept on the target by forcing the output to zero. In our design, we use a DF algorithm to get a rough AOA and then pass the scan angle to the tracker to do the monopulse tracking [7].

B. PREVIOUS WORK

The ongoing digital array project begun by Gezer [8], who designed a digital phased array to track UAVs with the use of commercial off-the-shelf (COTS) hardware, is extended in this thesis. The design of the tracking system was also verified through simulation.

Eng [9] built a calibration station that provided an easy way to measure the direct current (DC) offset of the demodulator boards, which are critical components of the digital array. The components of the calibration system were easy to disassemble, making upgrades easier to accomplish. For example, the analog-to-digital converter (ADC) could be upgraded to give better resolution.

Benveniste [10] implemented a single-channel robust symmetrical number system (RSNS) to conduct DF measurements. Several moduli sets were used and evaluated through MATLAB simulations. Results showed that there were large angle resolution errors at low SNR. Additionally, large dynamic range moduli sets can yield high angle resolutions errors when compared to small dynamic range moduli sets. He also assembled and tested bench top hardware with low noise amplifier (LNA) and demodulator boards. The system was connected to National Instruments (NI) PXI-5112 cards, and LabView software and calibration functions were evaluated.

Tan and Pandya [11] carried out the design of a UAV tracking system with the use of RSNS DF and monopulse DBF. Three different LabView modules were also developed. The first provided monopulse beamforming and tracking, the second performed frequency modulation (FM) demodulation and the third performed decoding

of the National Television Standards Committee (NTSC) video signal. The beamforming and tracking module used RSNS combined with monopulse DBF to acquire and track a UAV using a six-element antenna array. The FM demodulation module was tested successfully for a single channel. The NTSC decoding module was able to decode video signals and display them on a LabView console.

Kaya [12] improved the FM demodulation module and integrated and initiated testing of the system.

C. SCOPE OF RESEARCH

The ultimate objective of this project was to extend previous work [8-12] by designing, building and testing an array and processor with RSNS DF and monopulse DBF to accurately acquire and track a video signal source. Hardware used to implement the array and processor was built mainly from COTS components to lower cost. Simulations were implemented in MATLAB. Antenna controller software was built using LabView.

The first task was to simulate and validate the RSNS algorithms used in DF. RSNS folding waveforms and ambiguity resolution were investigated, followed by hardware design and implementation. Calibration of the demodulator boards was described briefly. A bench top setup in the Microwave Laboratory the RSNS DF method was used to measure AOA and then conduct comparisons between the measured and true values. Further, analysis was performed to assess the calculated AOA values with the impact of noise on the AOA estimates to determine which SNR values were acceptable for the DF accuracy.

The second task investigated angle tracking techniques and different types of tracking systems. Tracking accuracy factors are also explained to better understand the noise effect on the tracking system design. Then a single-channel RSNS with monopulse DBF tracking system was constructed. A six-element phased array is used for the tracking. A block diagram of the array is shown in Figure 4. All of the functions shown outside of the first block are done in the processor. Measurements in the anechoic chamber are performed to demonstrate tracking. The anechoic chamber reduces

interference, and the layout of the anechoic chamber is described in Chapter V. The tracking system uses RSNS DF first to find the initial AOA and then pass the scan angle to the monopulse DBF module to do continuous tracking.

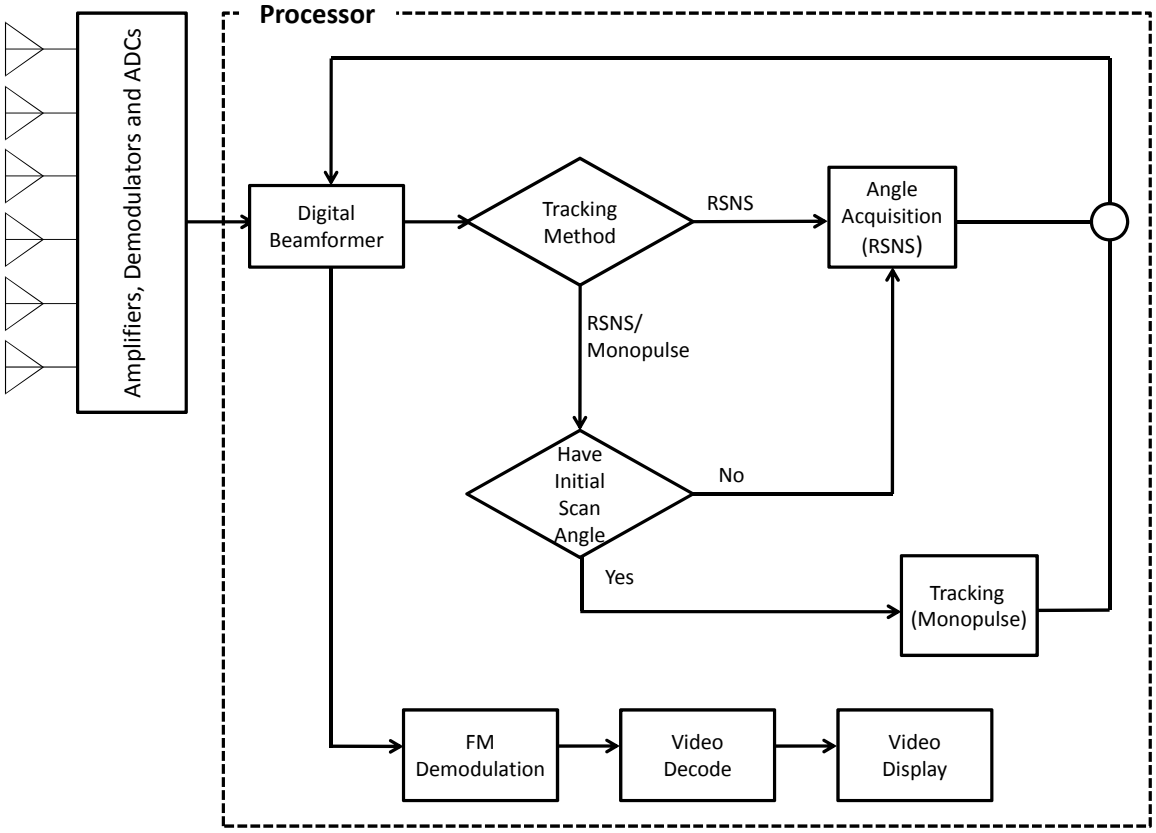

Figure 4. Structure of a six-element phased array tracking system.

Test data obtained from laboratory bench top testing and the anechoic chamber are compared to theoretical values to further refine the software modules.

D. THESIS OUTLINE

The basic principles of DF are reviewed and the RSNS folding waveforms and ambiguity are explained in Chapter II. Furthermore, quadrature demodulation and fundamental RSNS theory are explained.

Different types of tracking systems, angle tracking techniques and tracking accuracy considerations are reviewed in Chapter III.

The single-channel RSNS system design is presented and the results of MATLAB simulations conducted at different SNRs to examine tradeoffs and effects are included in Chapter IV. Moreover, the demodulator board calibration and LabView software demonstrations are covered.

Measurements of the antenna hardware in the anechoic chamber and the results are evaluated in Chapter V.

Summaries, conclusions and recommendations for future study are contained in Chapter VI.

II. DIRECTION FINDING AND ROBUST SYMMETRICAL NUMBER SYSTEM

In Section A of this chapter, three DF methods are introduced. In particular, the phase delay method used for the single-channel RSNS DF system of Chapter IV is highlighted. In Section B, signal modulation and demodulation, commonly used in communication systems, are illustrated. In Section C, the problems of ambiguity and folding waveforms are discussed. Finally, RSNS parameters are defined and an interferometer design is explained in Section D.

A. DIRECTION FINDING

Radio DF systems use phased arrays to measure AOA from an incident planar EM wave. There are three categories of DF methods: amplitude comparison, phase delay and time delay [13]. In order to perform a comparison, at least two antenna elements are required. The antenna is assumed to be operated in the far-field, and for the present discussion, the EM wave is restricted to a narrow frequency band.

The amplitude comparison method converts the amplitude responses received from antenna elements into voltages and then converts them to the AOA. Phase and time delay methods use the phase and time difference between the antenna elements, respectively, to derive AOA.

A single-channel array is shown in Figure 5. A plane wave is incident on a phased array with two linear elements separate by a distance d, referred to as the baseline. The distance between elements is determined by the required angle resolution and ambiguity issues. The antenna field-of-view (FOV) ranges from -90° to $+90^{\circ}$. The planar EM wave first arrives at antenna 2 then travels another $d\sin(\theta)$ distance to antenna 1 [10].

The output voltages from the elements are fed to direct downconversion quadrature demodulators. The waveform is translated in frequency from the carrier to

baseband (centered at 0 frequency). The in-phase (I) and quadrature (Q) components can be combined to form a complex baseband signal that contains all of the signal's amplitude and phase information [5].

After down conversion, the I and Q voltages are sampled and sent to a processor where the RSNS DF algorithm is executed.

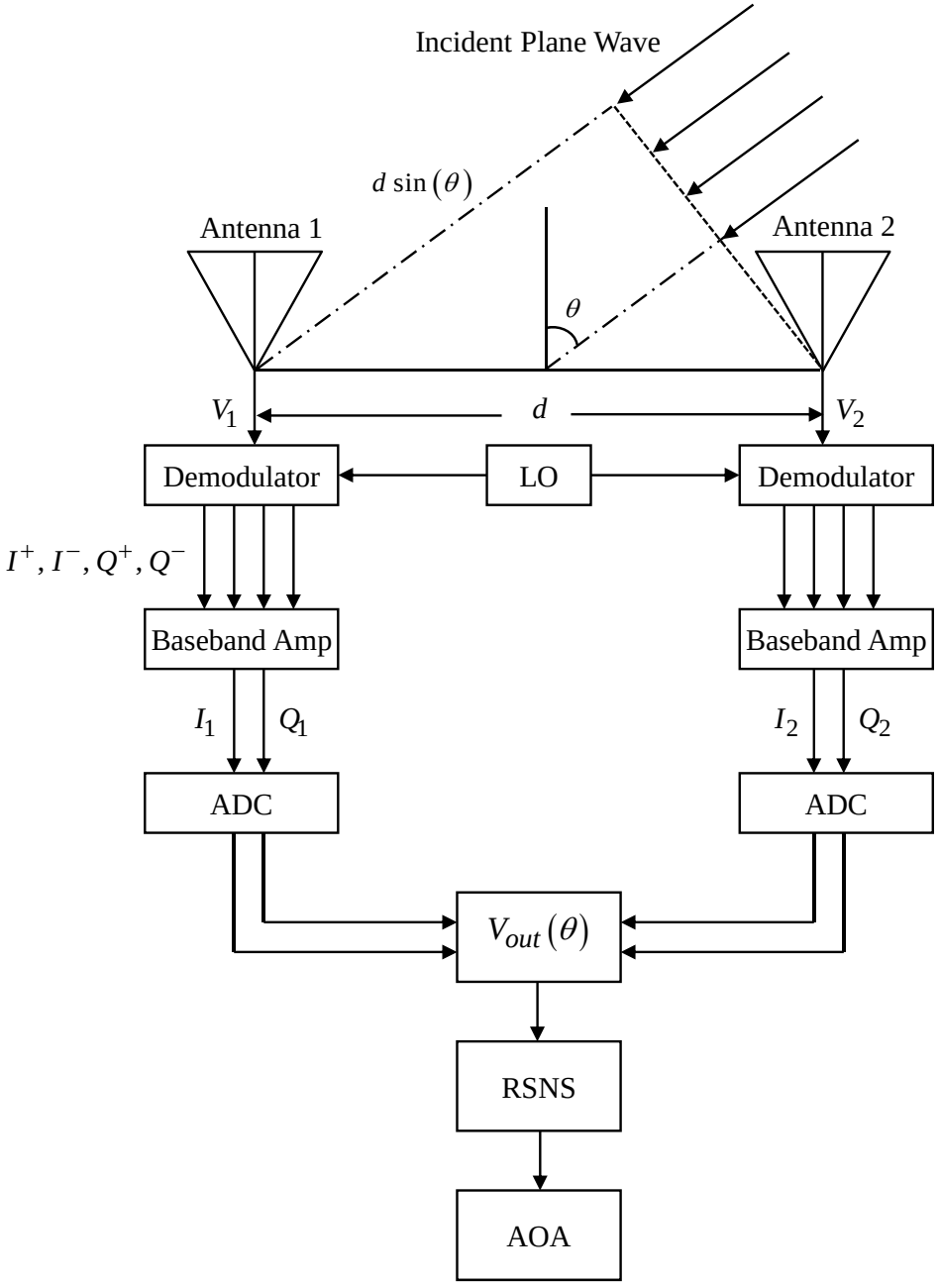

Figure 5. Incident plane wave and two-element array (after [10]).

The received signal out of the antenna element is

$$V_i = V\cos\left(\omega_c t + \psi_i + \phi_i\right) \tag{1}$$

where i indicates the antenna element number ($i = 1, 2$), $\omega_c = 2\pi f_c$ is defined as the carrier frequency, ψ_i is the phase delay from cables and ϕ_i is the path phase difference compared to the reference. In this, case antenna 1 is considered the reference.

The received signals V_i are passed to the quadrature demodulator for mixing and filtering. These steps are elaborated on in more detail in Section B. The signals out of the demodulator are I_1, Q_1, I_2 and Q_2. They are the in-phase (I_i) and quadrature (Q_i) components of the signal

$$V_i(t) = A_i(t)\cos[\omega_c t + \Phi_i(t)] = I_i(t)\cos\left(\omega_c t\right) - Q_i(t)\sin\left(\omega_c t\right) \tag{2}$$

where

$$I_i = A_i\cos\left(\Phi_i\right) \tag{3}$$

$$Q_i = A_i\sin\left(\Phi_i\right) \tag{4}$$

$$A_i = \sqrt{\left(I_i\right)^2 + \left(Q_i\right)^2} \tag{5}$$

$$\Phi_i = \tan^{-1}\left(\frac{Q_i}{I_i}\right) \tag{6}$$

A_i is the amplitude and Φ_i is the phase [5]. A plot of the I/Q relationship is shown in Figure 6.

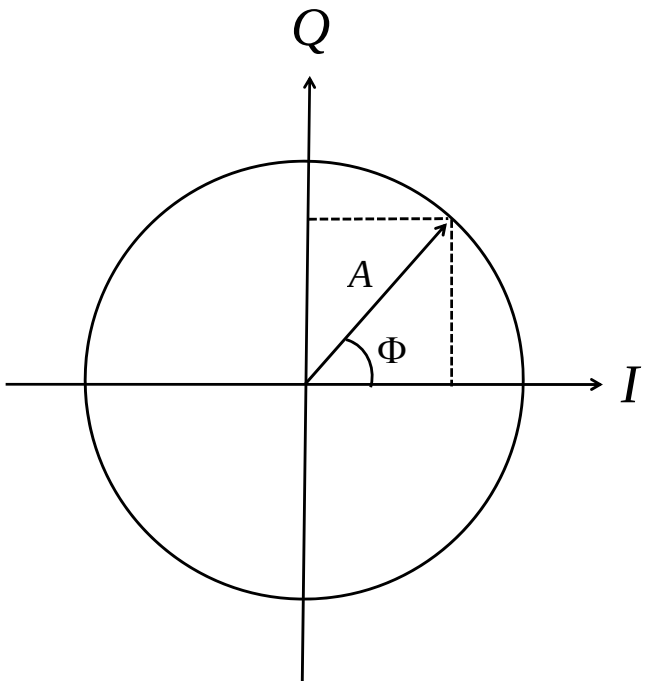

Figure 6. I/Q signal diagram (from [5]).

If we set the origin in the middle of the two antenna elements, the phase value of each element is given as $\phi_1 = -\frac{kd}{2}\sin\theta$ and $\phi_2 = \frac{kd}{2}\sin\theta$, where $k = \frac{2\pi}{\lambda}$. The phase difference is calculated as

$$\Delta\phi = \phi_2 - \phi_1 = kd\sin(\theta). \tag{7}$$

Once $\Delta\phi$ is computed, the normalized folding waveforms are obtained from the quadrature demodulator and are expressed as

$$V_{out}(\theta) = \cos(\Delta\psi + \Delta\phi) \tag{8}$$

where $\Delta\psi = \psi_2 - \psi_1$ comes from the cables. This term can be neglected because the cable lengths are known and are assumed to be equal [5]. Finally, by combining Equation (7) and (8), the phase folding waveform is simplified as

$$V_{out}(\theta) = \cos\left[kd\sin(\theta)\right]. \tag{9}$$

We see from Equation (9) that AOA can be calculated directly because k, d and V_{out} are known. However, the measurement is ambiguous unless $d < \lambda/2$, so that

$0 \le \Delta\phi \le 2\pi$. To get higher resolution, an increase in the baseline distance is necessary. When the baseline distance is increased, more ambiguities are created which cause multiple AOAs for each $\Delta\phi$. This is the reason for the phase folding waveform. A signal processing method based on a RSNS mapping can achieve a high resolution without ambiguities [14]. The details are explained in Section D.

B. QUADRATURE DEMODULATION

1. Signal Modulation

Modulation and demodulation techniques are commonly used in communication systems, such as standard broadcast radio, wireless networks and telecommunication systems. The block diagram in Figure 7 demonstrates the modulation of a sinusoid with a message signal. By modulating a sinusoid of carrier frequency ω_c with the message signal $s(t)$, we see that the modulated signal $y(t)$ can be efficiently transmitted. The inputs are the I and Q components of $s(t)$.

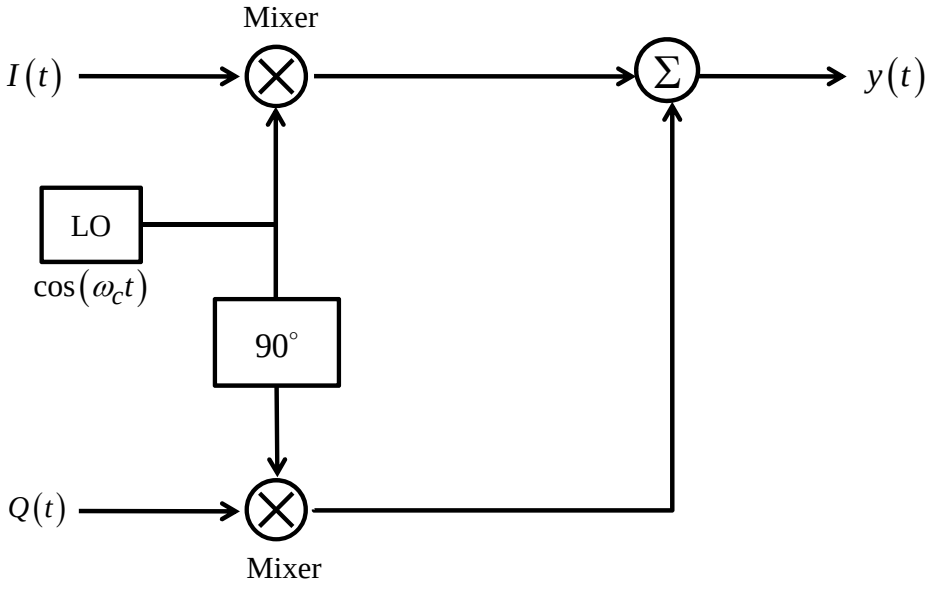

Figure 7. Modulation of a sinusoid with a message signal (after [15]).

There are three main reasons for using the modulation and demodulation process. First, baseband signals do not propagate far because frequencies at DC do not radiate. Second, it facilitates frequency-division multiplexing (FDM), where a single-channel is divided into several bandlimited sub-channels and each sub-channel modulates with a different carrier frequency. Since frequency spectrum is a limited resource, this technique is used quite often in commercial applications [16]. Third, the frequency determines the physical size of the antenna. Low frequency signals have long wavelengths and large diameter antennas are required. If the physical size of the antenna is too large, the system becomes impractical [11].

2. Quadrature Demodulation

The process of recovering the original message signal $s(t)$ is called demodulation. The emitter signal $y(t)$ at carrier frequency $\omega_c = 2\pi f_c$ is represented in I-Q form as defined in Equation (2):

$$y(t) = A(t)\cos[2\pi f_c t + \Phi(t)] = I(t)\cos(2\pi f_c t) - Q(t)\sin(2\pi f_c t). \qquad (10)$$

The $I(t)$ and $Q(t)$ components are derived using the quadrature demodulation technique [5]. The block diagram in Figure 8 shows the quadrature demodulation process. A photo of an AD8347 analog quadrature demodulator is shown in Figure 9. This device has a LO input frequency range of 0.8 GHz to 2.7 GHz, and 2.4 GHz is used in the demonstration array described in Chapter IV. The differential I and Q outputs are used to obtain the single-channel outputs $I = I^+ - I^-$ and $Q = Q^+ - Q^-$.

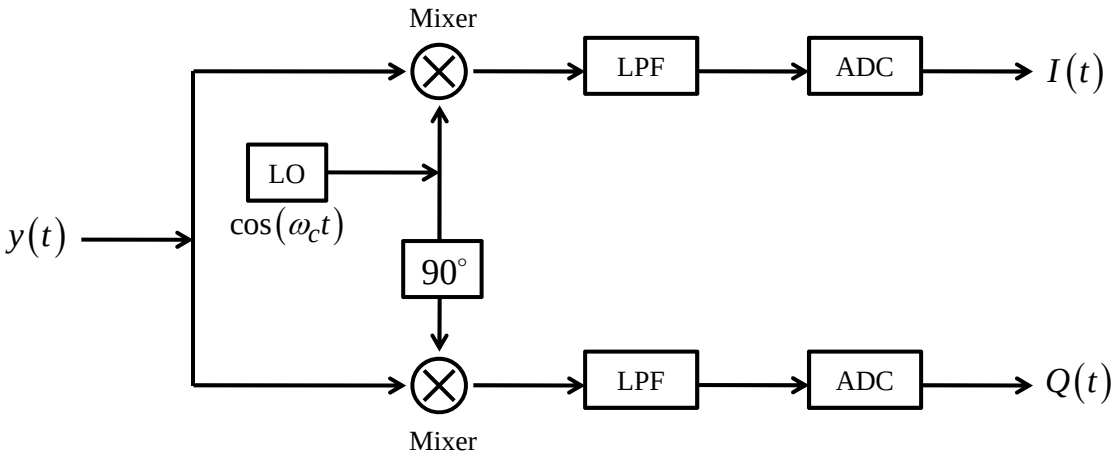

Figure 8. Quadrature demodulation process (after [5]).

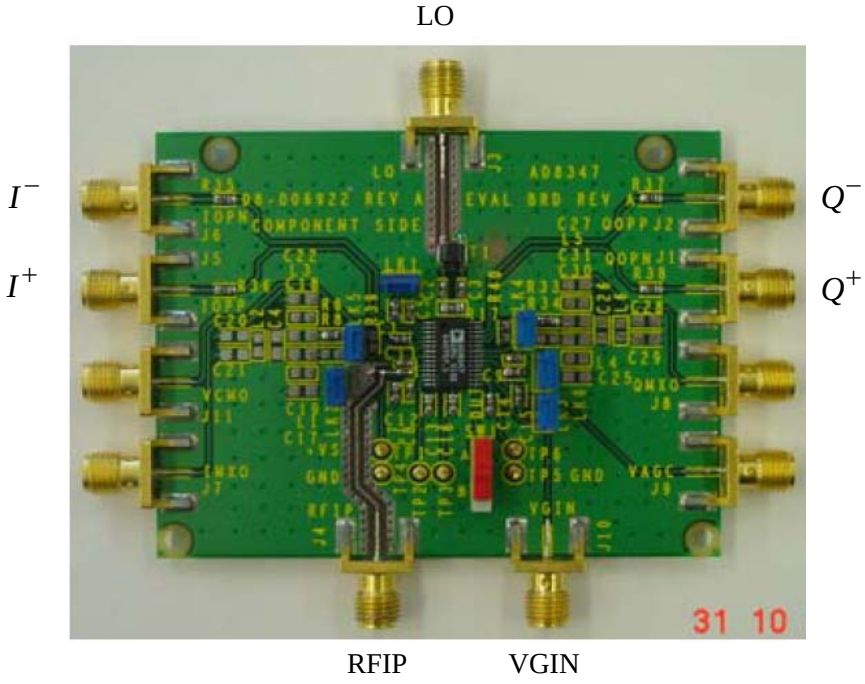

Figure 9. AD8347 quadrature demodulator made by Analog Devices, Inc. (after [5]).

The purpose of a quadrature demodulator is to transform the received signal $y(t)$ into its $I(t)$ and $Q(t)$ form. A complex envelop signal $u(t)$ is given as

$$u(t) = I(t) + jQ(t). \tag{11}$$

First, $y(t)$ is mixed with the LO signal $\cos(\omega_{LO}t)$, where for direct downconversion $\omega_{LO} = \omega_c$. The in-phase channel, from [5], is represented as

$$\mathrm{Re}\left\{\frac{u(t)}{2}e^{j(\omega_c+\omega_{LO})t}\right\} + \mathrm{Re}\left\{\frac{u(t)}{2}e^{j(\omega_c-\omega_{LO})t}\right\}. \tag{12}$$

Next, the mixed signal is passed through a low pass filter (LPF), where the term on the left side at $2\omega_c$ in Equation (12) is eliminated leaving only

$$\mathrm{Re}\left\{\frac{u(t)}{2}\right\} = \frac{I(t)}{2}. \tag{13}$$

A similar process on the second phase shifted channel gives the quadrature component

$$\mathrm{Im}\left\{\frac{u(t)}{2}\right\} = \frac{Q(t)}{2}. \tag{14}$$

C. AMBIGUITY AND FOLDING WAVEFORMS

To obtain higher resolution, the distance between antenna elements must be increased. However, if the baseline distance is increased over a half wavelength, an ambiguity problem arises. This may result in more than one solution to the AOA, thus making the true AOA indeterminate.

1. Ambiguity

From Equation (7), $\Delta\phi$ is related to wavelength, distance and AOA. However, frequency is also related to wavelength. Limits on all of these variables must be adhered to in order to avoid ambiguities.

When the antenna element spacing is equal to $\lambda/2$, $\Delta\phi = \pi\sin(\theta)$ is obtained. The plot in Figure 10 clearly shows the relationship between phase difference and AOA; one phase difference maps to one AOA. The mapping relationship is unique [17]. For example, if the phase difference is -100°, only one AOA is obtained (indicated by the "o").

However, if element spacing increases to λ, $\Delta\phi = 2\pi\sin(\theta)$ is obtained. The plot in Figure 10 shows that this one phase difference can map to two AOAs (indicated by the "x"). When the phase difference equals -100°, both -18° and 47° are possible AOAs. The mapping relationship is not unique and this phenomenon is called ambiguity [13].

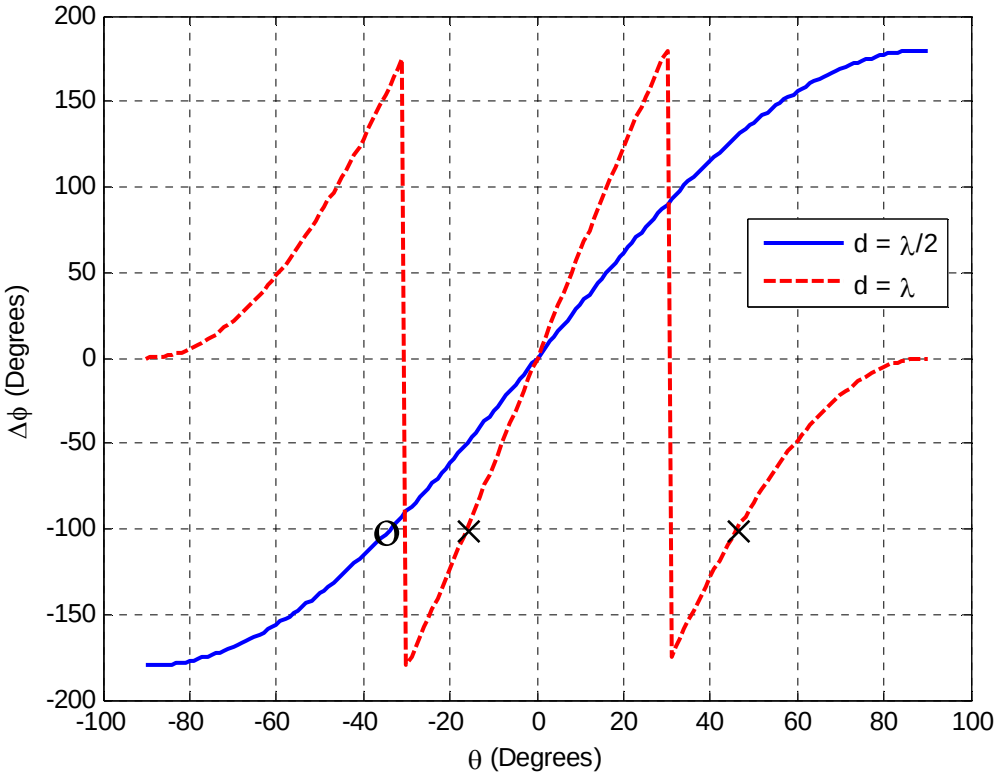

Figure 10. $\Delta\phi$ vs. AOA at $d = \lambda/2$ and $d = \lambda$ (after [10]).

Similarly, a change in frequency can cause an ambiguity [17]. For example, as demonstrated in Figure 11, if the element spacing is fixed at 0.5 m and the frequency is 300 MHz, there is no ambiguity. However, when the frequency is increased to 900 MHz, ambiguities are evident. For a phase difference equal to -100°, there are three possible AOAs.

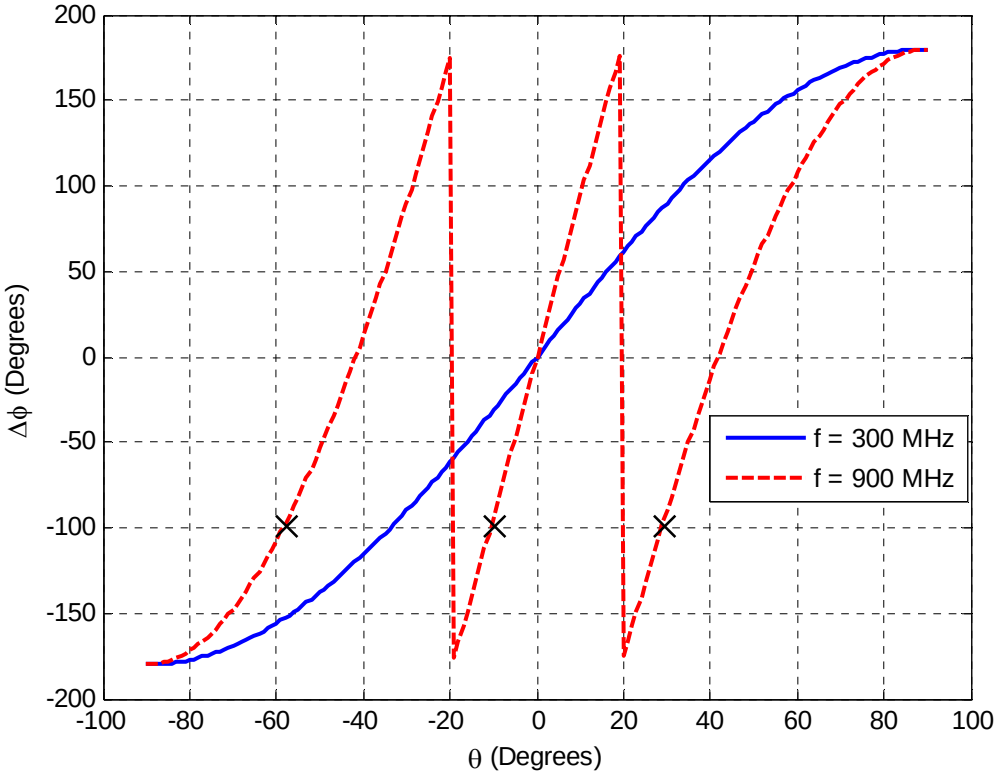

Figure 11. $\Delta\phi$ vs. AOA with fixed $d = 0.5$ m at frequencies of 300 MHz and 900 MHz.

When designing a single-channel DF system, the distance between elements, wavelength and frequency should all be taken into consideration to avoid this ambiguity phenomenon.

2. Folding Waveforms

For a two element array, the output V_{out} in Equation (8) is a folding waveform that is periodic between $\theta = \pm\pi/2$, and the number of folds is represented by

$$n = \frac{2d}{\lambda}. \tag{15}$$

From Figure 12, we see that when $d = \lambda/2$, there is only one fold (cycle) in the output waveform. This is easily verified by inspection of Equation (15). Another property is

that the folding waveform is symmetrical [14]. An increase in the baseline distance demonstrates this property. In Figure 12, there are two folds in the waveform when $d = \lambda$. Notice the symmetry about the origin.

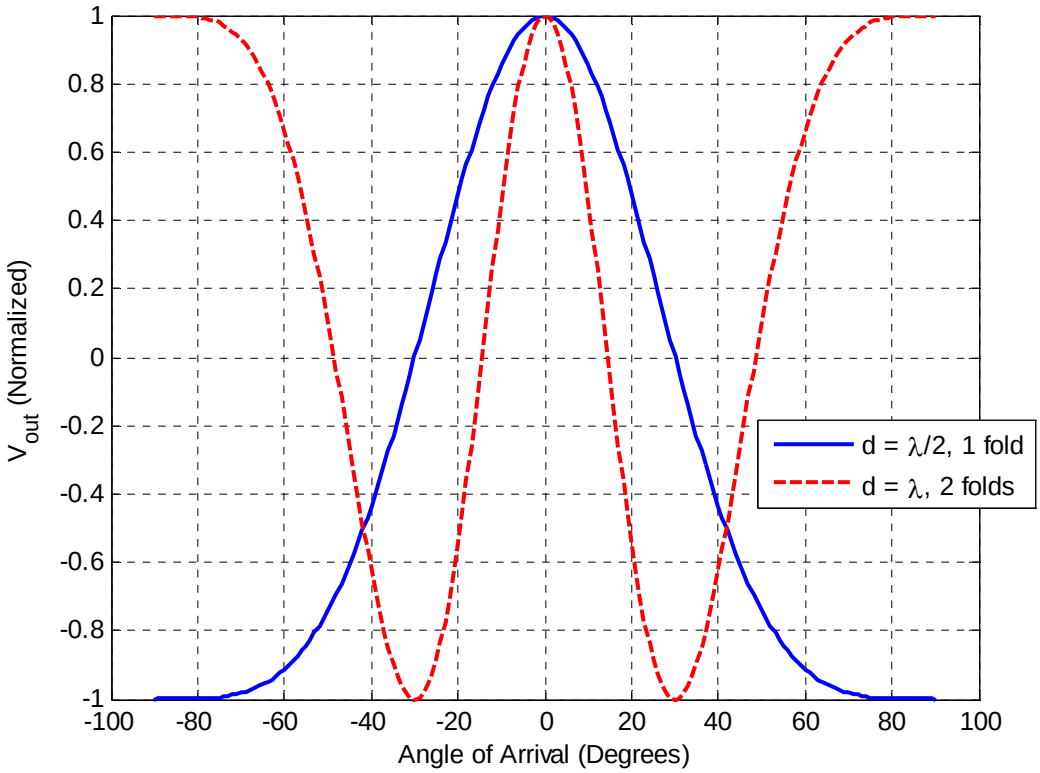

Figure 12. Output voltage vs. AOA at $d = \lambda / 2$ and $d = \lambda$ (after [10]).

To sum up, increasing the baseline distance also increases the number of folds. Thus, the number of folds can be controlled by antenna element spacing.

D. ROBUST SYMMETRICAL NUMBER SYSTEM THEORY

The concept of RSNS mapping is used to reconstruct the folding waveforms out of the antenna and obtain high resolution AOA estimates without long baseline distances. In this section, the RSNS parameters are first defined, then the DF antenna design steps are outlined.

1. RSNS Parameters

The fundamental elements of the RSNS algorithm are the moduli (m_i). They are integers greater than zero and are relatively prime. The number of moduli is related to the number of antenna elements and is denoted by N, also called the number of channels. For example, as shown in Figure 5, a two element antenna is one channel with a spacing fixed by a modulus m_1 [10].

A RSNS row vector is defined such that

$$[0,\ 1,\ 2,...,\ m_i-1,\ m_i,\ m_i-1,...,\ 2,\ 1]. \tag{16}$$

A sequence used to represent the folding waveform is constructed by repeating each element N times in the row vector represented in Equation (16). For the ith sequence $(i=1,2,...,N)$, the result should look like

$$X_{m_i}=[\underbrace{0\ ,0,...,0,0}_{N},\underbrace{1,1,...,1,1}_{N},...,\underbrace{m_i,m_i,...,m_i,m_i}_{N},...,\underbrace{1,1,...,1,1}_{N}]. \tag{17}$$

After the sequence sets are generated, they are aligned vertically and shifted one column per sub-sequence. Next, the dynamic range is defined as $\hat{M}$ and is the maximum number of contiguous column vectors of the shifted sequence set that has no repetitions. An example for $m_1=3$ and $m_2=4$ is displayed in Table 1. In this case, there is no column pair duplicated from column numbers 6 to 20, so $\hat{M}=15$ is the dynamic range [14].

Table 1. RSNS sequence for moduli [3, 4] (after [10]).

$\hat{M}$ = 15

Column Number	1	2	3	4	5	**6**	**7**	**8**	**9**	**10**	**11**	**12**	**13**	**14**	**15**	**16**	**17**	**18**	**19**	**20**	21
m_1 = 3	0	0	1	1	2	2	3	3	2	2	1	1	0	0	1	1	2	2	3	3	2
m_2 = 4	1	0	0	1	1	2	2	3	3	4	4	3	3	2	2	1	1	0	0	1	1

Previous work in [6, 8, 9, 10, 12] found that for some specific two element cases, the dynamic range can be summarized and calculated as follows:

Case 1: For $m_1 \geq 3$ and $m_2 = m_1 + 1$,

$$\hat{M} = 3\left(m_1 + m_2\right) - 6; \tag{18}$$

Case 2: For $m_1 \geq 5$ and $m_2 = m_1 + 2$,

$$\hat{M} = 3\left(m_1 + m_2\right) - 7; \tag{19}$$

Case 3: For $m_1 \geq 5$ and $m_2 = m_1 + C\left(C \geq 3\right)$,

$$\hat{M} = 4m_1 + 2m_2 - 2. \tag{20}$$

2. Interferometer Design

After the number of channels and their moduli has been selected, there are several steps needed to implement a RSNS interferometer system. The first is to calculate the number of folds for each modulus, which is given as

$$n_i = \frac{\hat{M}}{2Nm_i}. \tag{21}$$

With n_i defined, the corresponding element baseline distance can be derived. By substituting Equation (21) into Equation (15), we get a new equation for spacing given by

$$d_i = n_i \frac{\lambda}{2} = \frac{\hat{M}\lambda}{4Nm_i}. \tag{22}$$

Another issue is that the received signals from the elements degrade at wide FOV angles. Therefore, a rescaling process is adopted to alleviate this angle distortion. Only part of the FOV is used instead of the entire visible region [17]. From Equation (9), a new relationship $d\sin\left(\theta\right) = d'\sin\left(\theta'\right)$ is derived to define a scaling factor $\left(\xi\right)$, represented as

$$\xi = \frac{d'}{d} = \frac{\sin\left(\theta\right)}{\sin\left(\theta'\right)} \tag{23}$$

where d' is the scaled baseline distance. To verify the rescale effect, a smaller θ' is used in Equation (23) corresponding to a longer d'. As mentioned at the beginning of

this section, a longer baseline distance means a better AOA resolution. Further, combining Equation (22) with (23), we get a new relationship

$$d_i' = d_i \xi = \frac{\hat{M}\lambda}{4 m_i N} \xi \tag{24}$$

where d_i' is the scaled baseline distance [6].

Next, the folding waveforms are encoded out of the antenna (Equation (9)) into RSNS bins by comparing V_{out} to the thresholds given by

$$V_{j,m_i} = \cos\left(\frac{m_i - j + 0.5}{m_i} \pi \right), \quad 1 \le j \le m_i. \tag{25}$$

Folding waveforms and thresholds for $m_1 = 3$ and $m_2 = 4$ are shown in Figure 13.

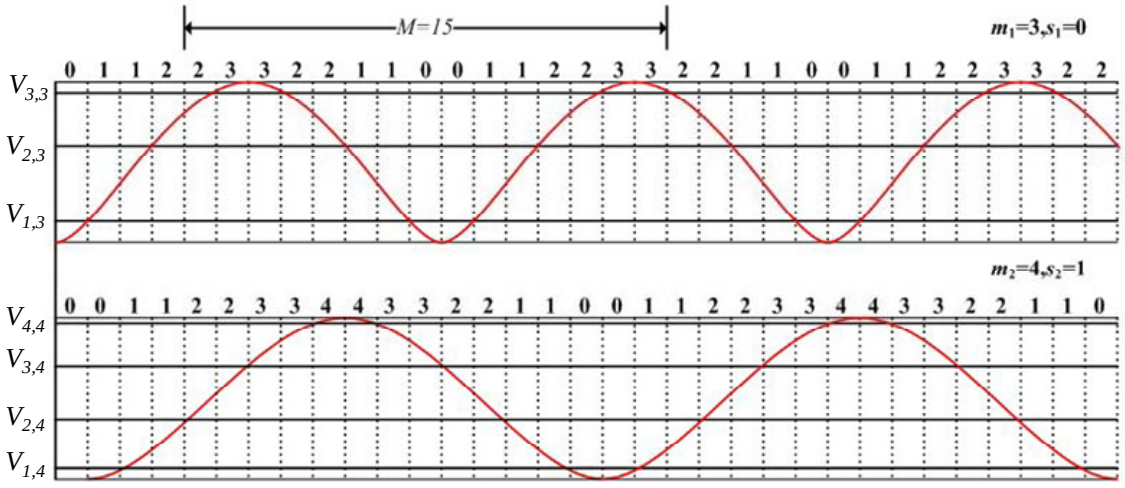

Figure 13. RSNS folding waveforms for $m_1 = 3$ and $m_2 = 4$ (from [17]).

The final step is to calculate the phase adjustment (ς_i) and align the center of the dynamic range to the folding waveforms at broadside $(\theta = 0^\circ)$ [10]. After phase adjustment, Equation (9) becomes

$$V_{out}(\theta) = \cos(kd \sin\theta + \varsigma). \tag{26}$$

In a straightforward application of the RSNS, each modulus is mapped to a separate channel (pair of elements). Since all channels can share a common reference

element, the total number of elements required for N channels is $N-1$. However, it is possible to simulate the output from multiple channels from a single pair of elements as long as the folding waveform out of the elements is unambiguous. That is, only one fold occurs in V_{out} which requires $d \leq \lambda / 2$. This approach has been called "virtual RSNS processing." This discussion has been based on the array output voltage given by Equation (9). This is referred to as the phase folding waveform because the phase difference between elements is used directly. It is possible to generate an amplitude folding waveform, which is essentially the array factor for the two elements. The amplitude waveform folds at half the rate of the phase waveform and, therefore, the spacing requirement for an unambiguous fold is $d \leq \lambda$.

A single-channel RSNS DF of moduli 5 and 9 is designed and simulated in Chapter IV. Parameters of this RSNS DF system are derived based on the theory presented earlier and on the equations described in this section.

THIS PAGE INTENTIONALLY LEFT BLANK

III. TRACKING SYSTEMS AND TECHNIQUES

Once the AOA is obtained, the digital processor can initiate the tracking algorithm. In Section A, a brief discussion of two types of tracking systems is introduced. In Section B, several candidate angle tracking techniques, such as conical scan, sequential lobing and monopulse tracking are explained with a focus on monopulse tracking. In Section C, theoretical angle accuracy is derived and several factors that affect the limitations of tracking accuracy are discussed.

A. TYPES OF TRACKING SYSTEMS

There are many applications that use tracking systems for either civilian or military purposes. In the civilian area, airports deploy air traffic control (ATC) systems to manage air traffic in the vicinity of airports. In the military area, tracking radars track target trajectory, compute the best intercept path and guide missiles to the target. The purpose of tracking in this application is to track a designated signal with continuous measurement of the angle coordinates.

1. Single-Target Tracker (STT)

The proposed digital phased array design is essentially a STT. The STT continuously tracks a signal with a high rate of observation frequency. Observation rate depends on how many times the source signal is observed within a period. Typically, 10 observations per second are enough to maintain track on a UAV emitter. A STT with a closed-loop tracker obtains the angle error signal and keeps adjusting the tracker to minimize the angle error. Similarly, the proposed algorithm is a closed loop technique. The accuracy of tracking is not as major a concern as it is for a radar application. It is only necessary that the UAV stay roughly in the array main beam to avoid a significant loss in gain [4].

2. Phased Array Radar Tracking

Phased array radars can track multiple targets by steering beams electronically in different directions. In digital phased arrays, computers are used to quickly switch beams in multiple directions in different time frames. They have the advantage of high observation rate, as in STT, plus the capability of multiple-target tracking. The disadvantage is the complexity associated with analog beamforming, where each array element must contain a phase shifter, duplexer and T/R module [11]. A typical phased array radar (AN/SPY-1D) on an Aegis platform is shown in Figure 14. It is able to perform search, track and missile guidance functions with a capability of simultaneously tracking over 100 targets.

Figure 14. AN/SPY-1D (from [18]).

B. ANGLE TRACKING TECHNIQUES

Angle tracking techniques are used to keep signals in the antenna main beam. In a simple tracking system, the AOA estimate of the signal is somewhere around a beamwidth. This is too rough for a tracking system to operate as a tracker.

Three common techniques are conical scan, sequential lobing and monopulse tracking. Monopulse tracking is the main technique used in this work and is discussed in Chapter V to implement a tracking system using DBF. Thus, the first two techniques are only discussed briefly.

1. Conical Scan

Conical scan, also known as con-scan, uses a single time-shared beam as a tracker. The scan structure of conical scan tracker is shown in Figure 15. The squint angle θ_q is defined as the difference angle between the rotation axis and the beam axis. The target axis points toward the signal source. The antenna beam traces a cone pattern around its rotation axis.

The amplitude of the signals from the emitter is modulated at a frequency equal to the beam rotation frequency. If the target axis and the rotation axis are aligned, there is a constant amplitude return. If the target is away from the rotation axis, the amplitude of the modulation depends on the angular distance between the rotation axis and the target axis [4].

A tracking system can be implemented by continuously adjusting the rotation axis to position to the target axis.

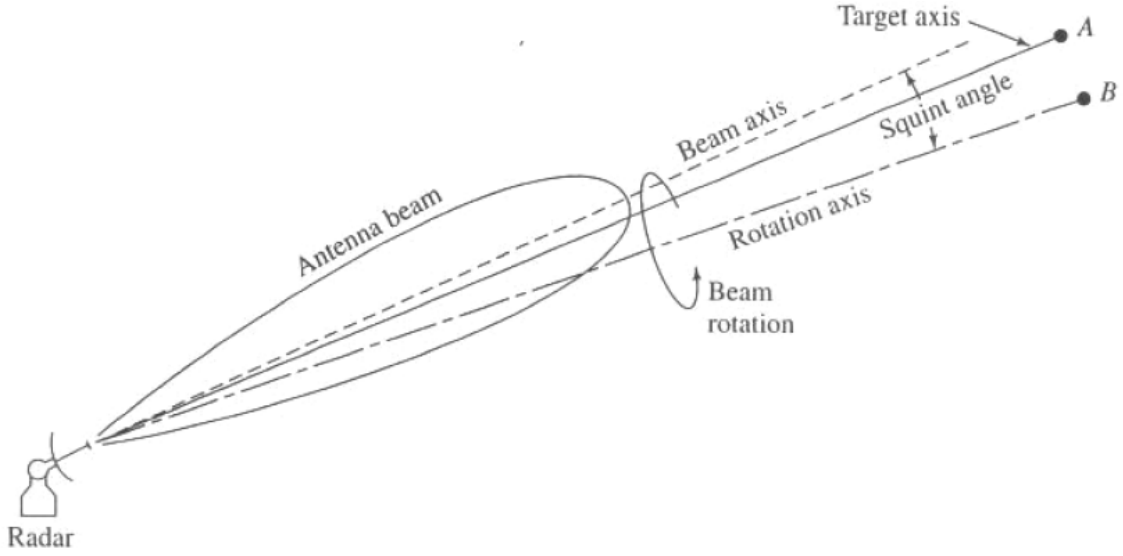

Figure 15. Scan structure of conical scan (from [4]).

2. Sequential Lobing

Sequential lobing, as depicted in Figure 16, uses a single beam that is rapidly switched between positions 1 and 2. Two beams are squinted with angles $\pm\theta_q$ compared to the boresight angle θ_0. The boresight angle is defined as the crossover of the two beams. The amplitudes of the received signals are A and B for beam positions 1 and 2, respectively. It determines the sources' deviation angle from the boresight. After obtaining the arrival angle θ_T, the antenna repositions the boresight to the θ_T direction. The tracking process is accomplished by continuously comparing the amplitude and adjusting the boresight direction to the source direction [4]. The switched time interval causes the received signals from the source to fluctuate due to propagation variations and results in degradation of the accuracy of the measurement.

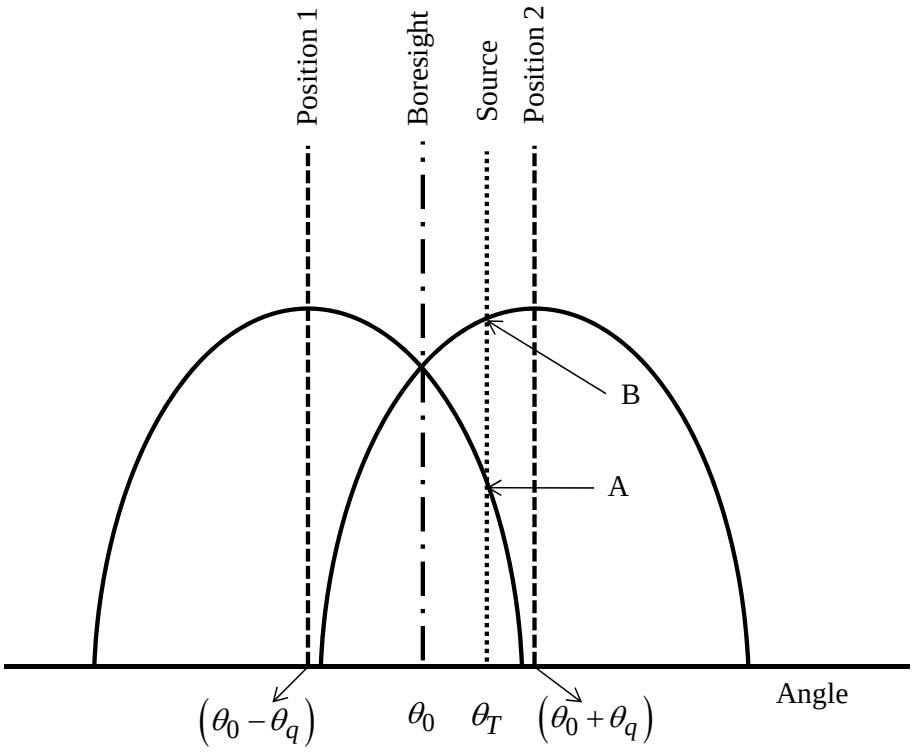

Figure 16. Sequential lobing in rectangular representation (after [4]).

3. Monopulse Tracking

The first two methods require the processing of multiple measurements over a finite observation time. Fluctuations in the signal over the observation time cause measurement errors. Instead of switching beams to different angles like sequential lobing or using one single time-shared beam to do conical scan, monopulse (simultaneous lobing) tracking uses two or more simultaneous beams to conduct comparisons. It derives the angular location of a target with a single observation. Hence, there is no time interval problem in monopulse tracking. The accuracy of monopulse is higher than other tracking systems because the sampled signals do not change with time. There are no amplitude fluctuation problems in monopulse [4].

There are two types of monopulse. One is amplitude comparison monopulse and the other is phase comparison monpulse. Amplitude comparison monopulse is the most common, so the term monopulse generally refers to amplitude comparison monopulse.

a. Amplitude Comparison Monopulse

Two beams are overlapped and their main beams are pointed at small positive and negative angles $\pm\theta_q$ which are defined as squint angles or offset angles. The antenna radiation patterns of the two squinted beams are shown in Figure 17. One way to implement two squinted beams in arrays is to use two beamforming networks.

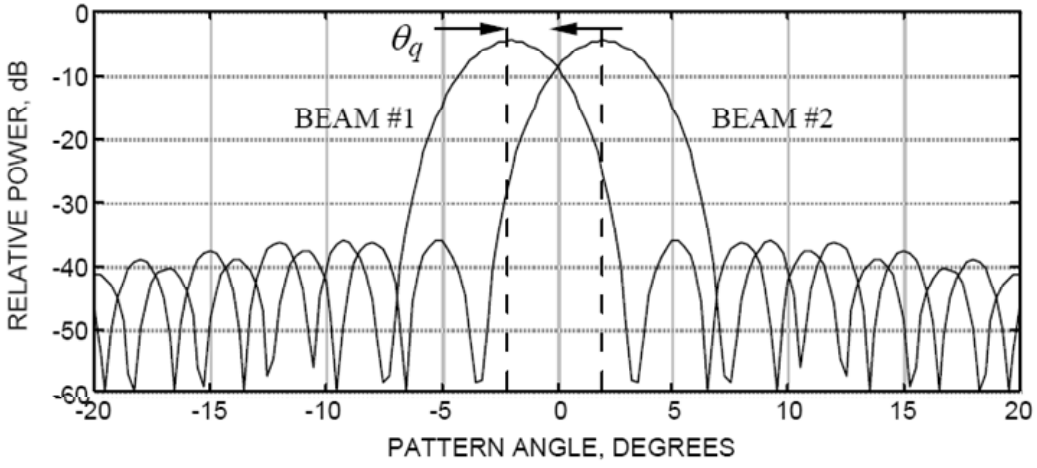

Figure 17. Antenna radiation patterns of two squinted beams (from [19]).

The sum and difference of the two squinted beams are displayed in Figure 18. Both the sum and the difference patterns are used for reception but only the sum pattern is used for transmission. Each channel requires a separate receiver [19].

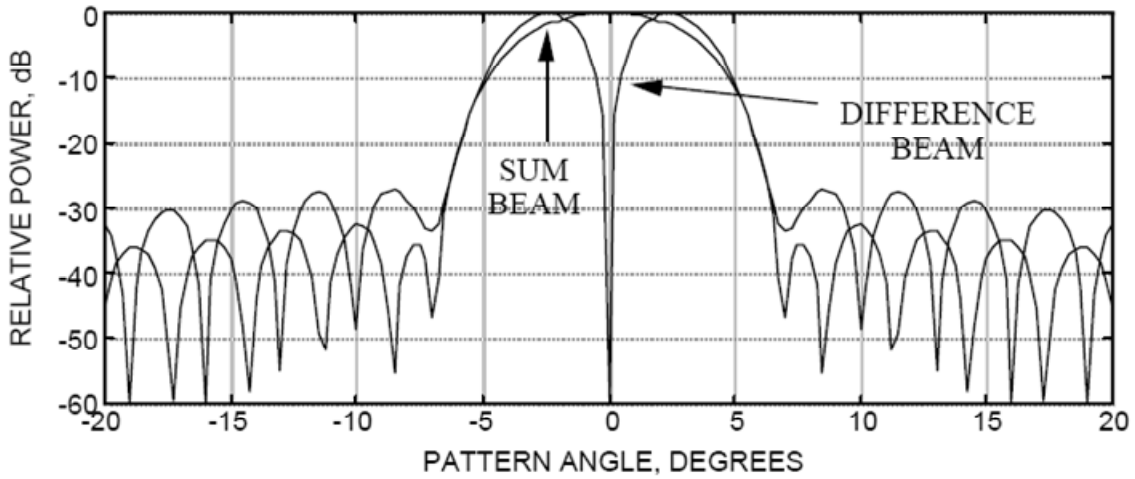

Figure 18. Sum and difference patterns of two squinted beams (from [19]).

The objective of monopulse tracking is to position the null of the difference pattern in the direction of the source. The difference pattern provides the magnitude of the angle error. The direction ($\pm$ sign) of the angle error comes from the phase comparison of the sum pattern with the difference pattern. From [19], the difference-to-sum voltage ratio is used to generate the angle error and is represented as

$$\frac{\Delta}{\Sigma} = \frac{\text{difference voltage}}{\text{sum voltage}}. \tag{27}$$

The plot of Δ / Σ in the vicinity of the null is shown in Figure 19. In the linear region, the ratio can be simplified to

$$\frac{\Delta}{\Sigma} \approx K\theta \tag{28}$$

where θ is the angle error (how far the source is off boresight) and K is the monopulse slope constant. If the squint angle is increased, the monopulse slope constant, K, increases and the angle measurement is more accurate. However, increasing the squint

angle also decreases the gain on axis of the sum pattern. From [4], there is an optimum two-way tracking squint angle derived as $\theta_q = 0.31\theta_B$ where θ_B is the HPBW of the squinted beams.

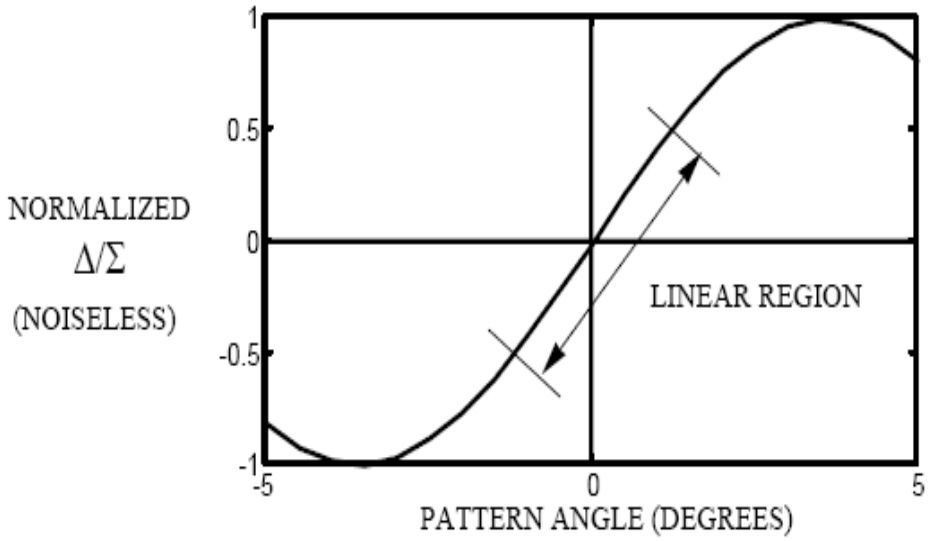

Figure 19. Plot of Δ/Σ where scan angle is at boresight (from [19]).

b. Phase Comparison Monopulse

Phase comparison monopulse is similar to amplitude comparison monopulse, but the two antenna beams point in the same direction rather than being squinted at an angle. In this case, the amplitude of the received signals is the same, but the phase is different. The phase difference ($\Delta\phi$) of the signals from the source is estimated as

$$\Delta\phi = 2\pi \frac{d}{\lambda} \sin\theta \tag{29}$$

where d is the spacing between the two antennas and θ is the signal direction compared to the normal direction of the baseline.

By measuring the phase difference of the received signals, the angle to the signal can be derived. A phase comparison monopulse tracker is also known as an interferometer [4].

C. ANGULAR ACCURACY AND LIMITATIONS

In this section, discussion focuses on angular accuracy. There are factors that limit angular accuracy, such as receiver noise, antenna errors and multipath. They are discussed briefly in this section.

1. Theoretical Angular Accuracy

Following the approach in [4], the theoretical antenna root mean square (RMS) error in angle measurement can be approximated as

$$\delta\theta = \frac{1}{\gamma\left(2E / N_0\right)^{1/2}} = \frac{1}{\gamma\left(S / N\right)^{1/2}} \tag{30}$$

where E is the received signal energy, N_0 is the noise power per unit bandwidth, γ is the effective aperture width and S / N is the SNR. For an array, γ is defined as

$$\gamma^2 = \frac{\sum_{n=1}^{N} \left(2\pi d_n / \lambda\right)^2 \left|A_n\right|^2}{\sum_{n=1}^{N} \left|A_n\right|^2} \tag{31}$$

where N is the number of array elements, d_n is the distance of element n from the center of the array, λ is the wavelength and A_n is the amplitude illumination, which is further discussed in Chapter V. The theoretical angle error with a uniform amplitude illumination $\left(A_n = 1, n = 1, ..., N\right)$ is

$$\delta\theta = \frac{\sqrt{3}\lambda}{\pi D\left(2E / N_0\right)^{1/2}} = \frac{0.628\theta_B}{\left(SNR\right)^{1/2}} \tag{32}$$

where θ_B is the HPBW and is approximately $0.88\lambda / D$. D is the total length of the array $\left(D \approx \left(N - 1\right)d\right)$.

2. Receiver Noise

Noise at the receiver will affect the angular accuracy of a tracking system. As seen in Equation (32), high angular accuracy can be achieved by using a narrow HPBW

and high SNR [4, 20]. In the case of monopulse, the noise fills the difference beam notch and prevents accurate measurement of angle, as shown in Figure 20. Receiver noise becomes a major factor for angular accuracy when the received signal is very small. The RMS error in angle measurement due to receiver noise in terms of the monopulse slope constant, K is given as

$$\delta\theta = \frac{0.868}{K\sqrt{SNR}}. \tag{33}$$

This relationship is based on results that are derived in Chapter V.

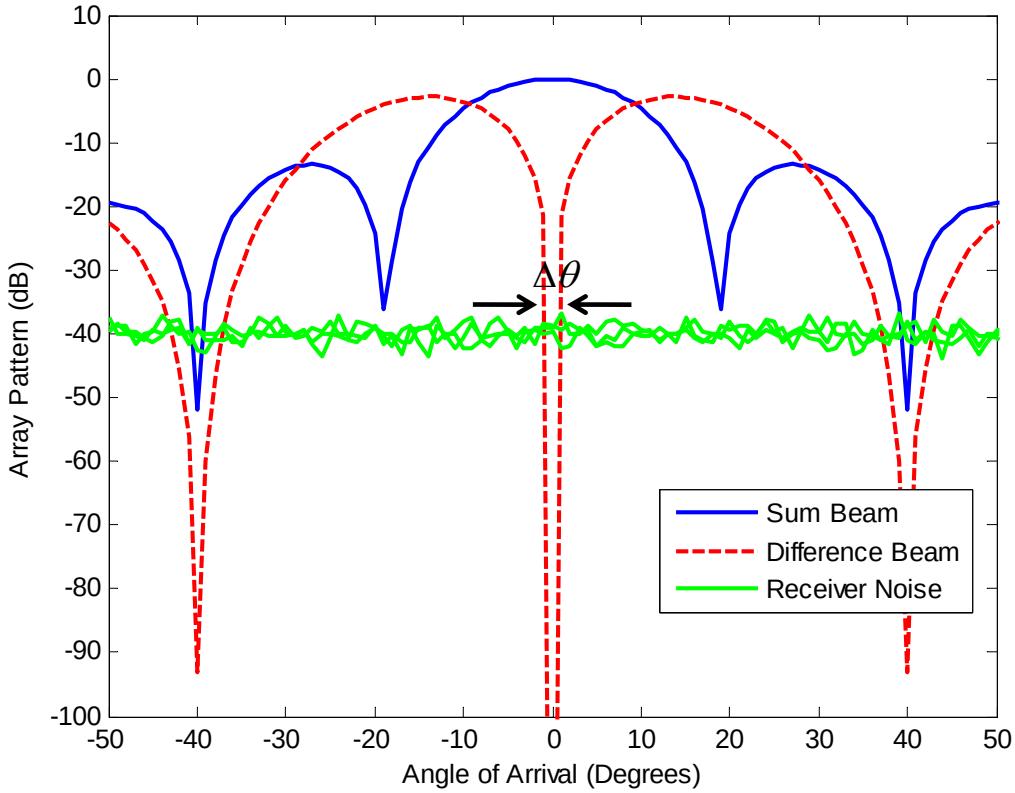

Figure 20. Monopulse tracking with receiver noise contribution (after [8]).

3. Antenna Errors

The theoretical antenna radiation pattern is often different from the actual radiation pattern, especially at wide angles. There are two main factors that cause

aperture illumination errors, one is systematic and the other is random. Systematic errors consist of mutual coupling and discrete quantization from the digital phase shifter. Random errors may come from fabrication precision, distortion of the antenna surface or phase variation caused by temperature [4].

In the system considered in this thesis, antenna errors cause null shifting and null filling and are independent of the signal. The patterns in Figure 21 show the effect of random amplitude errors. Simulated random amplitude errors (0.95 < amplitude errors < 1.05) are multiplied at each antenna element and the resulting difference beam deviated slightly from the original one [19].

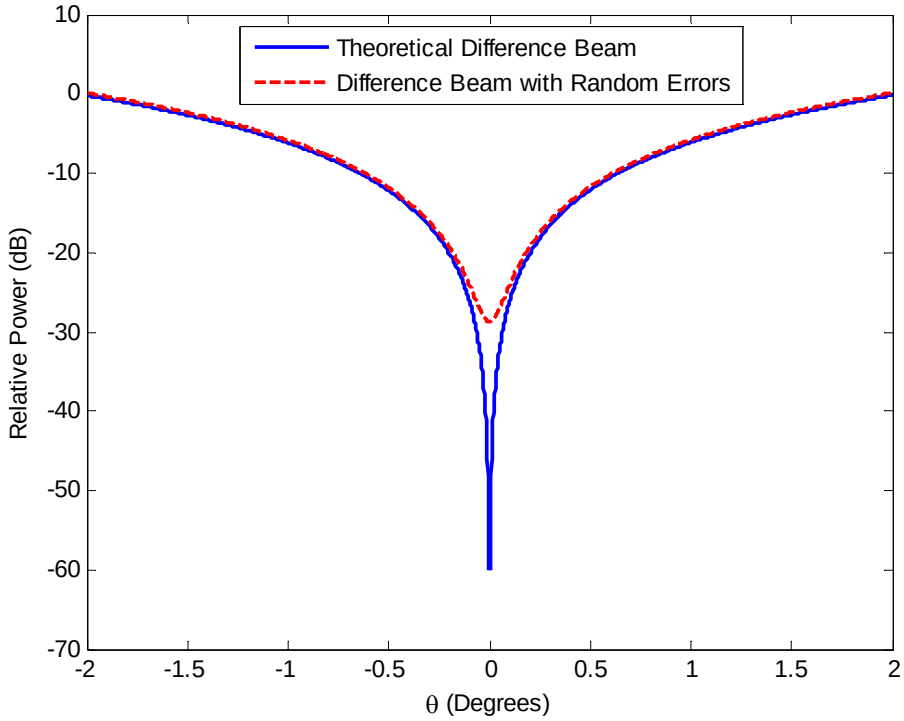

Figure 21. Difference beam with antenna errors contribution.

In Figure 22, two slope constants are displayed, one with no error and the other with random errors. The slope constant with random errors causes a reduction in angle accuracy. This is due to antenna hardware errors rather than amplitude errors. As

explained in Chapter V, the digital beamforming process weighs all channels equally. Therefore, amplitude errors do not affect beam pointing.

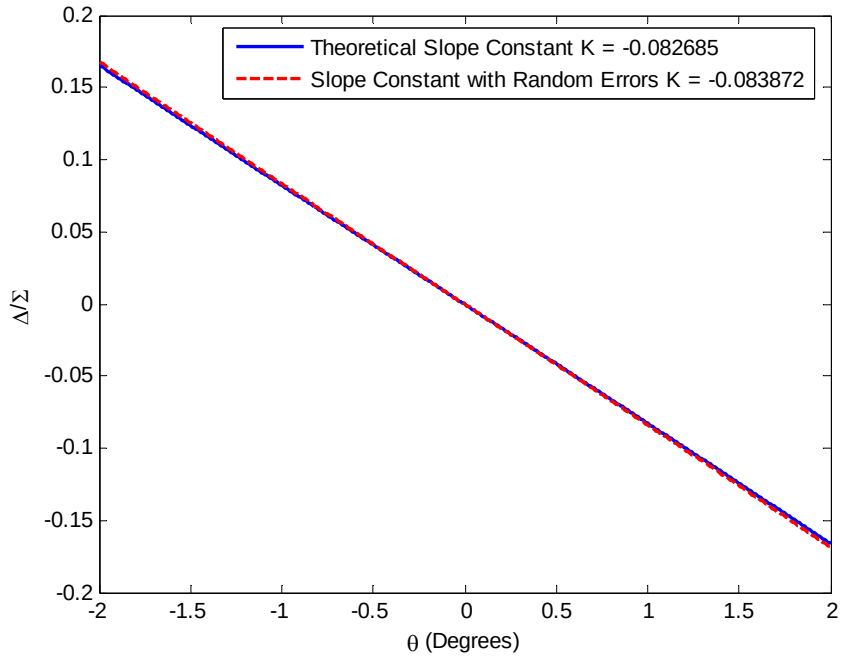

Figure 22. Slope constants variation with antenna errors contribution.

4. Multipath

Except for LOS wave propagation, there are potentially multiple propagation paths between the transmitter and receiver. Multipath is a major factor causing the degradation of angle accuracy, especially near the surface of the earth. Emitted signals reflect from the ground causing a mirror image which confuses the tracker [21]. The multipath between the transmitter and receiver is shown in Figure 23.

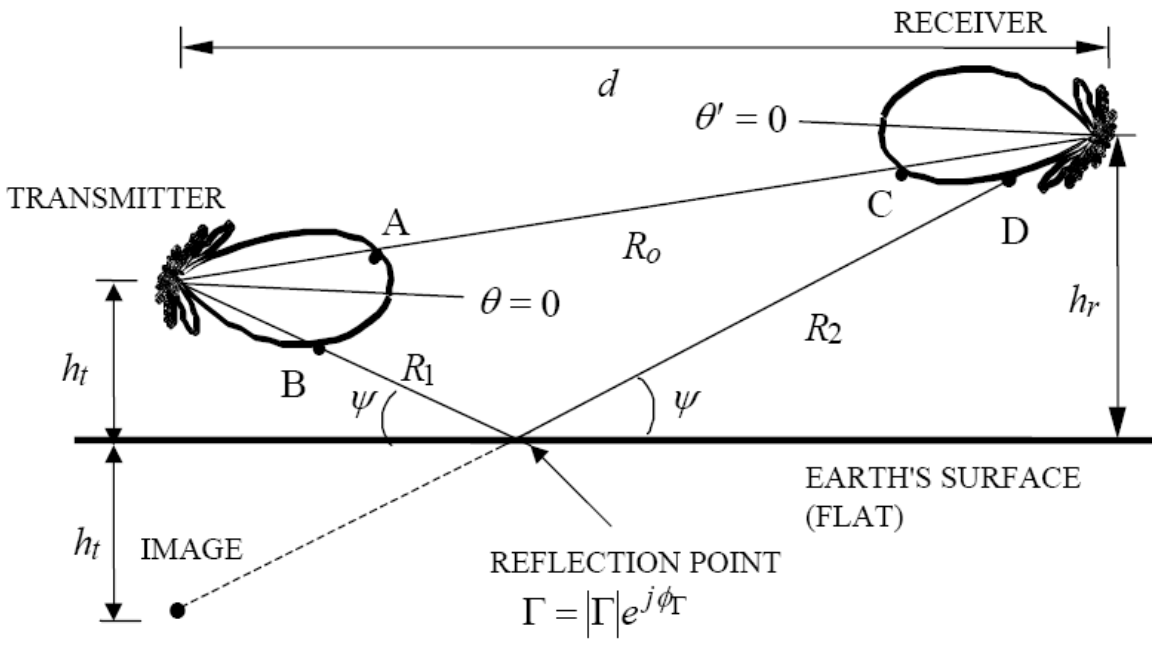

Figure 23. Multipath between transmitter and receiver (from [22]).

From [22], the path difference when $h_t, h_r << d$ is given by

$$\Delta R = \left(R_1 + R_2\right) - R_0 = \sqrt{d^2 + \left(h_t + h_r\right)^2} - \sqrt{d^2 + \left(h_t - h_r\right)^2} \approx \frac{2h_t h_r}{d} \tag{34}$$

where $\left(R_1 + R_2\right)$ is the reflection path and R_0 is the direct path. The path gain factor (PGF) is defined as

$$\left|F\right| = \left|1 + \Gamma e^{-jk\Delta R}\right| = \left|1 + \Gamma e^{-jk2h_t h_r / d}\right| = 2\left|\sin\left(kh_t h_r / d\right)\right| \tag{35}$$

where $\Gamma = -1$ is the reflection coefficient of the surface. The received power, which is proportional to the square of the PGF, is given as

$$P_r \propto \left|F\right|^2 = 4\sin^2\left(\frac{kh_t h_r}{d}\right) \approx 4\left(\frac{kh_t h_r}{d}\right)^2. \tag{36}$$

In Equation (36), the small angle approximation is assumed. As the altitudes of the transmitter and receiver decrease, the received signals $\left(P_r\right)$ are weaker, resulting in larger tracking errors [22]. In Chapter V, the hardware testing of a monopulse tracker is implemented in an anechoic chamber to reduce multipath effects. In the system

developed in this thesis, only tracking in azimuth is of interest. Multipath is primarily of concern in elevation tracking. However, ground bounce may cause fading of the signal and possible loss of track, in which case, the processor must re-acquire the signal.

THIS PAGE INTENTIONALLY LEFT BLANK

IV. DESIGN AND BENCHTOP HARDWARE TESTING OF A SINGLE-CHANNEL RSNS DF ARRAY

There are three objectives in this chapter. The first objective is to design and implement a DF hardware platform using a single-channel virtual RSNS. The second objective is to demonstrate the operation of the RSNS module using a benchtop test setup. The received phase difference from the simulated signal source is converted to the AOA and compared to the AOA based on the actual phase difference from the network analyzer. The LabView software design and development is also described in this chapter.

A. SINGLE-CHANNEL RSNS DESIGN

The RSNS algorithm was implemented in LabView and encapsulated as a visual interface (VI) function called out by the DF main program. At the beginning of the RSNS design, the channel number and moduli were selected based on system requirements.

In this application, a single-channel RSNS was designed. It had two antenna elements ($N = 2$). Two relatively prime numbers, 5 and 9, were chosen as the moduli ($m_1 = 5, m_2 = 9$). From Equation (20), the dynamic range ($\hat{M}$) was obtained as 36. The number of folds for each moduli was calculated by using Equation (21). The result was 1.8 folds and 1 fold for moduli 5 and 9, respectively. The testing platform was operated at a frequency of 2.4 GHz ($\lambda = 0.125$ m). From Equation (22), the antenna virtual element baseline distances for the two channels were computed as $d_1 = 0.1125$ m and $d_2 = 0.0625$ m. These are virtual channels in the sense that they do not require physical elements spaced at d_1 and d_2. Any physical spacing can be used as long as the amplitude folding waveform has only one fold $(d < \lambda)$. For the array, the selected physical spacing was $d = 0.0625$ m. With regard to re-mapping the FOV for acquisition,

the required FOV was from -90° to $+90^{\circ}$. Therefore, by Equation (23), the scaling factor was $\zeta = 1$. The thresholds were calculated from Equation (25) and are shown in Table 2.

Table 2. Threshold values $V_{j,m}$ for $\hat{M} = 36$ (after [10]).

m \ j	1	2	3	4	5	6	7	8	9
5	-0.9511	-0.5878	0	0.5878	0.9511				
9	-0.9848	-0.8660	-0.6428	-0.3420	0	0.3420	0.6428	0.8660	0.9848

The final step was to calculate the phase adjustment for each element to align the center of the dynamic range to the folding waveforms at broadside $\left(\theta = 0^{\circ}\right)$. In accordance with [8] and Equation (26), phase adjustments were calculated. The result for element 1 was $\varsigma_1 = -1.2566$ radians and for element 2 it was $\varsigma_2 = -1.5708$ radians. The normalized folding waveforms with phase adjustments for moduli [5, 9] are shown in Figure 24.

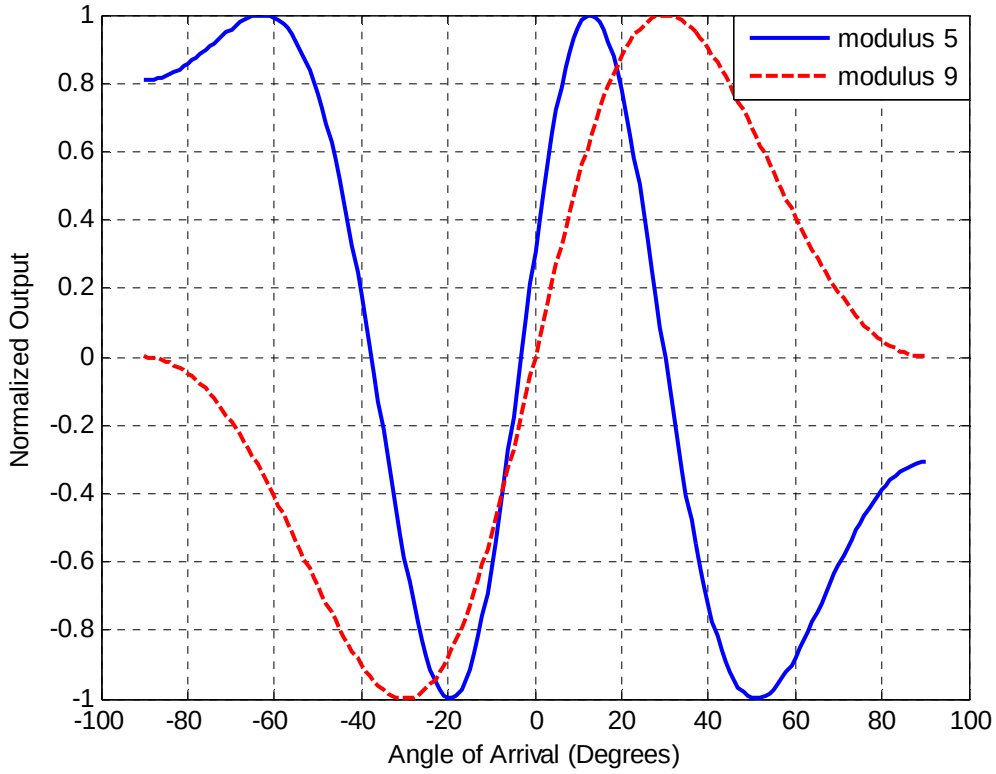

Figure 24. Normalized folding waveforms with phase adjustment of moduli [5, 9].

From [20], the estimated AOA $\left(\theta'_u\right)$ for the u^{th} bin is given as

$$\theta'_u = \sin^{-1}\left(\frac{2u+1}{\hat{M}\zeta} - \frac{1}{\zeta}\right) \tag{37}$$

and the angle resolution $\left(r_u\right)$ for the u^{th} bin is given as

$$r_u = \sin^{-1}\left(\frac{2u-\hat{M}+2}{\hat{M}\zeta}\right) - \sin^{-1}\left(\frac{2u-\hat{M}}{\hat{M}\zeta}\right). \tag{38}$$

The ideal transfer function of the actual AOA versus estimated AOA is displayed in Figure 25. Examining the transfer function reveals that there were 36 stairs due to the dynamic range. The transfer function shows no ambiguities in the FOV.

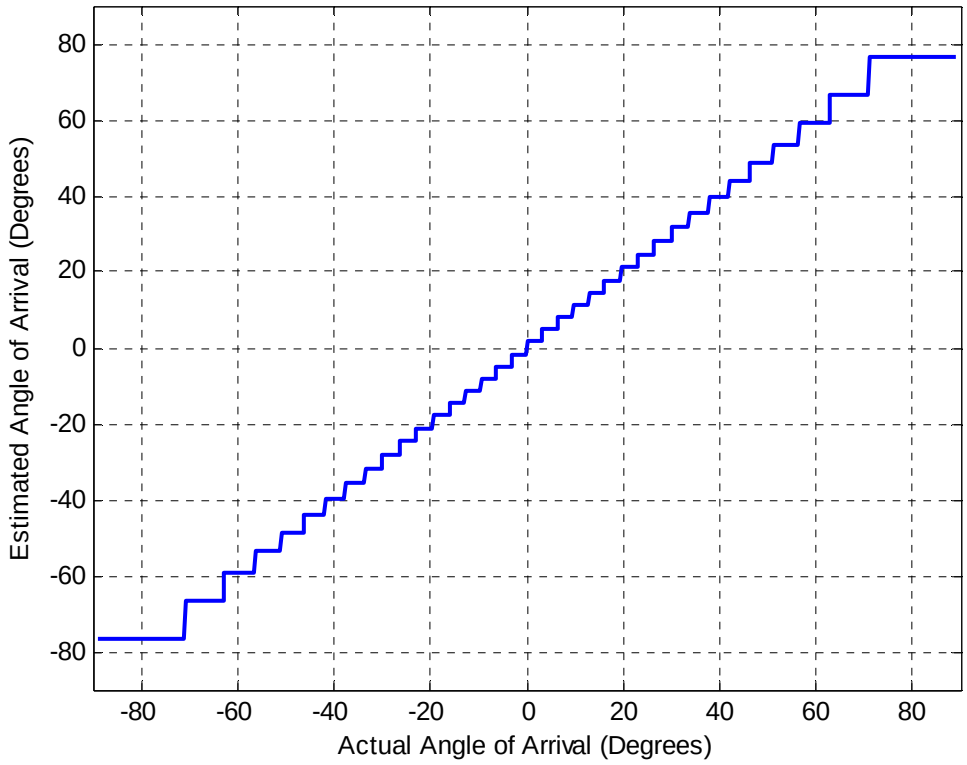

Figure 25. Transfer function for moduli [5, 9] (after [13]).

The error in estimated AOA versus actual AOA is displayed in Figure 26. The minimum angle resolution was 3.1847° at the broadside, and the maximum angle resolution was 19.1881° at two ends of the FOV $\left(\pm 90^{\circ}\right)$.

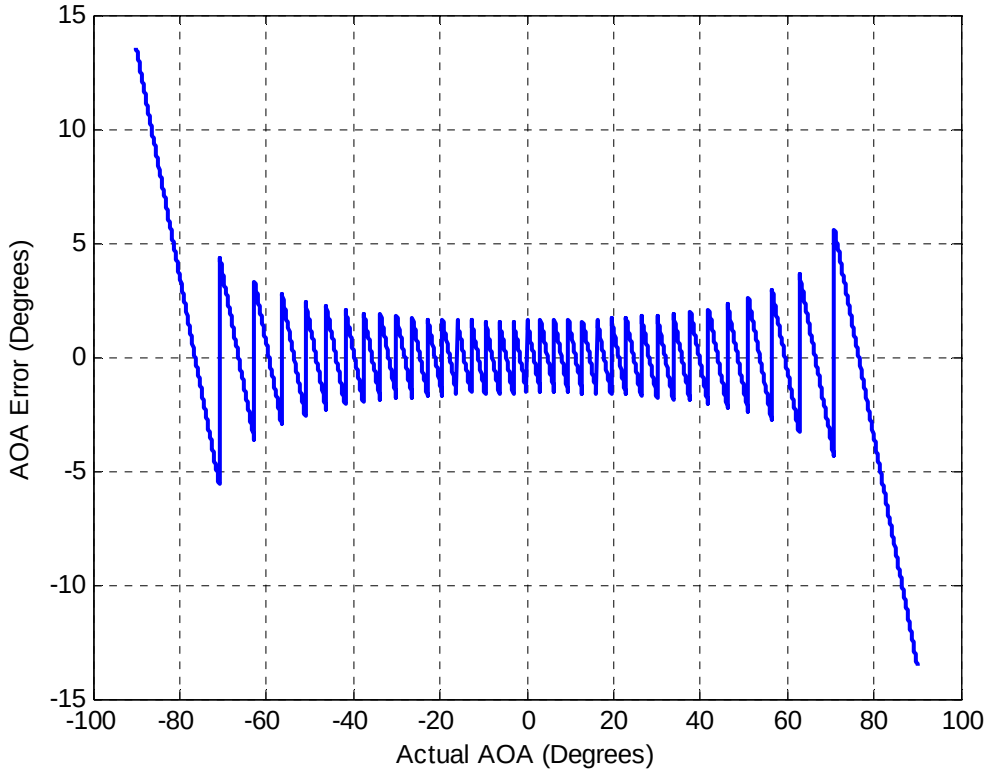

Figure 26. AOA error for moduli [5, 9] (after [23]).

B. BENCHTOP HARDWARE SETUP

A benchtop hardware test set was built to test the single-channel virtual RSNS concept [10]. The test platform used a signal generator to simulate a signal source that was received at the outputs of the antennas. The system block diagram, including hardware and software blocks, is shown in Figure 27. The generated signal out of the vector network analyzer (VNA) was separated into two paths. The first was connected to another power splitter and served as the LO input to the two demodulator boards. The second path was connected to a power splitter and served as the RF input to the two demodulator boards. One sub-division was the reference path (master) with no phase change inserted, and the other was a phase-shifted path (slave) with a phase change inserted. The demodulator board within the master path was designated TST1 and in the slave path was called TST2. The received signals through each of the paths were

demodulated and output I/Q values were passed to the digitizer, PXI-5112. The digitized signals were then passed to the computer, PXIe-1062Q, and accessed by the RSNS module, which was developed in LabView, to calculate the AOA [10].

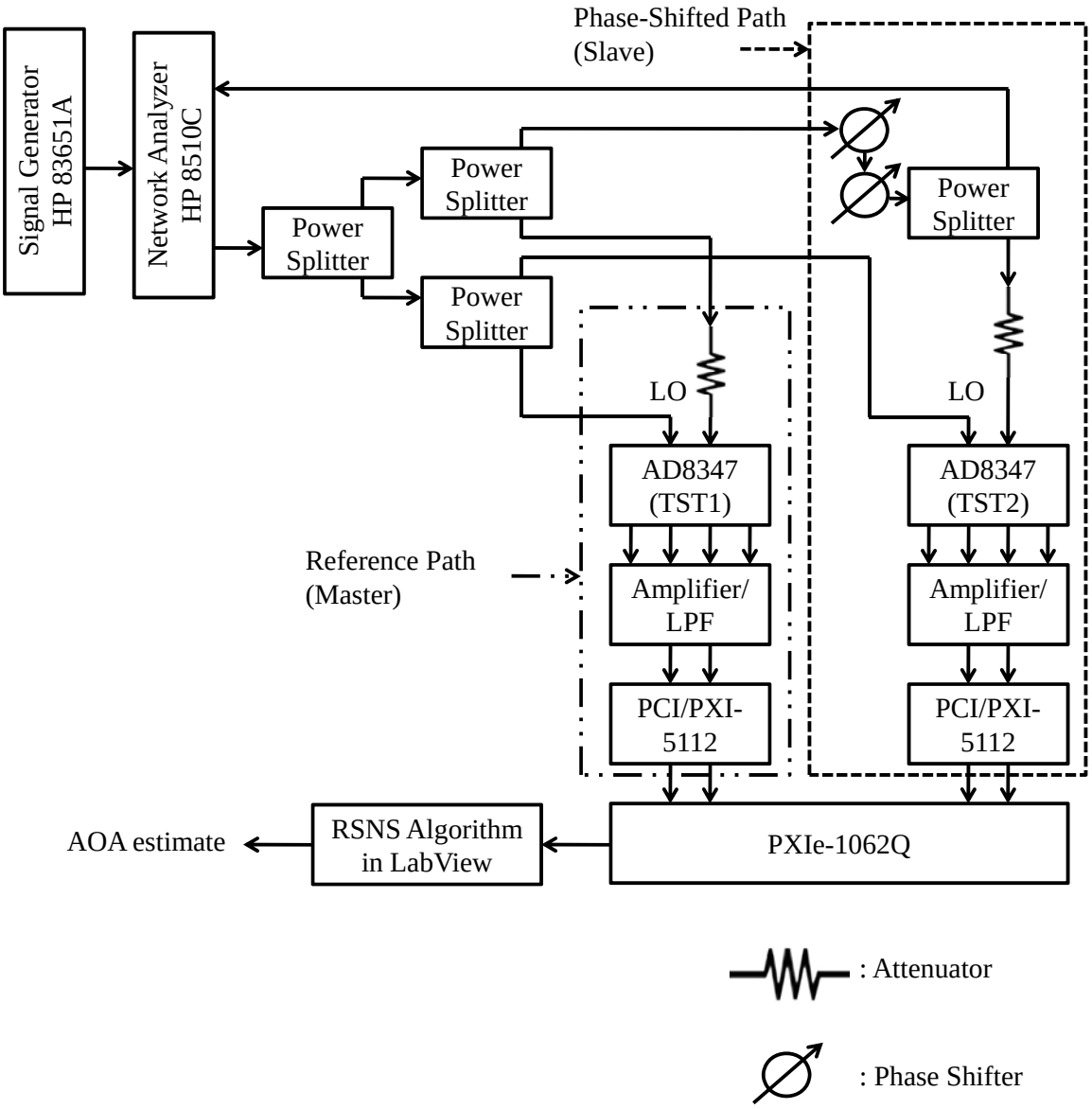

Figure 27. Block diagram of the DF testing platform (after 10).

The main purpose of this measurement was to validate the DF system software and evaluate the performance of the single-channel RSNS. To simply the system, the phase difference coming from the signal source was simulated by changing the phase

shifters in the test platform. The signal source was operated at 2.4 GHz, and a total of 360° phase change was provided by two mechanical phase shifters. Each of them had a 180° range with 30 turns (one turn equals to approximately 6°).

The signal generator was part of the VNA, HP8510C. The phase difference was not only measured by the DF system but also measured by the VNA, so the exact phase was known to within about 1°. The two acquired values were compared and the details were presented in Section E of Chapter IV. To make the phase measurement accurate, the signal paths were required to be equal, aside from the mechanical phase shift.

A photograph of the testing platform is shown in Figure 28. The test set components and their specifications are listed in Table 3.

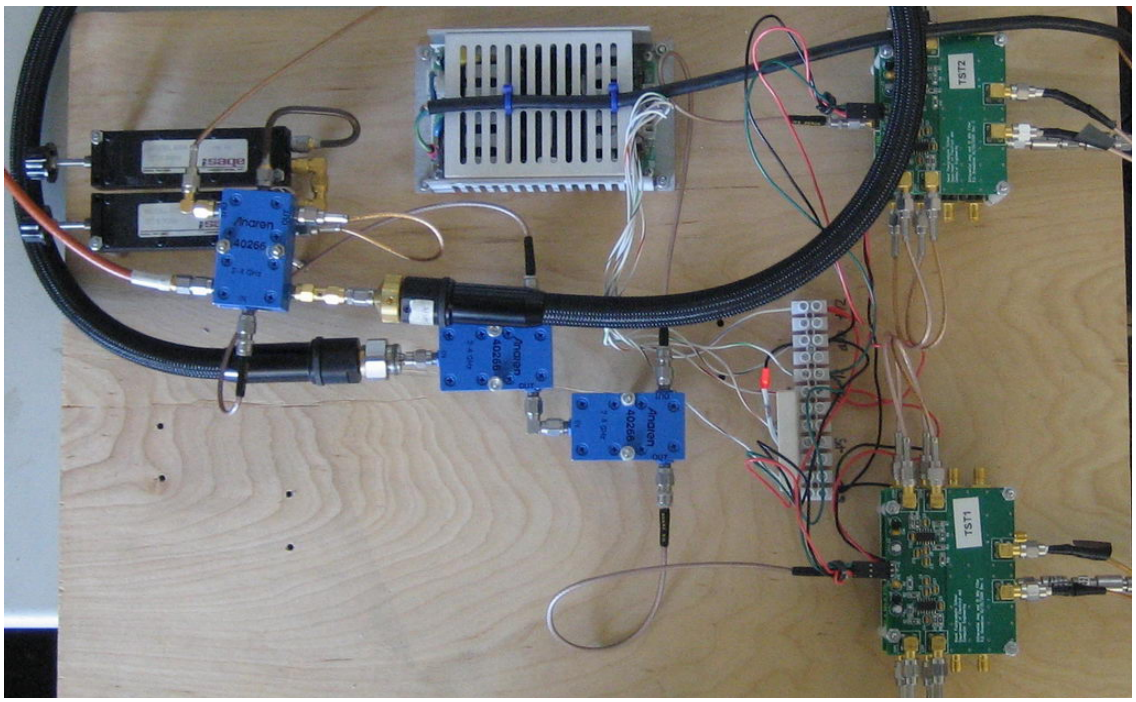

Figure 28. Photograph of a single-channel RSNS DF benchtop test system.

Table 3. Hardware equipment list (after [10]).

Component Name	Quantity	Specification
Signal Generator	1	Model: HP 83651A Series Synthesized Sweeper Frequency Range: 45 MHz to 50 GHz
S-Parameter	1	Model: HP 8517A S-Parameter Test Set Frequency Range: 45 MHz to 50 GHz
Network Analysizer	1	Model: HP 8510C Network Analyzer
Power Splitter	4	Model: Anaren 40266 Frequency Range: 2 to 4 GHz Maximum Insertion Loss: 0.3 dB Maximum VSWR: 1.3 SWR
Phase Shifter	2	Sage Laboratories Inc. DC-8 GHz
DC Power Supply	1	Condor GL50A 50 Watt CH1 5.05 VDC 4 A, CH2 12 VDC 2.5 A, and CH3 12 VDC 0.2 A
Cable	19	Pasternek Cable RG-306
Variable Attenuator	1	Telonic Altair Attenuation Model 8140S
Direct Conversion Quadrature Demodulator [TST1, TST2]	2	Model: AD8347 (Analog Devices) LO/RF Frequency Range: 800 MHz to 2.7 GHz LO Input Level: -10 dBm to 0 dBm and -8 dBm (recommended) RFIP: 10 dBm (Max) Power Supplies: 2.7 to 5.5 V
Amplifier	2	Differential Amplifier with LPF bandpass 3 dB of 10 MHz and Voltage gain of 10
Processor	1	Model: PXIe-1062Q (NI) Slots: 8 PXI Express Chassis for PXI and PXI Express Modules
Digitizer [DAQ 2, DAQ 3]	2	Model: PCI/PXI-5112 (NI) Resolution: 8 bits Sample Rate: 100 MS/s (Max) Bandwidth (-3 dB) : 100 MHz (Max)

Before starting measurement, there was another issue taken into consideration. Two of the demodulator boards, TST1 and TST2, had to be calibrated to remove DC offsets. The calibration process is explained in Section C.

C. CALIBRATION

Two of the demodulator boards, TST1 and TST2, used in the testing platform, had DC offsets that had to be determined and deducted from test measurements before applying the RSNS algorithm. This process made the phase measurement more accurate. The calibration method was to measure the I and Q values through the whole 360° and calculate the mean I and Q values, which corresponded to the I/Q circle center coordinates. The calibration process was to re-map the I and Q values so that they were centered at zero [10].

The program used to calibrate was developed in [10] and implemented in LabView. Some of the functions were revised. The new LabView front panel is shown in Figure 29. A default file-save-name and paths are located in the upper-left corner of the front panel. The graph in the upper-right of the panel is used to display the I/Q input signals from the testing platform. The lower-left graph displays the uncalibrated DC offsets and the lower-right graph displays the calibrated DC offsets. The measured I and Q DC offset values appear at the bottom of the panel.

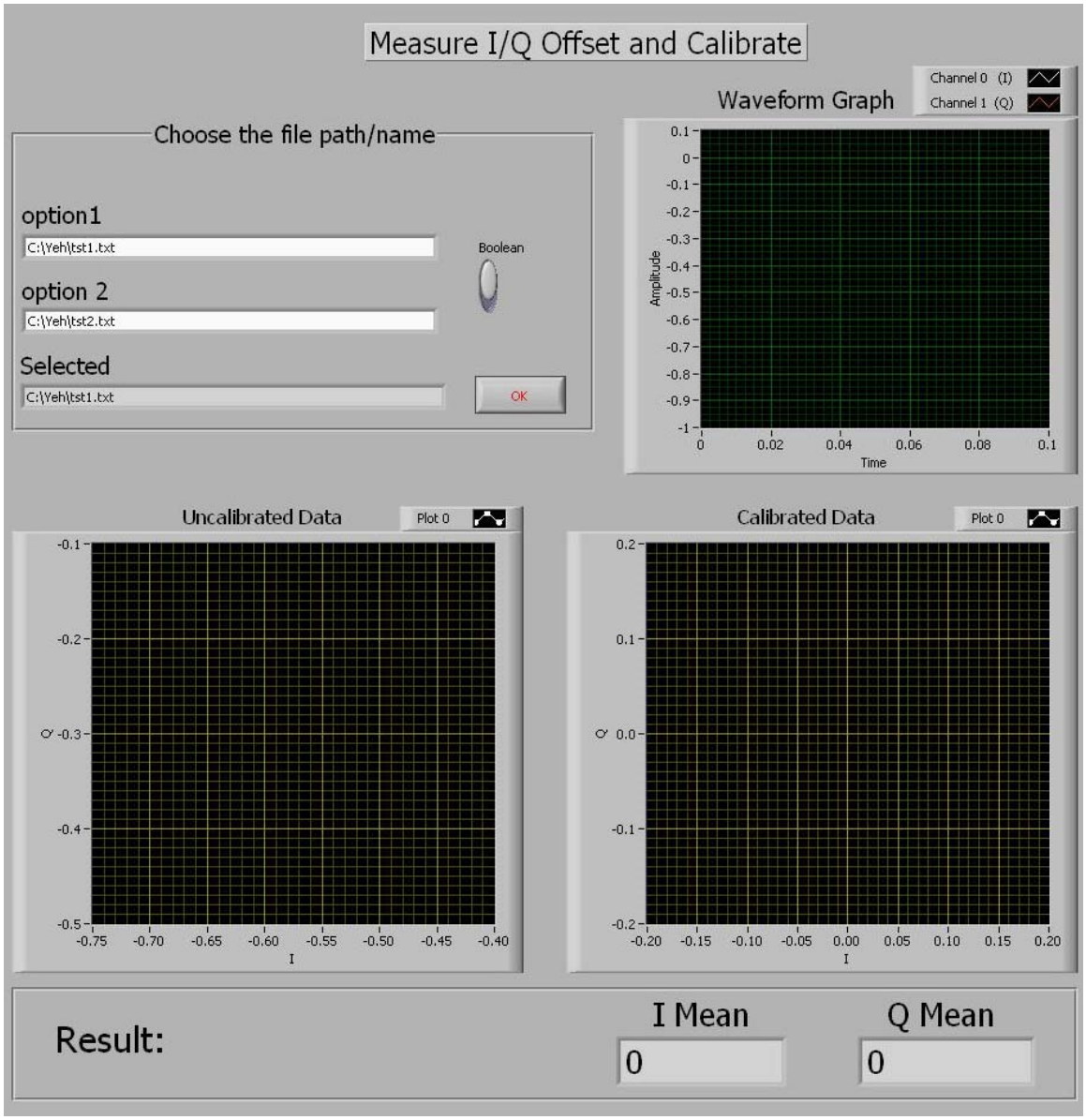

Figure 29. Front panel of calibration (after [10]).

There are two parts in this calibration program. The first part of this program is shown in Figure 30. A rate of 10,000 samples per second is selected. Every 10,000 points are summed and used to compute the mean values for both I and Q. The initial measured values are saved to the selected file and a prompt window pops up waiting for the user to change the mechanical phase shifter. In this test, the phases are changed

approximately every 6° (one turn of the phase shifter). The process must go through all 360° of phase, and the measured values are automatically appended to the file.

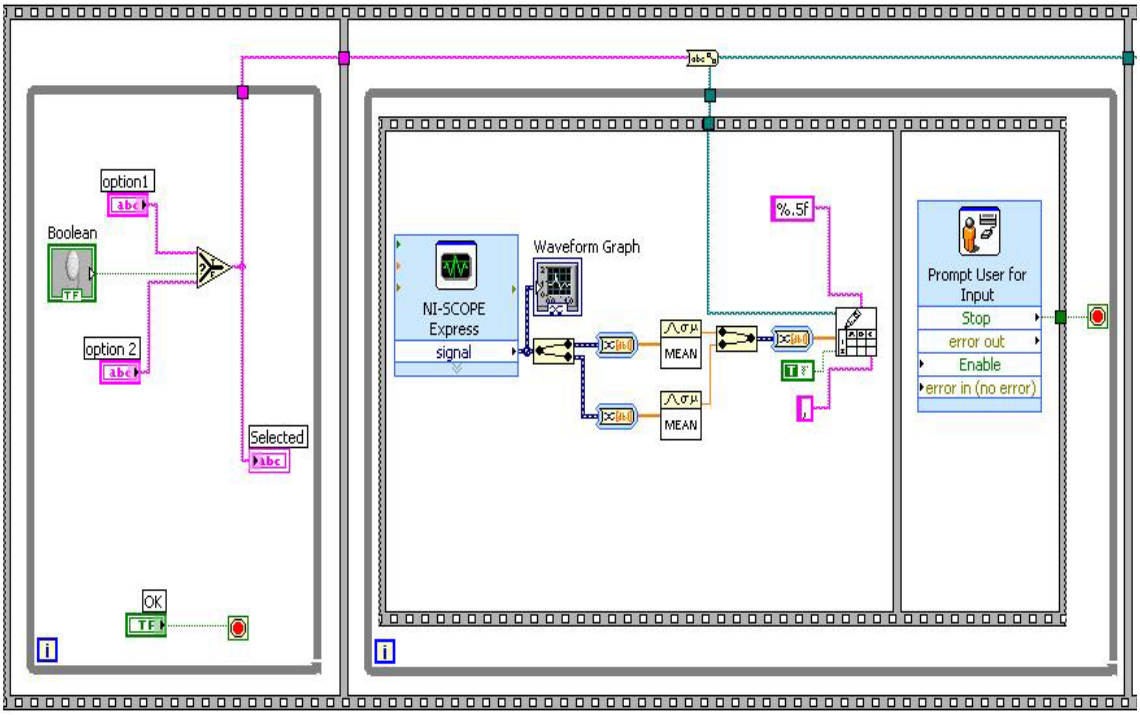

Figure 30. DC values collection in LabView (after [10]).

The second part of this program is to read the saved file in part one and use the raw data to draw the uncalibrated graph, which is not centered at the origin. Another function calculates the mean I and Q values, then subtracts them from the raw data. The subtracted values are used to draw the calibrated graph, which should be centered at the origin. The second part of the calibration program is shown in Figure 31.

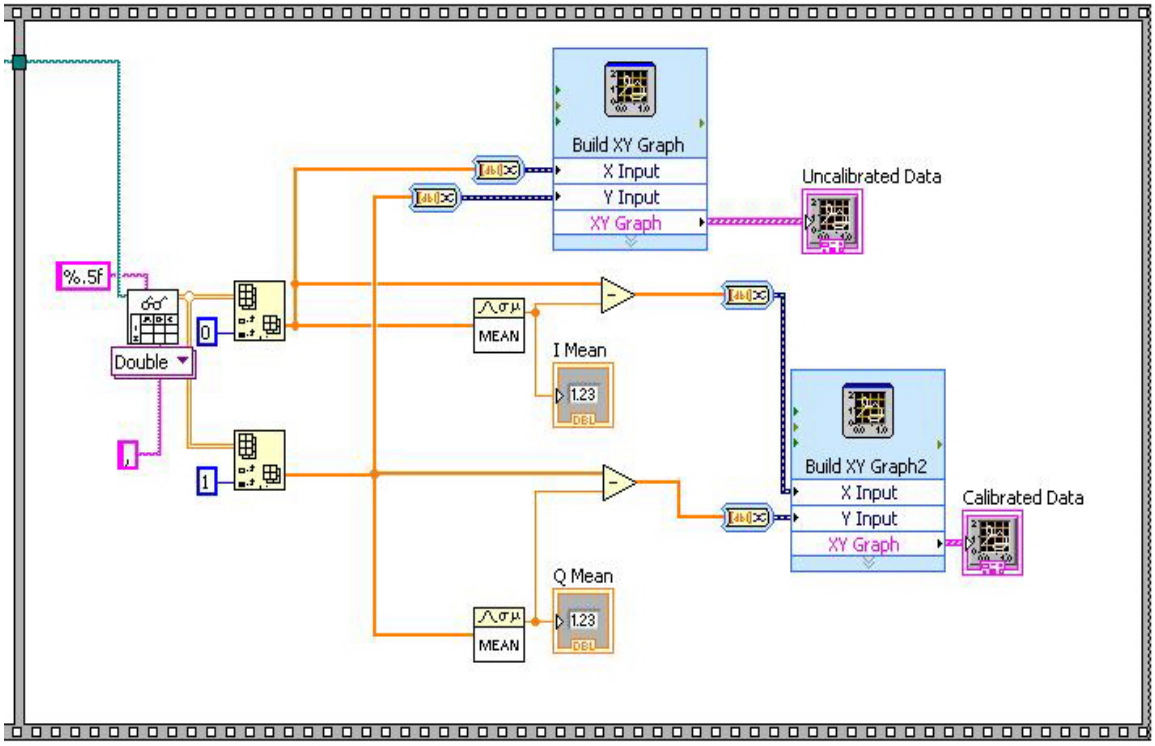

Figure 31. Draw the uncalibrated and calibrated values in LabView (after [10]).

Another issue which affects the accuracy of the measurement is the selection of the proper power level. The power level in each component must be adjusted to avoid over driving or under driving the circuit [10]. Further, the power into the two demodulator boards must be equal, so several attenuators are used to balance the input power levels. Third, most components have a limited or optimum operating power range, and it is necessary to set the power levels to this range. The measured power levels, power supply voltage and attenuator values of the components in the testing platform are listed in Table 4. The minimum, maximum and optimum values are also listed for reference.

Table 4. Power levels in components (after [10]).

	Measured Values	Spec. Min	Spec. Max	Optimum
Network Analyzer	10 dBm	N/A	14 dBm	N/A
LO (TST1)	-8.63 dBm	-10 dBm	0 dBm	-8 dBm
LO (TST2)	-8.70 dBm	-10 dBm	0 dBm	-8 dBm
RFIP (TST1)	-41.57 dBm	N/A	10 dBm	N/A
RFIP (TST2)	-41.61 dBm	N/A	10 dBm	N/A
Attenuator (TST1)	33.5 dB	N/A	N/A	N/A
Attenuator (TST2)	29.5 dB	N/A	N/A	N/A
Power Supplies for TST1 and TST2	5.05 V	2.7 V	5.5 V	N/A

This calibration routine was executed and the results follow. A screen shot of a test is shown in Figure 32. The DC offset for TST1 had a mean value of -0.562005 V in the I channel and a mean value of -0.291017 V in the Q channel. After subtracting the offset values, we see that the calibrated graph shows a circle centered at zero.

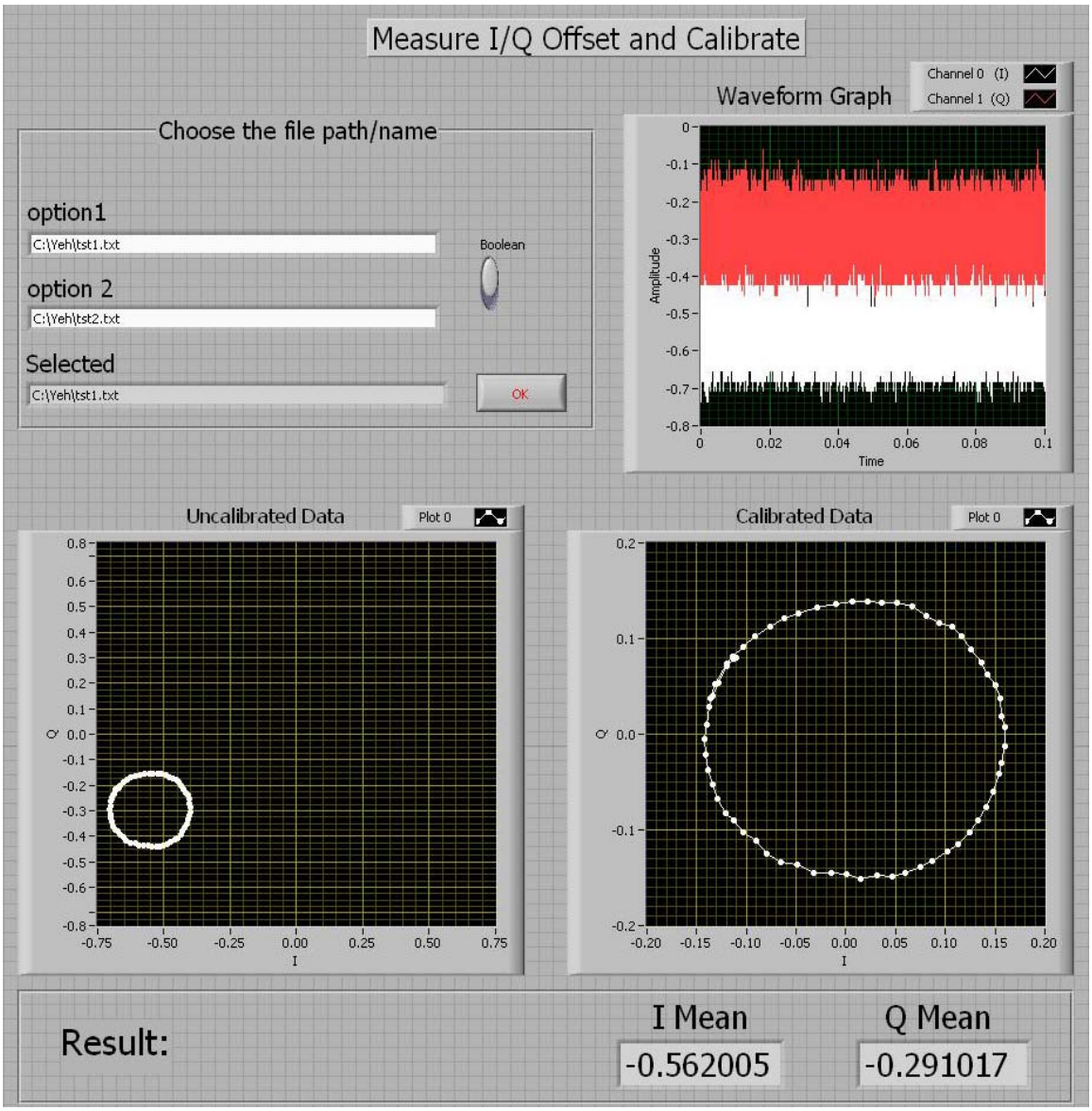

Figure 32. Calibration for TST1 (after [10]).

The DC offset for TST2, which had a mean value -0.540751 V in the I channel and 0.167873 V in the Q channel, is shown in Figure 33. After subtracting the offset values, we see that the calibrated graph shows a circle centered at zero.

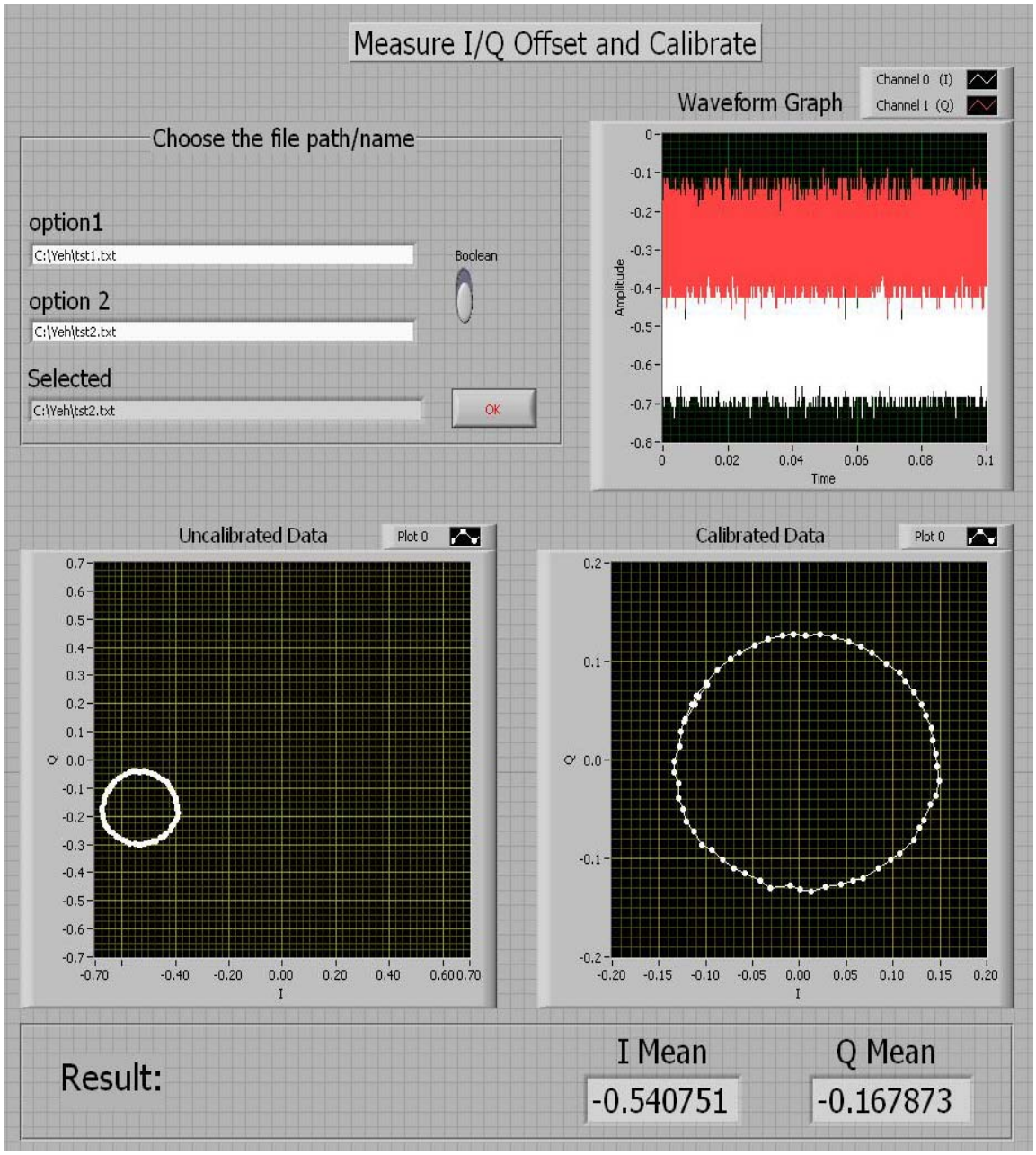

Figure 33. Calibration for TST2 (after [10]).

After implementing the calibration process, we consider that the two demodulator boards are accurate. The next step was to estimate the actual AOA from the signal source as discussed in Section D of Chapter IV.

D. RSNS DF LABVIEW BENCHTOP MEASUREMENT MODULE

LabView is the control and processing software developed by NI. It is a virtual environment for computation as well as control and data logging for physical instruments, such as meters and oscilloscopes. The graphical programming environment provides users the tools to intuitively design test and measurement systems more easily. It is a real time system and is designed to be reliable and much faster than other software system. The programs developed in LabView are easy to revise and modify, so simulations can be used, thus, saving more time than actually assembling and testing a circuit. In this project, LabView Version of 8.5 was used to design and control all modules of the array processor.

After the I and Q signals are sent to the computer, the LabView program assumes control and performs all of the necessary processing. The DF program was originally developed in [10], but some of the functions and layout were revised and modified in this work. Three sections to this program were developed. The first part loads the DC offsets, initiates signal input and configures the system parameters. The second part subtracts DC offsets, calculates the AOA and saves the measured values in various output files. The third part loads the saved files from the second part, draws the simulated AOA versus estimated AOA graph and draws the actual phase difference versus measured phase difference graph. The front panel of the DF module is shown in Figure 34.

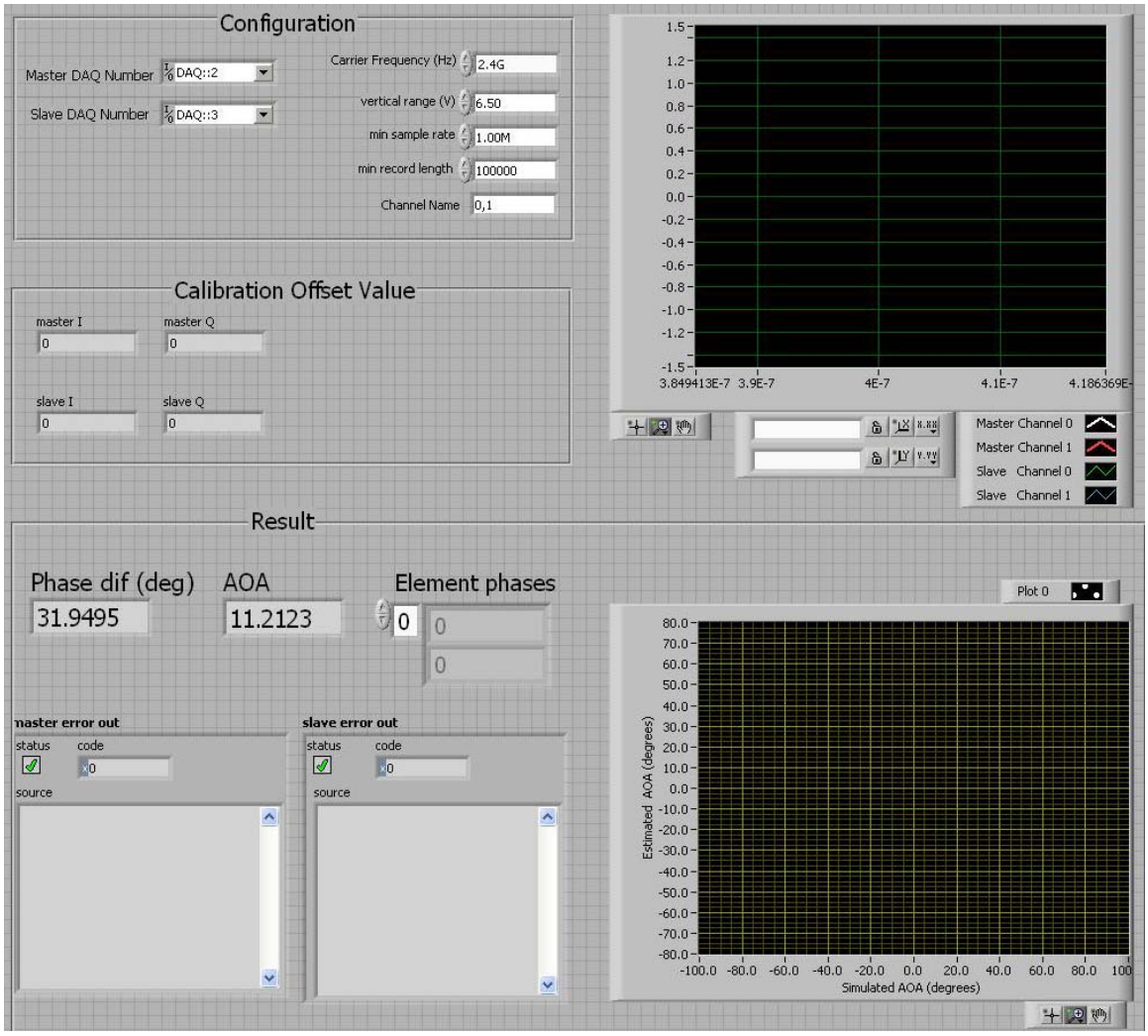

Figure 34. Front panel of the benchtop DF test software (after [10]).

In Figure 35, the first portion of the VI block diagram used for the DF test is shown. During the test, two of the calibration files (tst1.txt and tst2.txt), saved in the measurement process and described in Section C, are loaded at the beginning of the program. The input signals from the master path are initiated and the data acquisition (DAQ) device is set to the number 2 (the second slot of the chassis). The DAQ number of the slave path is set to 3 (the third slot of the chassis). The sampling rate is set to 1 MS/s (mega samples/sec), and the record length is set to 0.1 MS.

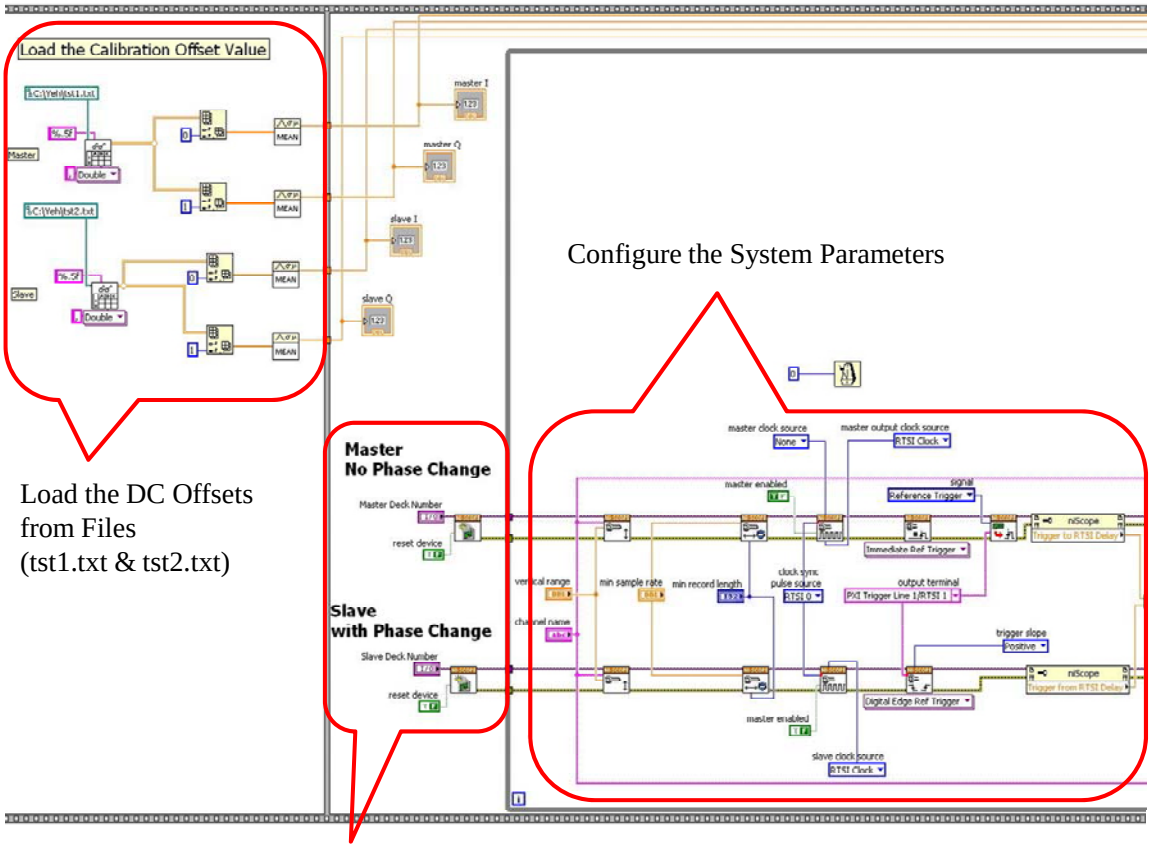

Figure 35. The first portion of the DF block diagram (after [10]).

The second part of the VI block diagram is shown in Figure 36. Both of the demodulator boards (TST1 and TST2) require removal of their DC offsets. The phase of the signals from the master path and slave path is passed to the RSNS Sub-VI to calculate the AOA. The phase difference, estimated AOA, phase difference of master, phase difference of slave and phase difference from the VNA are sequentially stored in an output file (df.txt).

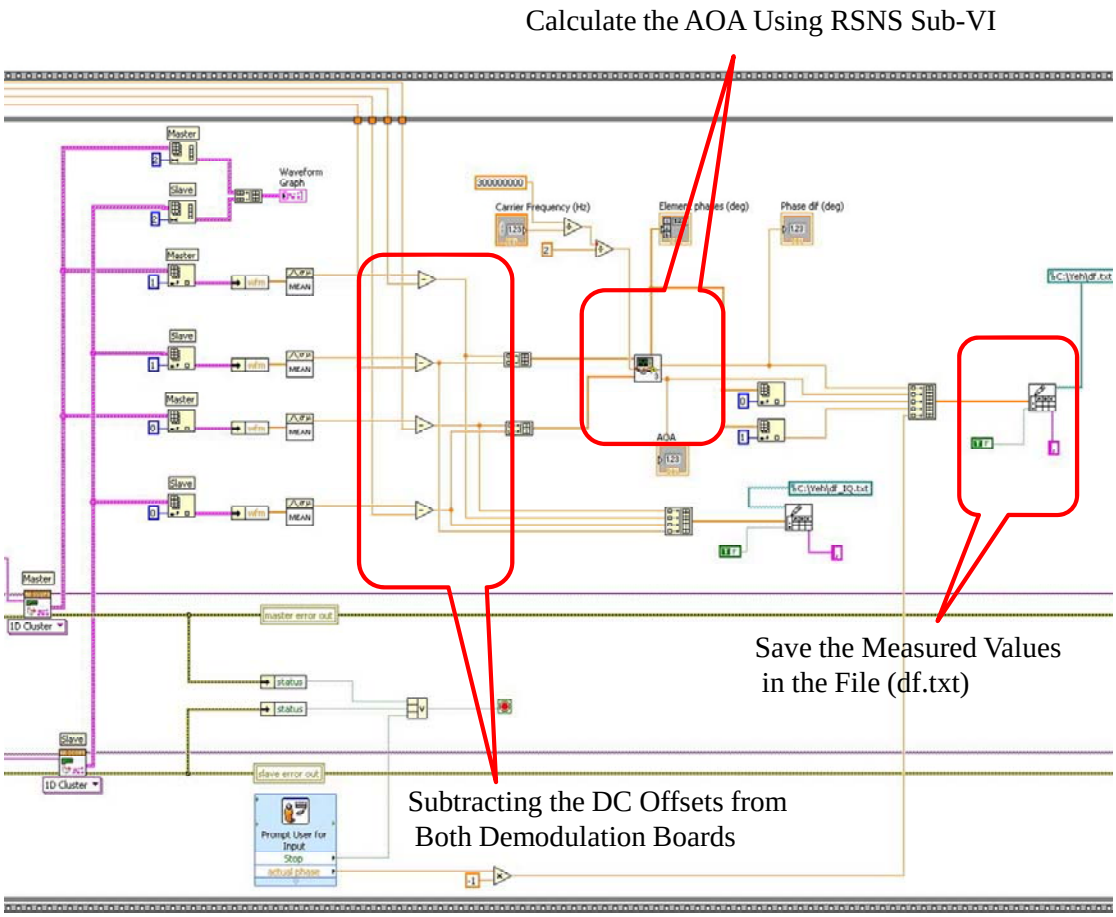

Figure 36. The second portion of the DF block diagram (after [10]).

The RSNS Sub-VI program was developed in [10]. This component takes the I and Q values from both of the paths (master and slave) and calculates the AOA. There are four parts in the RSNS algorithm as shown in Figure 37. In the first part, two of the I/Q pairs from the master and slave paths are used to calculate the phase difference. In the second part, the phase differences are used to generate the folding waveforms. In the third part, the folding waveforms of each channel are compared with the RSNS thresholds. Finally, the thresholded outputs are compared to the RSNS code to estimate the AOA.

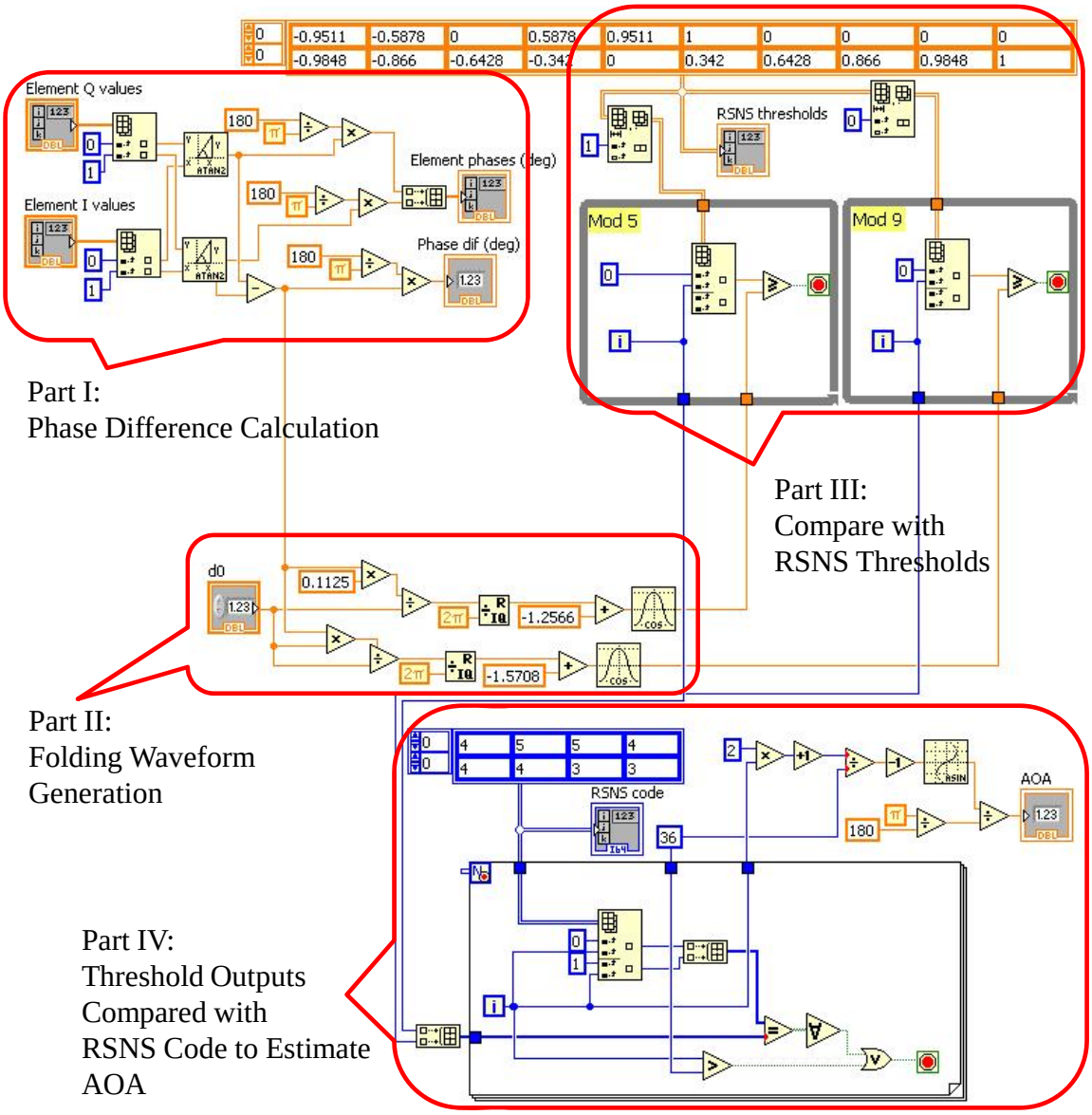

Figure 37. Sub-VI of RSNS algorithm (after [10]).

The third part of the VI block diagram is shown in Figure 38. The saved file from the second part is loaded. An embedded MATLAB script is used to plot the actual phase difference versus the measured phase difference. Another simulated AOA versus estimated AOA graph is plotted on the front panel. Both of the results are discussed in more detail in Section E.

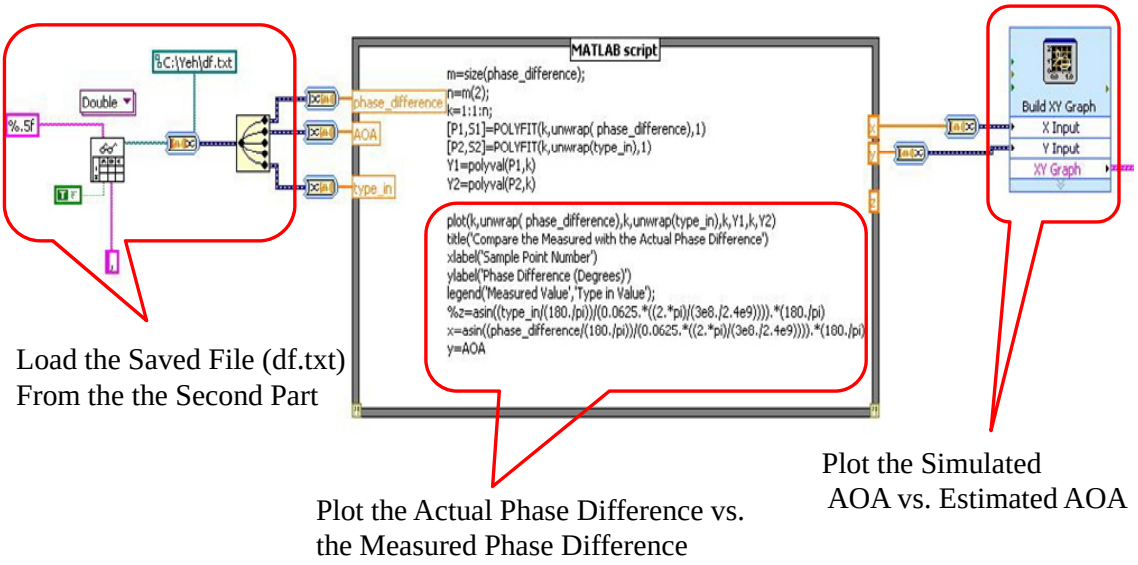

Figure 38. The third portion of the DF block diagram (after [10]).

E. BENCHTOP TEST RESULTS

In this section, the measured values from the DF benchtop testing platform, shown previously in Figure 27, are examined and analyzed, along with the measured values from network analyzer. The results shown in Figure 39 are typical of the simulated AOA (from VNA phase) versus the estimated AOA (from RSNS DF) extracted from the front panel of the DF program. The test data was obtained by shifting the phase shifters in one turn steps through 360° to simulate the signals from the emitter arriving at different angles. From this figure, the RSNS transfer function steps are vaguely observed along the diagonal line, similar to those seen in Figure 25.

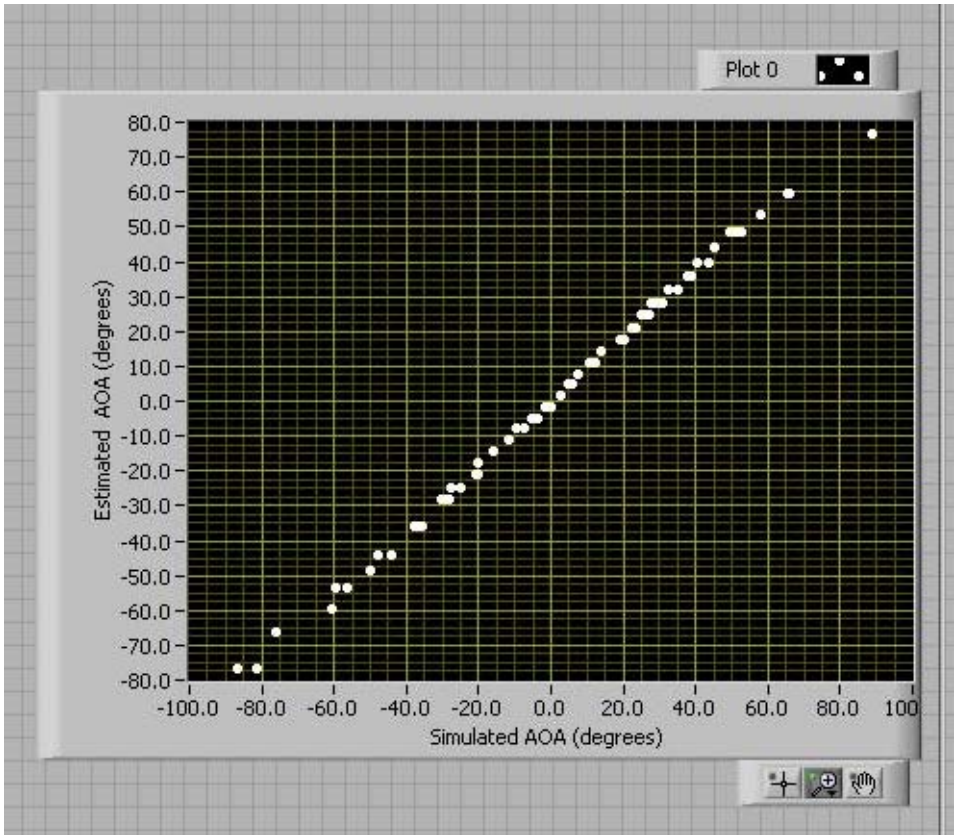

Figure 39. Simulated AOA vs. estimated AOA from DF testing platform.

The measured values stored in the output file (df.txt) are extracted and plotted with the RSNS transfer function for moduli [5, 9] in Figure 40. The estimated AOAs from the DF testing platform are overlapped with the theoretical RSNS AOAs. Based on these results, it can be concluded that the simulated signals with phase changes could be successfully transformed to the AOA values.

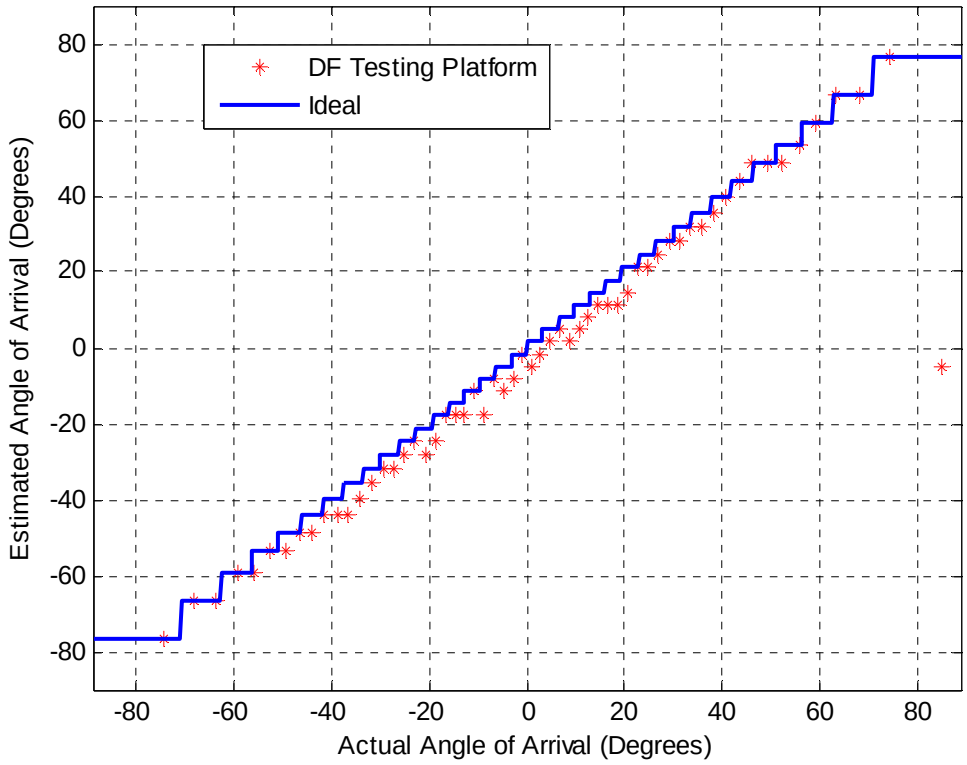

Figure 40. Comparison of ideal RSNS vs. DF testing platform.

To determine if the phase differences obtained from the I and Q values of the testing platform are in accordance with the phase differences measured by the network analyzer an analysis of the raw phase differences from the testing platform and the network analyzer are analyzed. These results are plotted in Figure 41. Note that there are break points around sample points 38 and 42 due to the phase cycles from -180° to 180°.

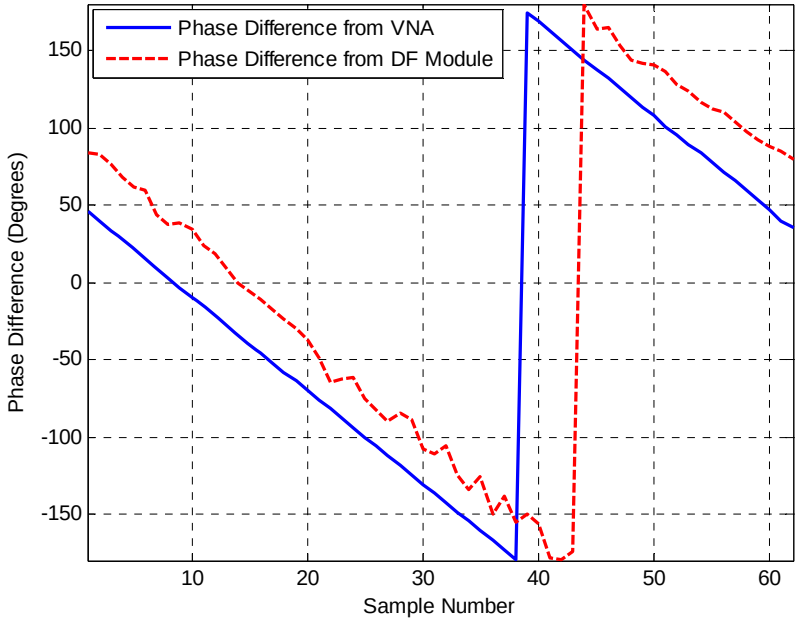

Figure 41. Phase difference of VNA and DF module.

After unwrapping the phase and centering the lines to the average phase values, a smoother phase plot is obtained and is shown in Figure 42. Both of these phase difference lines are almost matched to one another and they have the same slope when a least squares fit is applied.

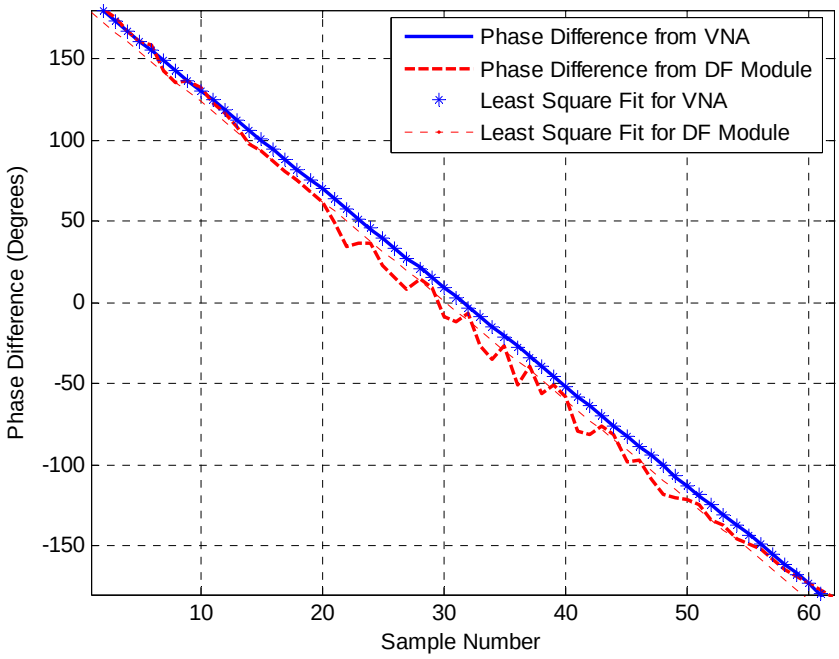

Figure 42. Phase difference of VNA and DF module with adjustment.

The actual AOA versus the AOA errors are compared and plotted in Figure 43 for the ideal RSNS, measured DF testing platform and network analyzer. The shift in measured data is likely due to demodulator calibration error.

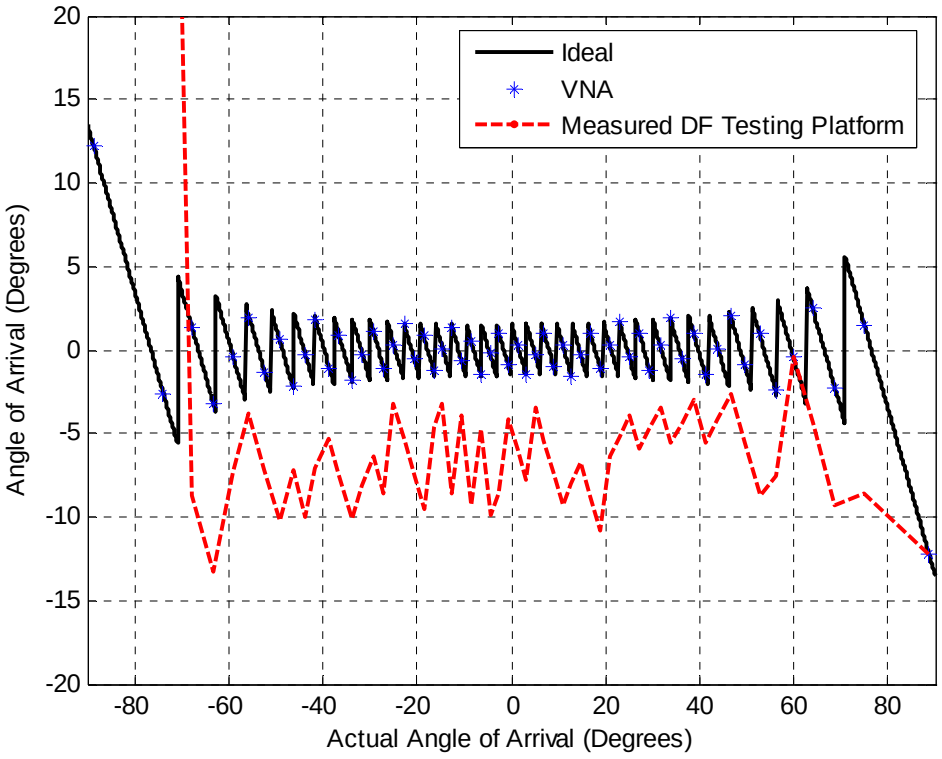

Figure 43. Comparisons of AOA errors from ideal, mesaured DF testing platform and VNA.

F. COMPARISON OF MEASURED AND SIMULATED DATA

In Section A, the ideal angle resolutions of moduli [5, 9] are derived from Equation (38) and plotted in Figure 26. In this section, different SNRs, varying from 10 dB to 90 dB, in increments of 20 dB, are simulated to observe their effects on angle error. The MATLAB file (virtualnoisejb.m) developed to simulate a plane wave incident from -90° to 90° with different SNRs added was modified [10] for this research. The input I and Q voltages for each element were set to 0 dBW and white Gaussian noise was added as

$$I = I + N_I \tag{39}$$

and

$$Q = Q + N_Q \tag{40}$$

where N_I is the noise added on the I channel and N_Q is the noise added on the Q channel. From [11], note that the monopulse difference beam has a linear region of approximately 20°. Therefore, the angle errors of the estimated AOA must be less than 20° for successful acquisition.

In Figure 44, actual AOA versus ideal (noiseless) AOA and versus the AOA for a SNR of 10 dB is shown. The maximum error between the ideal and 10 dB SNR cases is about $\pm 10^\circ$ at broadside but degrades at the two ends $\left(\pm 90^\circ\right)$.

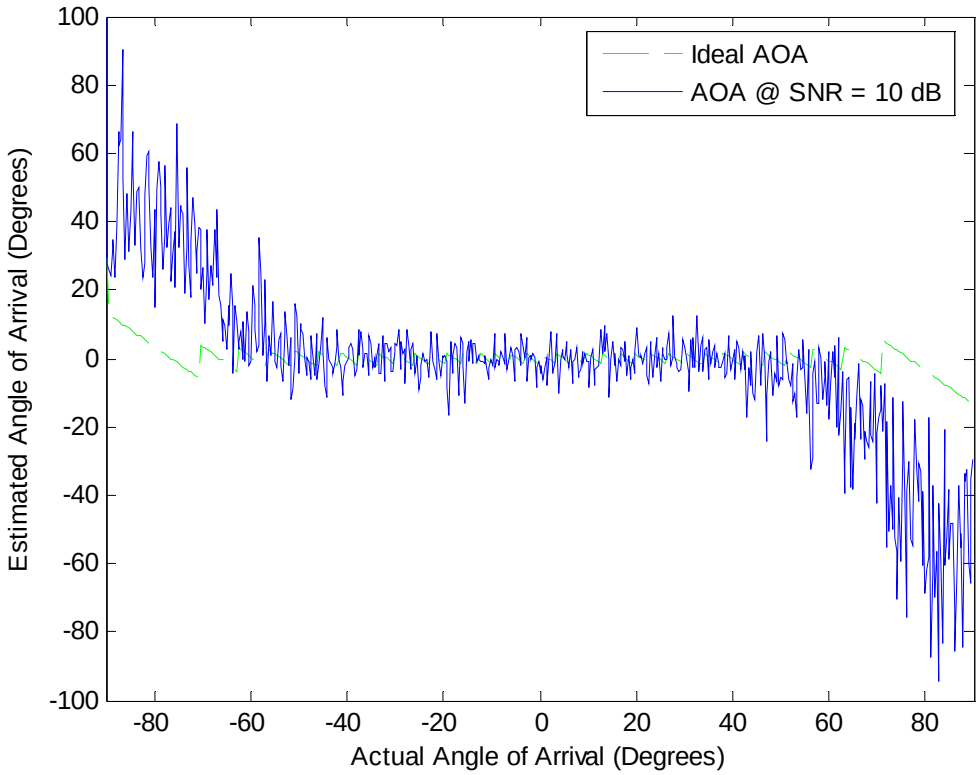

Figure 44. AOA error for noiseless and for SNR = 10 dB.

In Figure 45, actual AOA versus noiseless (ideal) AOA and versus the AOA for a SNR of 30 dB is shown. The maximum error between the ideal and 30 dB SNR cases is about $\pm 3^{\circ}$ at broadside and again degrades at the two ends $\left(\pm 90^{\circ}\right)$.

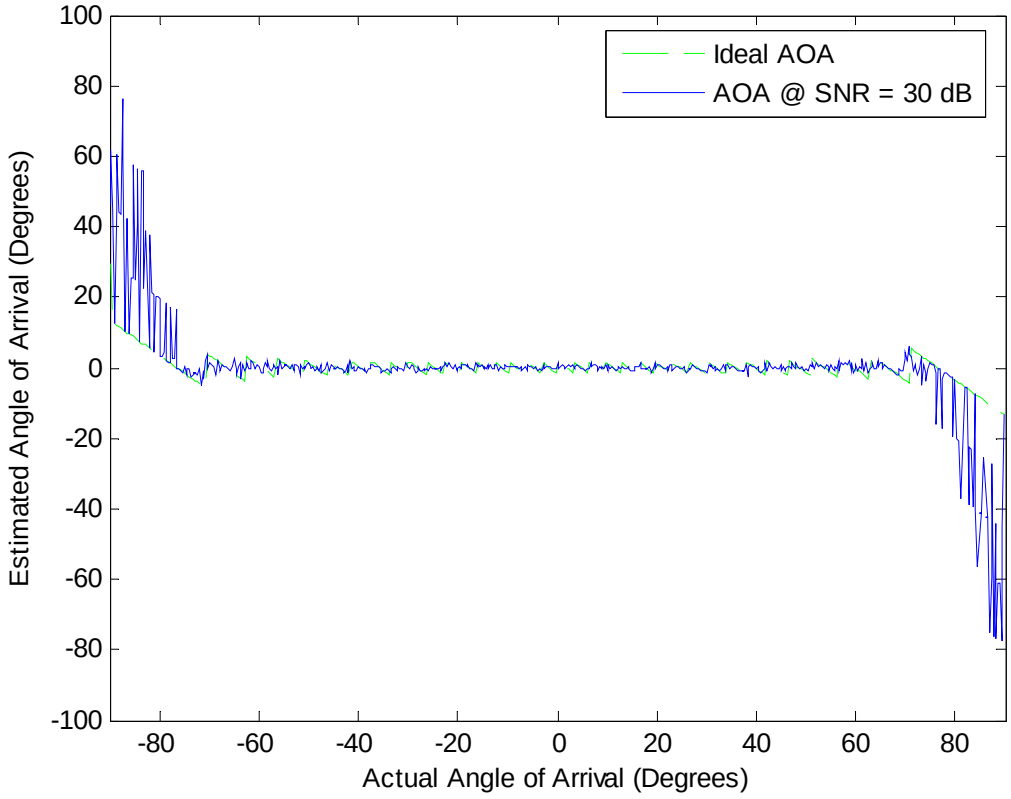

Figure 45. AOA error for noiseless and for SNR = 30 dB.

Figures 46 through 48 contain the corresponding results for SNRs of 50, 70 and 90 dB. The angle error continues to decrease as the SNR increases. At a SNR of 90 dB the performance is essentially ideal.

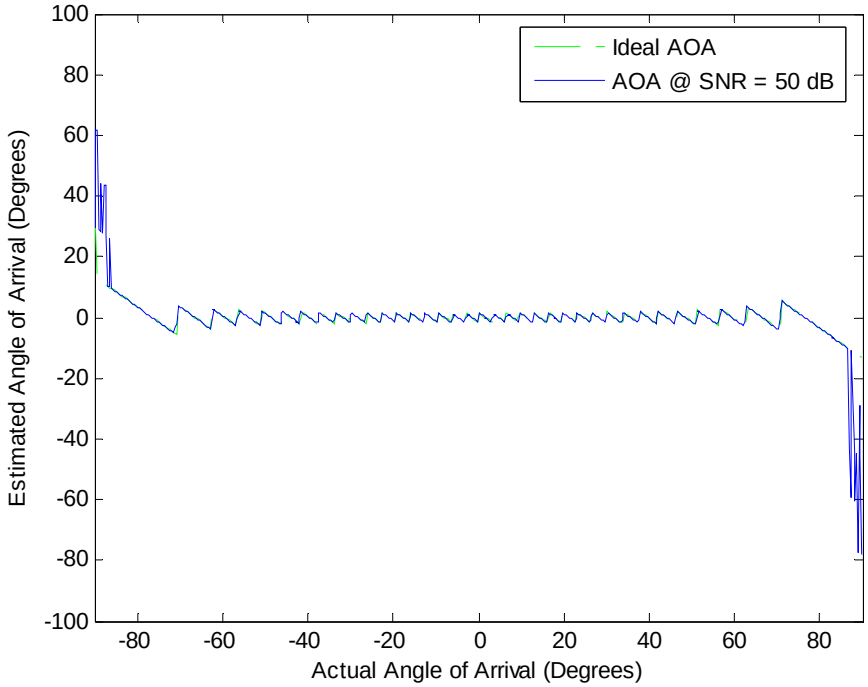

Figure 46. AOA error for noiseless and for SNR = 50 dB.

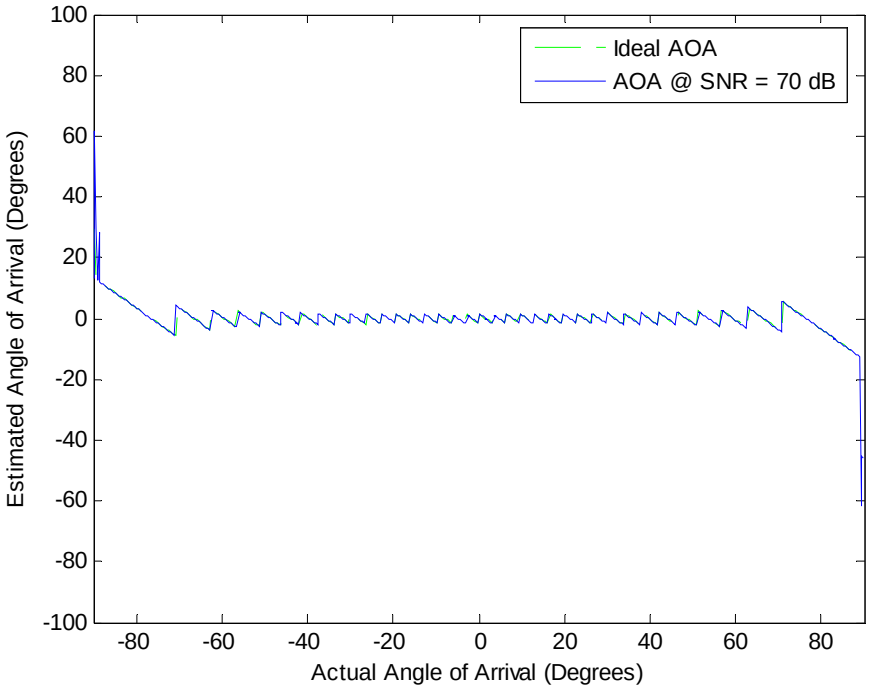

Figure 47. AOA error for noiseless and for SNR = 70 dB.

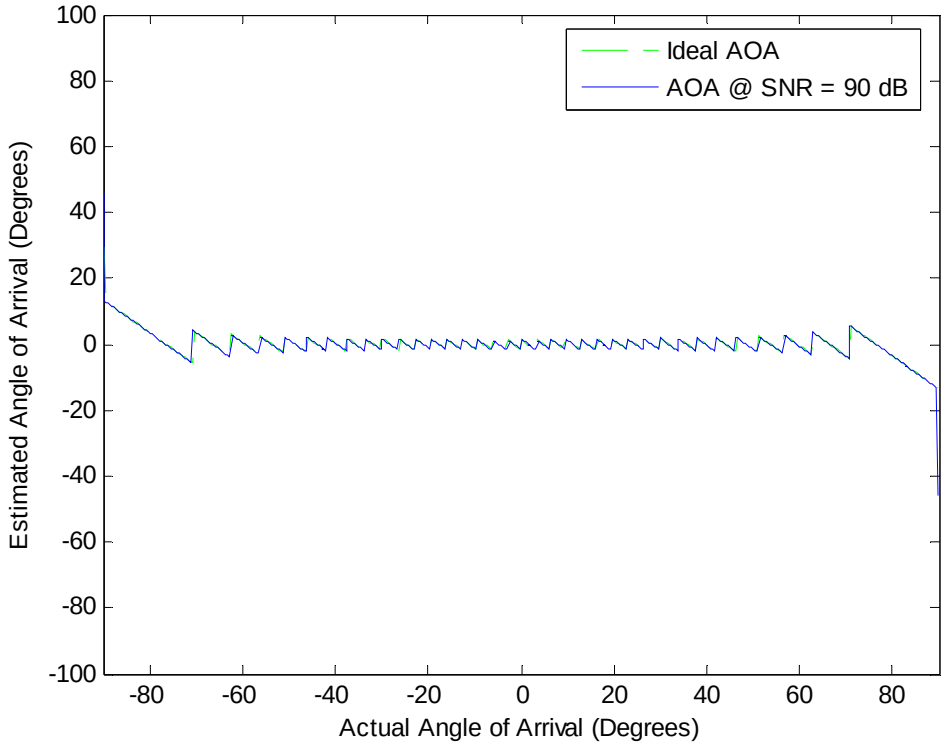

Figure 48. AOA error for noiseless and for SNR = 90 dB.

Monte Carlo simulation tests show that a SNR of approximately 30 dB is acceptable for the RSNS DF system to acquire accurate AOAs. For SNRs greater than 50 dB the performance is essentially ideal.

The design, simulation and benchtop test results for the RSNS DF algorithm were presented in this chapter. The integration of the antenna components and software and the system testing are addressed in the next chapter.

THIS PAGE INTENTIONALLY LEFT BLANK

V. INTEGRATED ARRAY SYSTEM HARDWARE AND SOFTWARE TESTING

The hardware of the digital tracking array with single-channel RSNS DF and monopulse DBF was assembled and tested. The angle measurements were taken in an anechoic chamber to reduce interference from multipath. The antenna under test was a six-element phased array. The structure of the phased array and the theory of monopulse DBF are elaborated and explained, and the hardware used in this tracking system is described. The tracking module was written in LabView and originally developed in [11]. It was modified and tested as described in Section C of Chapter V. Finally, the measurements and simulation results are analyzed and explained in Section F of Chapter V.

A. PROTOTYPE PHASED ARRAY DESCRIPTION

The six-element phased array used for angle tracking is shown in Figure 49. The array axis is aligned parallel to the *x*-axis. The *x*-*z* plane represents azimuth and the *y*-*z* plane represents elevation. Each elevation (vertical) subarray consists of two half-wave dipole antennas aligned in the *y*-axis. This subarray design can provide a higher gain than a single dipole, increasing the range and the angular accuracy. The spacing between subarrays is 0.0625 m, which is small enough to prevent grating lobes when scanned.

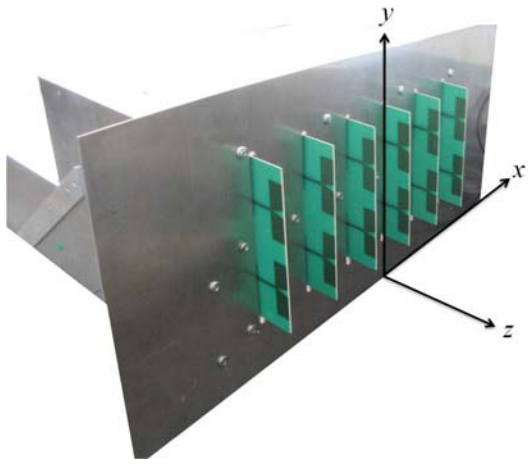

Figure 49. A six-element phased array.

The structure of each subarray is shown in Figure 50. Two half-wave dipole antennas and one microstrip power divider are printed on a thin, dielectric substrate of thickness $d_{substrate}$ and permittivity ε_r [24]. To make the current on the two arms of the dipole in phase, one of the paths is a half wavelength longer than the other (at 2.4 GHz). The parameters of the subarray are calculated in [11] and shown in Table 5.

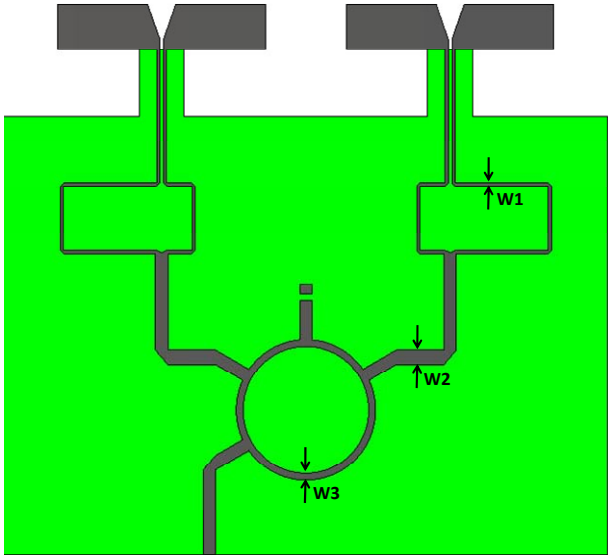

Figure 50. Layout of the elevation subarray (after [11]).

Table 5. Parameters of the elevation subarray (after [12]).

Gain (G)	5.16 (dB)
Azimuth HPBW (θ_B)	78°
Permittivity of the substrate (ε_r)	3.38
Thickness of the substrate $(d_{substrate})$	60 mils (1.52 mm)
Trace width of the 180° splitter (W_1)	35.7 mils (0.91 mm)
Width of the rat-race hybrid feed lines (W_2)	139 mils (3.53 mm)
Width of the rat-race hybrid (W_3)	76.3 mils (1.94 mm)

From [3] the half-wave dipole has a directivity of 1.64 (2.15 dB). The subarray under consideration for this thesis has two half-wave dipoles, so the directivity is 3.28 (5.16 dB). Further, with the use of the ground plane, another 3 dB gain comes from the image. The total gain of the subarray is 8.16 dB. The gain of the six-element phased array was measured in [12] and has a gain of 14 dB, which is 1.95 dB lower than its theoretical value. The excess loss can be attributed to measurement system loss and subarray circuit board loss. The HPBW is 20.17° by using the approximation of $\theta_B = 0.88\lambda / D$. The measured azimuth radiation pattern of the six-element phased array is shown in Figure 51.

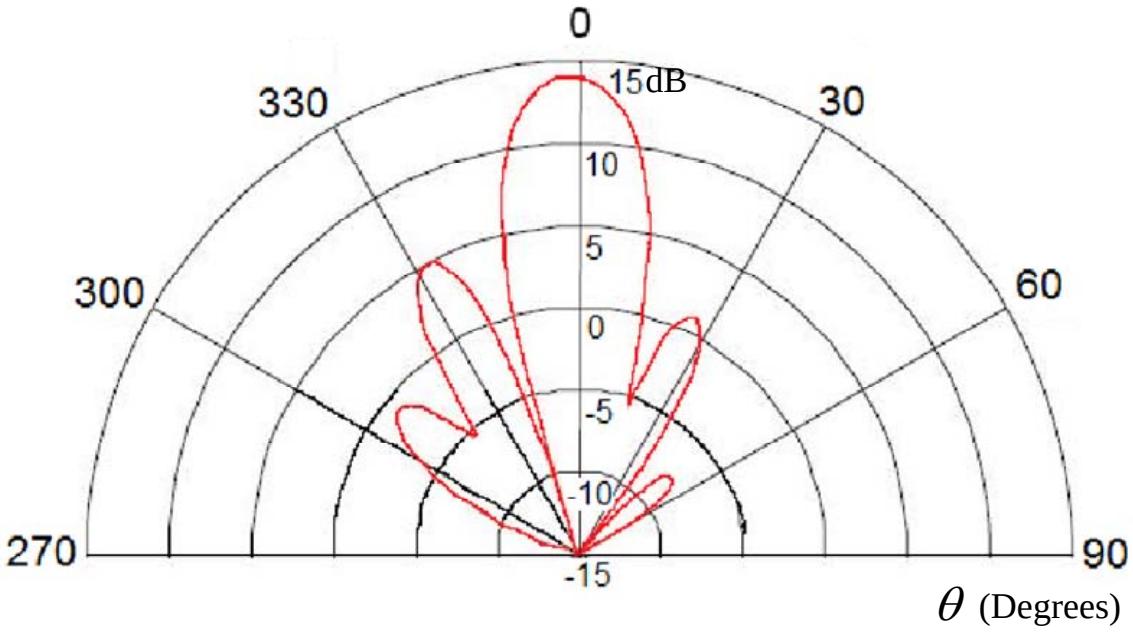

Figure 51. Measured radiation pattern of a six-element phased array in azimuth (after [12]).

The main beam of the radiation pattern is at $\theta = 0^\circ$. The asymmetrical radiation pattern is primarily due to the asymmetrical shape of the anechoic chamber. A reflecting ground plane (visible in Figure 49) is used to diminish the rear radiation and constrains the FOV from –90° to 90°. The spacing between subarrays equal to $\lambda / 2$, which is 0.0625 m at 2.4 GHz.

B. DIGITAL BEAMFORMING

Digital phased arrays form their beams in a beamforming computer (digital beamformer). The phase shifting of each array element is controlled by the DBF, therefore, the array scans at the speed of the processor.

Let there be N elevation subarrays positioned along the *x*-axis as shown in Figure 52. For the following analysis it is assumed that N is even.

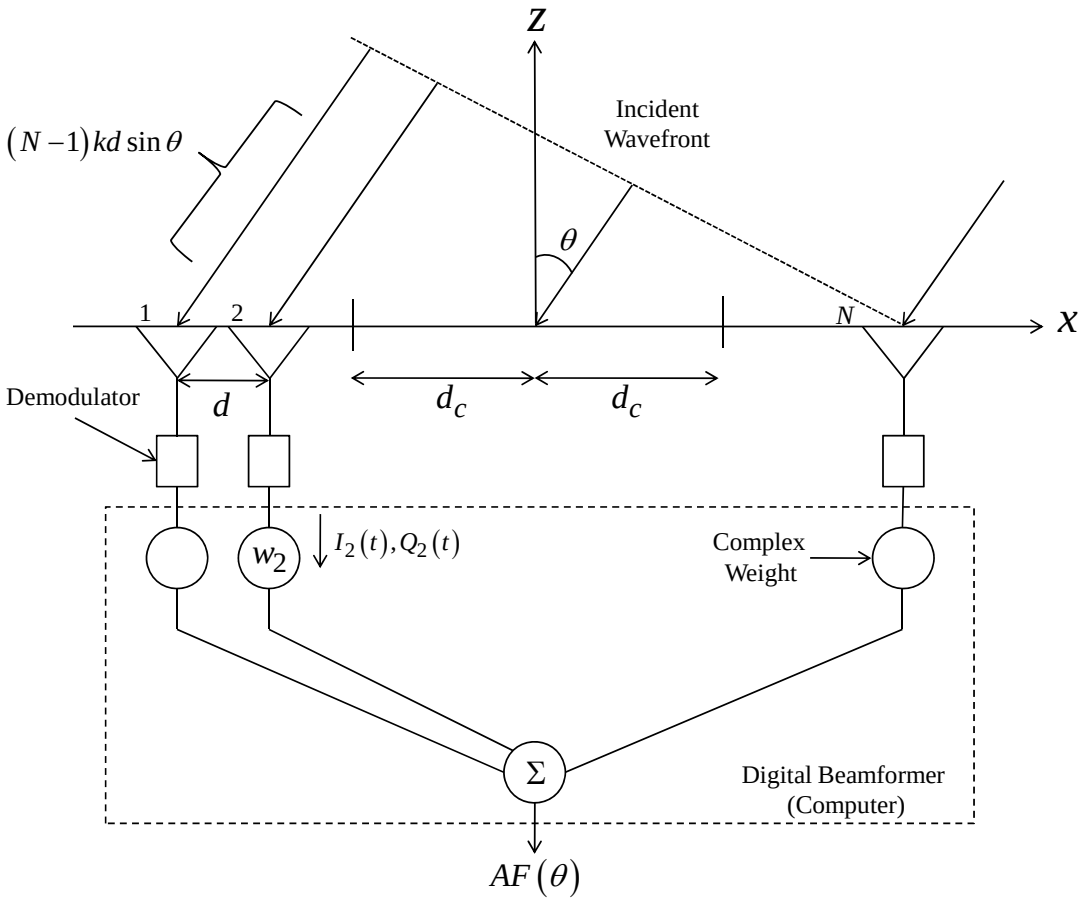

Figure 52. Digital phased array azimuth beamforming on reception (after [25]).

Let d_n be the element n location on the *x*-axis $(n = 1, 2, ..., N)$ so that the array is centered at the origin with inter-element spacing d. Therefore, d_n can be expressed as

$$d_n = \frac{2n-(N+1)}{2} d. \tag{41}$$

The array factor of the one-dimensioned linear array can be expressed as [5]

$$AF(\theta) = \sum_{n=1}^{N} w_n e^{jkd_n \sin\theta} = \sum_{n=1}^{N} A_n e^{j\alpha_n} e^{jkd_n \sin\theta} \tag{42}$$

where w_n is the complex weight, A_n is the amplitude illumination (for a uniform array, $A_n = 1$), and α_n is the n^{th} element phase weight. The angle θ is the incoming plane wave direction relative to the *z* axis [3]. The phase α_n is given as

$$\alpha_n = -kd_n \sin\theta_s \tag{43}$$

where θ_s is the scan angle of the main beam [25].

The digital beamforming process is depicted in Figure 53. The array is split into two azimuth subarrays with $N/2$ elements each. The distance of the centers of the subarrays from the array center is

$$d_c = \frac{N}{4} d. \tag{44}$$

The subarray factor for an azimuth subarray is

$$SF = \frac{\sin\left[\dfrac{Nkd\left(\sin\theta - \sin\theta_s\right)}{4}\right]}{\sin\left[\dfrac{kd\left(\sin\theta - \sin\theta_s\right)}{2}\right]}. \tag{45}$$

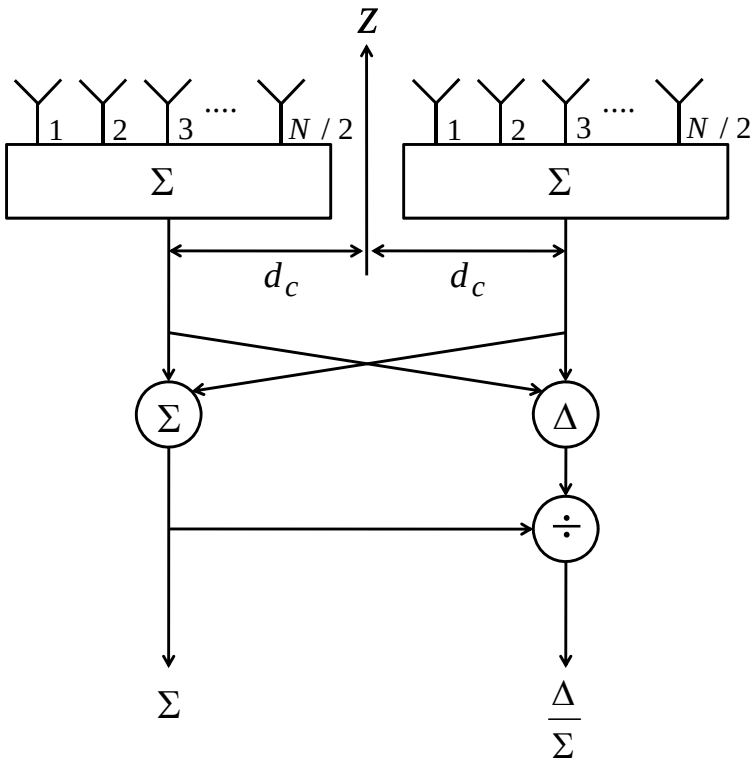

Figure 53. Sum and difference beamforming of monopulse (after [25]).

The subarrays are used to generate the sum and difference beams. From the principle of pattern multiplication [5], the sum and difference beams can be formed as

$$\begin{aligned}\Sigma &= SF \cdot e^{-jkd_c\left(\sin\theta-\sin\theta_s\right)} + SF \cdot e^{jkd_c\left(\sin\theta-\sin\theta_s\right)} \\ &= SF \cdot 2\cos\left[kd_c\left(\sin\theta-\sin\theta_s\right)\right]\end{aligned} \tag{46}$$

and

$$\begin{aligned}\Delta &= SF \cdot e^{-jkd_c\left(\sin\theta-\sin\theta_s\right)} - SF \cdot e^{jkd_c\left(\sin\theta-\sin\theta_s\right)} \\ &= SF \cdot 2j\sin\left[kd_c\left(\sin\theta-\sin\theta_s\right)\right].\end{aligned} \tag{47}$$

The difference over sum ratio is derived as

$$\frac{\Delta}{\Sigma} = \frac{SF \cdot e^{j\alpha_n}\left(2j\right)\sin\left[kd_c\left(\sin\theta-\sin\theta_s\right)\right]}{SF \cdot e^{j\alpha_n}2\cos\left[kd_c\left(\sin\theta-\sin\theta_s\right)\right]} = j\tan\left[kd_c\left(\sin\theta-\sin\theta_s\right)\right]. \tag{48}$$

Assuming $\left(\theta-\theta_s\right)$ is a small angle, we know that $\sin\theta-\sin\theta_s \approx \theta-\theta_s$ and $\tan\left[kd_c\left(\theta-\theta_s\right)\right] \approx kd_c\left(\theta-\theta_s\right)$ [26]. The difference over sum ratio can be simplified as

$$\frac{\Delta}{\Sigma} \approx kd_c\left(\theta - \theta_s\right) = K\left(\theta - \theta_s\right) \tag{49}$$

where K is the monopulse slope constant. The monopulse slope constant can be transformed to

$$K \approx kd_c = \frac{2\pi}{\lambda}\frac{N}{4}d = \frac{N\pi}{2}\frac{d}{\lambda} = \frac{0.88\lambda}{\theta_B}\left(\frac{\pi}{2\lambda}\right) = \frac{1.38}{\theta_B} \tag{50}$$

where $\theta_B \approx 0.88\lambda / D \approx 0.88\lambda / Nd$ [26]. This formula is accurate near broadside. However, at wide scan angles the slope decreases significantly due to a reduction in the array's projected aperture. To compensate, the constant can be modified by multiplying by $\cos\theta_s$ [26].

The I_n and Q_n values out of the demodulators are used to form the array response. Ideally, when a wave is incident from the direction θ,

$$I_n = \cos\left(jkd_n \sin\theta\right) \tag{51}$$

and

$$Q_n = \sin\left(jkd_n \sin\theta\right). \tag{52}$$

To form a beam in the direction of θ_s the processor must apply a complex weight of

$$w_n = A_n e^{j\alpha_n} = A_n e^{-jkd_n \sin\theta_s}. \tag{53}$$

The output of the DBF for the sum beam is [26]

$$\Sigma = \sum_{n=1}^{N} w_n\left(I_n + jQ_n\right) \tag{54}$$

and for the difference beam

$$\Delta = \sum_{n=1}^{N/2} w_n\left(I_n + jQ_n\right) - \sum_{n=(N/2)+1}^{N/2} w_n\left(I_n + jQ_n\right). \tag{55}$$

C. RSNS DF AND MONOPULSE DBF LABVIEW BEAMFORMING MODULE

The signals after the digitizer, PXI-5112, are transformed to digital format and the computer is used to form the beam and perform the tracking process. There are two

methods used to implement the tracking operations, one is continuous RSNS DF and the other is RSNS DF with monopulse DBF. The explanations of the RSNS DF and the monopulse DBF were presented in Chapter II and Chapter III. The module was developed in LabView and originally designed by [11]. Some new functions have been added and part of the control panel layout has been revised and modified.

There are four sections to this program. The first part initiates the input signals and configures the system parameters. The second part includes subtracting the DC offsets, adding phase adjustments, calculating the initial scan angle using the RSNS Sub-VI and computing the phase differences between adjacent elements. The third part is the digital beamformer, which calculates the difference over sum ratio and estimates the monopulse slope constant. The fourth part defines the angle error ranges, recalculates the scan angle from the angle error and then feeds data back to the starting point of the monopulse sequence, saving the measured values.

The front panel of the beamforming module is shown in Figure 54. There are two major sections to the front panel. The left side displays the configuration and results, which includes the calibration parameters of the array and the phase differences between elements during the testing. When the array is calibrated, the phase differences should be identical for an ideal plane wave arriving at broadside. The right block is the display and control zone, which includes an azimuth scan angle meter and a rectangular angle error meter. The lower-right panel is used to change the tracking modes and stop operation.

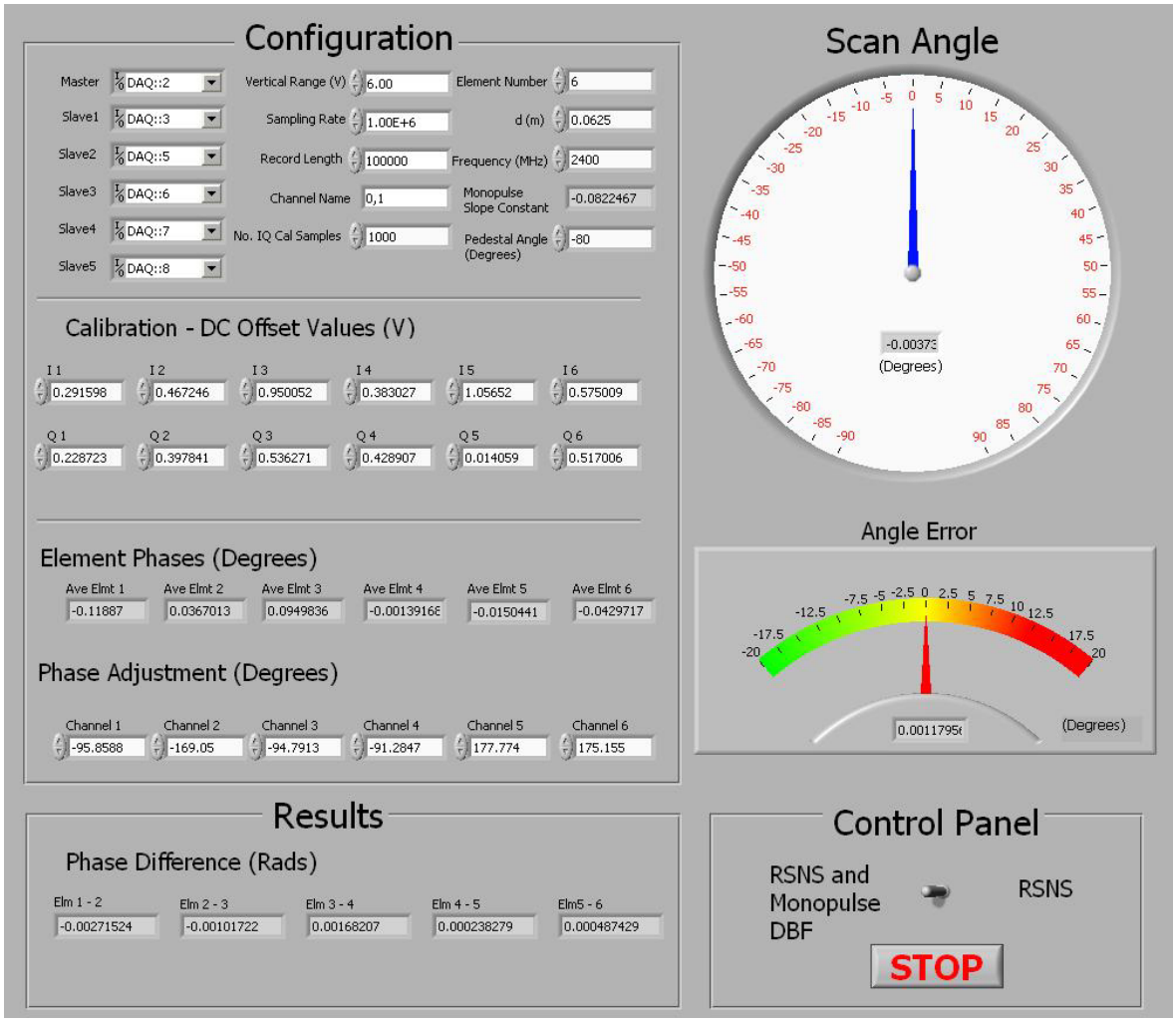

Figure 54. Front panel of the tracking module.

In Figure 55, the first portion of the VI block diagram used for the tracking process is shown. For brevity, only the master and two slave channels are shown. The I and Q signals output from the digitizers (six PXI-5112s) are the inputs to the process. The top path is set as the master (DAQ number to 2, the second slot of the computer, PXIe-1062Q) to perform as a reference trigger. Others paths are set as slaves (DAQ numbers are 3, 5, 6, 7 and 8, respectively). The sampling rate is set to 1 MS/s and the record length is set to 0.1 MS.

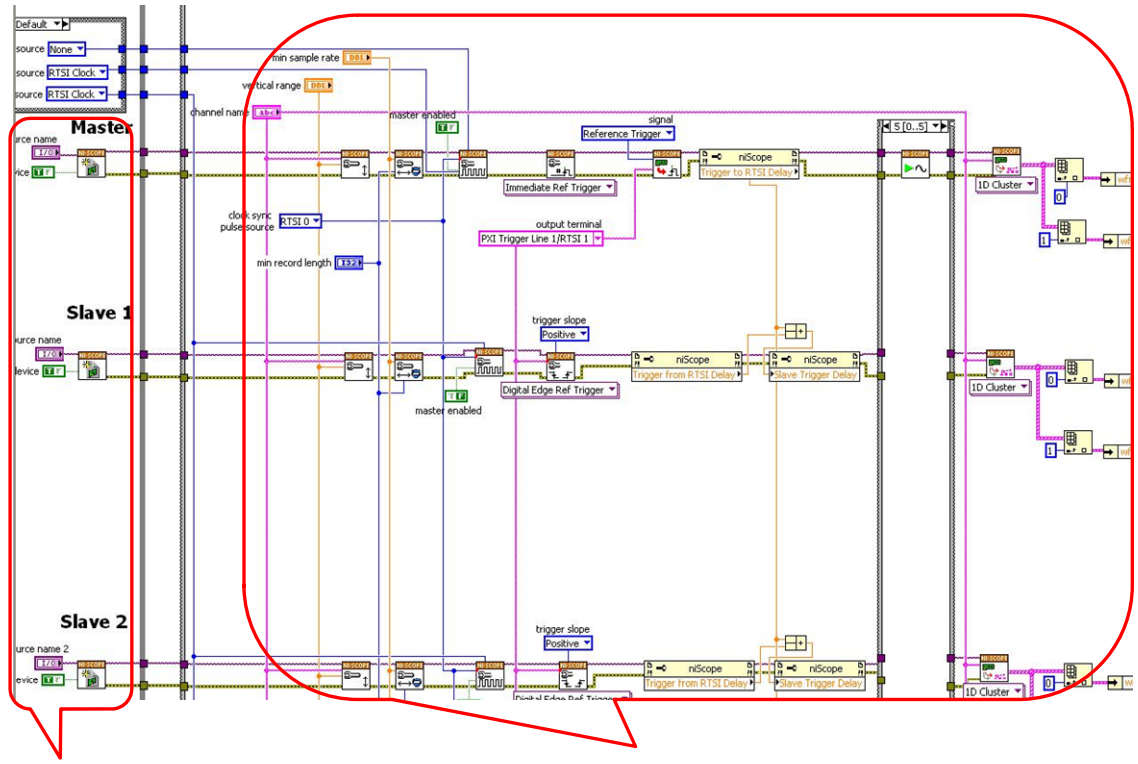

Figure 55. The first portion of the tracking system block diagram (after [11]).

The second part of the VI block diagram is shown in Figure 56 and only part of this portion is shown. The six demodulator boards must have their DC offsets removed. The procedure for offset calibration is described in Chapter IV, and the DC offset values were measured before the demodulators were installed. The phase differences from several combinations of elements (1-2, 2-3, 3-4, 4-5, 5-6) are averaged and passed to the RSNS Sub-VI to calculate the AOA. The averaging should reduce the effects of mutual coupling and any isolated channel phase errors. The monopulse uses the AOA as the initial scan angle of the emitter. In this testing, one phase difference (3-4), two combinations of three phase differences (2-3, 3-4, 4-5 and 1-2, 3-4, 5-6) and five phase differences (1-2, 2-3, 3-4, 4-5, 5-6) were compared to find the best estimate.

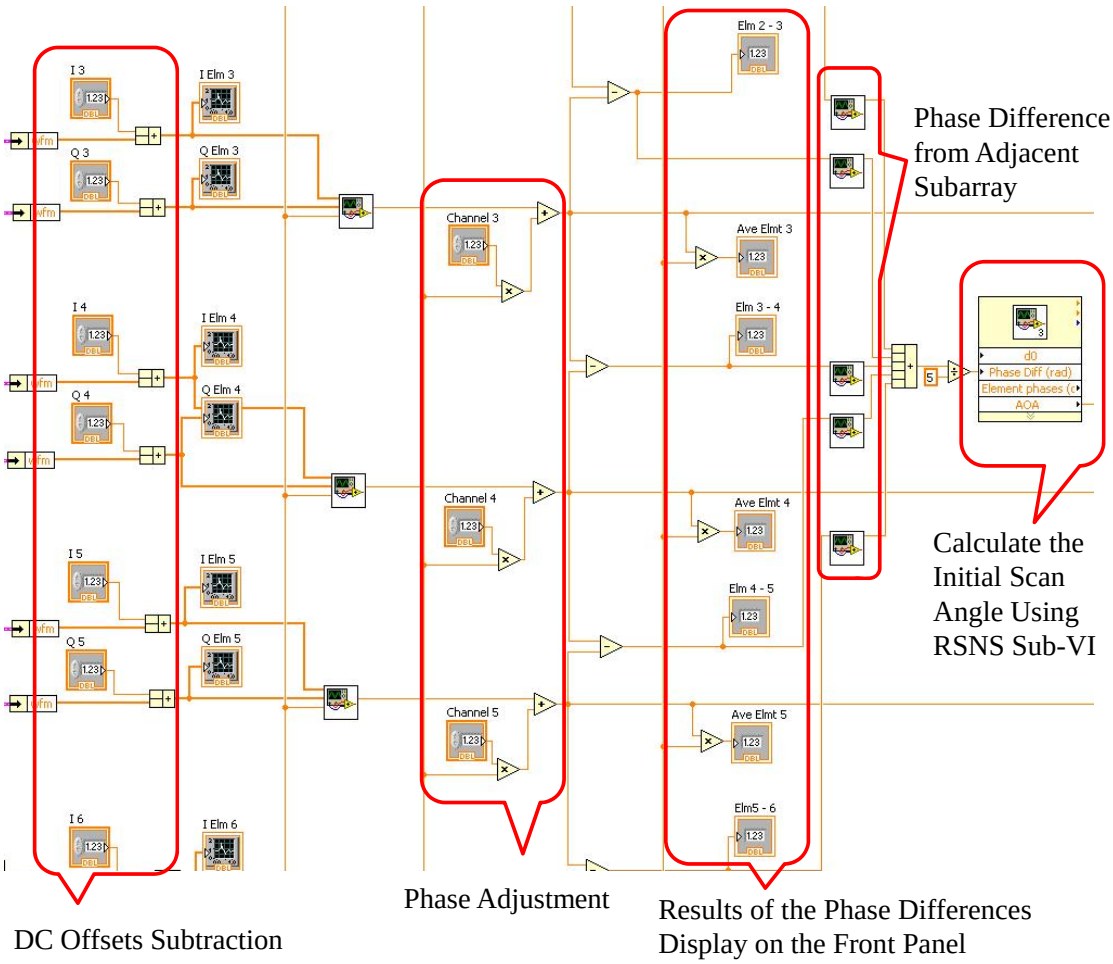

Figure 56. The second portion of the tracking system block diagram (after [11]).

Another important step in the second part is the initial phase adjustment. The six-element phased array is aligned with the horn antenna at the boresight. The incident wave is assumed to be a planar wavefront and hence the phases of each subarray are assumed to be equal. However, the phases of each subarray may be different, as shown in Figure 57. The phase differences are due to variations in the insertion phases of the RF devices in the individual channels, as well as the effects of mutual coupling. As shown, there is a 3.8° angle bias at broadside and other errors are expected at other measured angles.

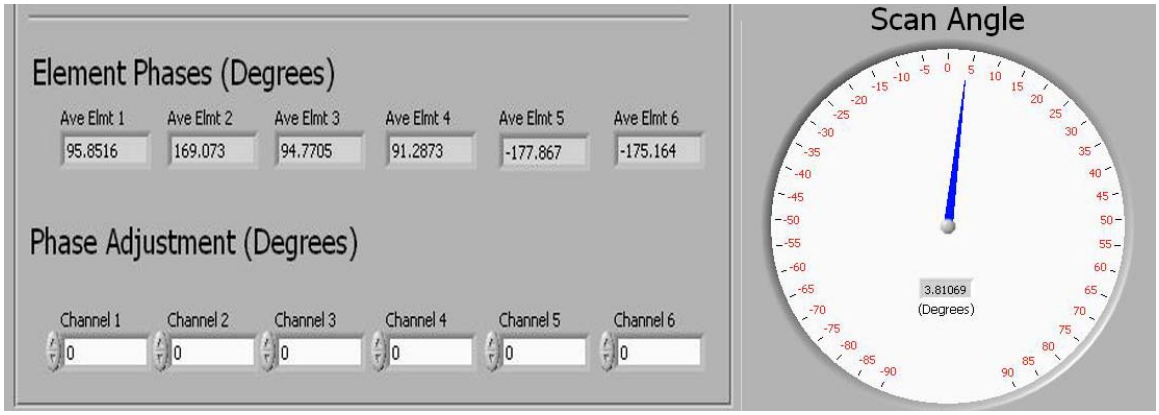

Figure 57. Display before phase adjustment.

These phase differences are recorded and then subtracted to give a common reference, which is 0° for the testing platform. The original angle bias is diminished as shown in Figure 58.

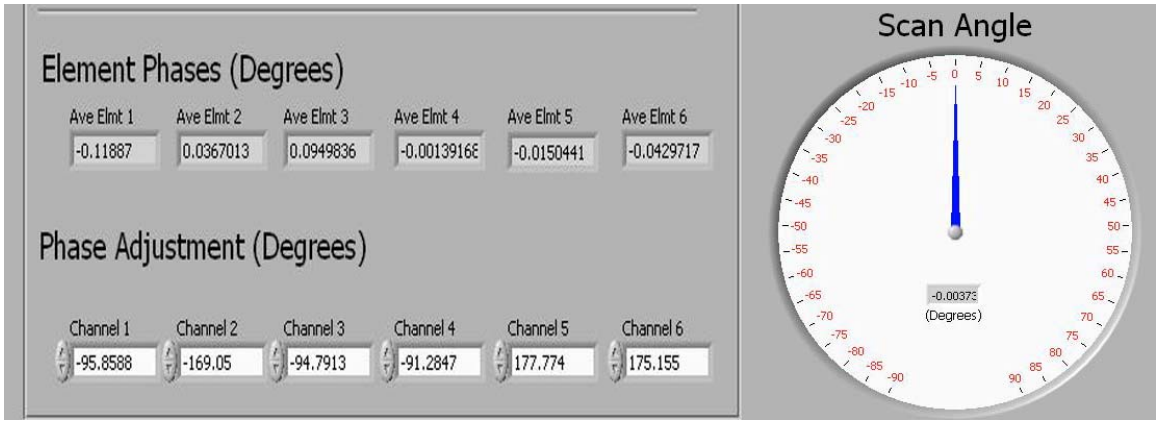

Figure 58. Display after phase adjustment.

The third part of the VI block diagram is shown in Figure 59. The subarray locations are calculated and provided as input arguments of the array factor Sub-VI. The array factor Sub-VI uses the phases with the subarray locations to construct the DBF. The beams of the six subarrays are divided into two subarray groups, which are referred to as left-subarray and right-subarray. For monopulse tracking, both the sum and difference beams are used for reception. The left-subarray adds the right-subarray to form the sum beam and the left-subarray subtracts the right-subarray to form the

difference beam. The difference over sum ratio is computed. The previous scan angle becomes the variable to estimate the monopulse slope constant and is divided by the difference over sum ratio to estimate the new scan angle.

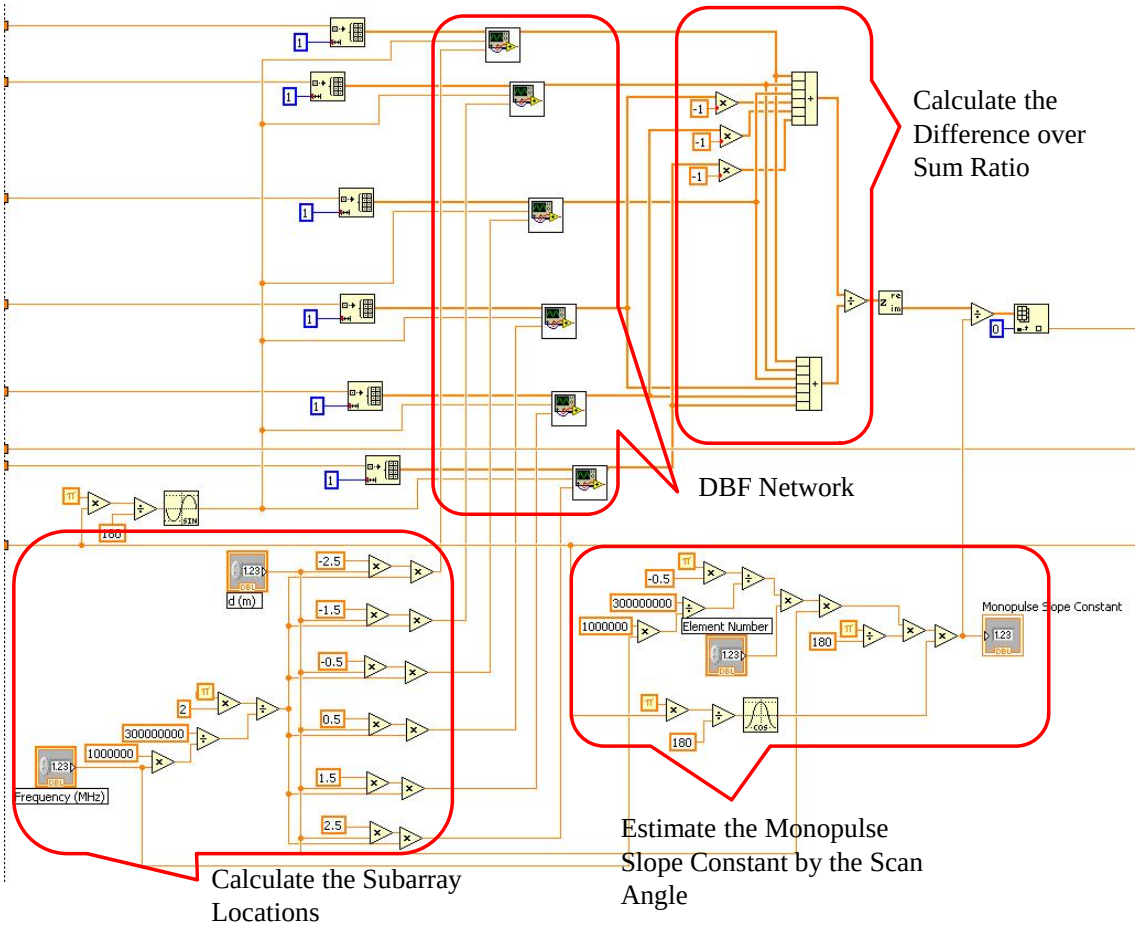

Figure 59. The third portion of the tracking system block diagram (after [11]).

The fourth part of the VI block diagram is shown in Figure 60. An angle error diagnostic function is built in to prevent track loss. If angle errors are more than the limits, the monopulse tracking will stop and jump back to RSNS DF to re-acquire a new scan angle. From [11], the monopulse has a total linear region of approximately 20°; therefore, the angle errors should be less than 20° to provide an accurate measurement. In the RSNS with monopulse DBF mode, the scan angle adds with the angle error and feeds the data back to the starting point of the monopulse sequence to become the new

monopulse scan angle. Finally, the index numbers, tracking mode numbers, scan angles, angle errors, RSNS AOAs and monopulse slope constants are stored sequentially in an output file (scan_angle.txt).

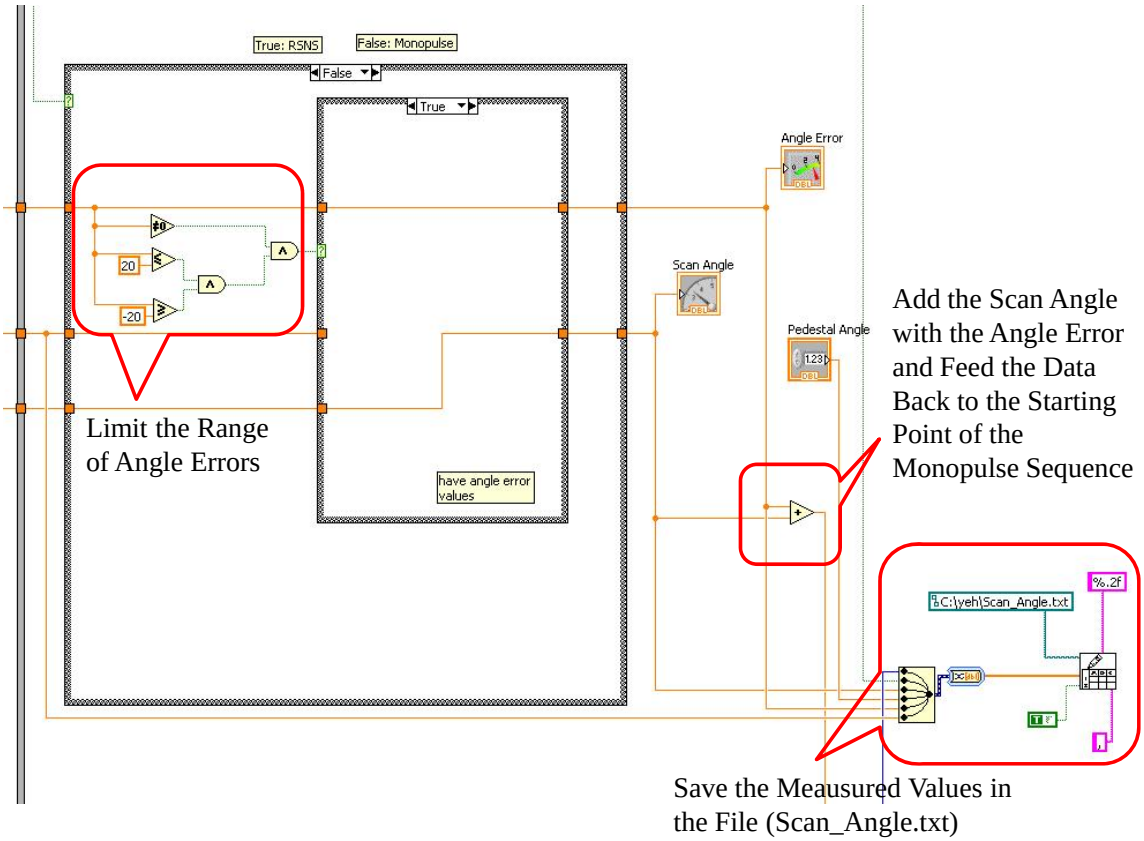

Figure 60. The fourth portion of the tracking system block diagram (after [11]).

D. FULL SYSTEM BENCHTOP HARDWARE TEST

Before testing the array in the chamber, a benchtop test was performed using a signal generator to simulate a signal transmitted from a UAV. A specially configured transmit antenna was used for the transmitter as displayed in Figure 61. The transmit antenna was surrounded by absorber material to limit the scattering of microwaves. The absorber material can be placed very close to an element ($\approx$1 inch) to act as a probe for diagnostic evaluation or several feet away to excite all of the array elements. If an

element is operating normally, the software displays voltage variations on the front panel. The purpose of this test was to check each element's functionality before conducting the tracking measurement in the chamber.

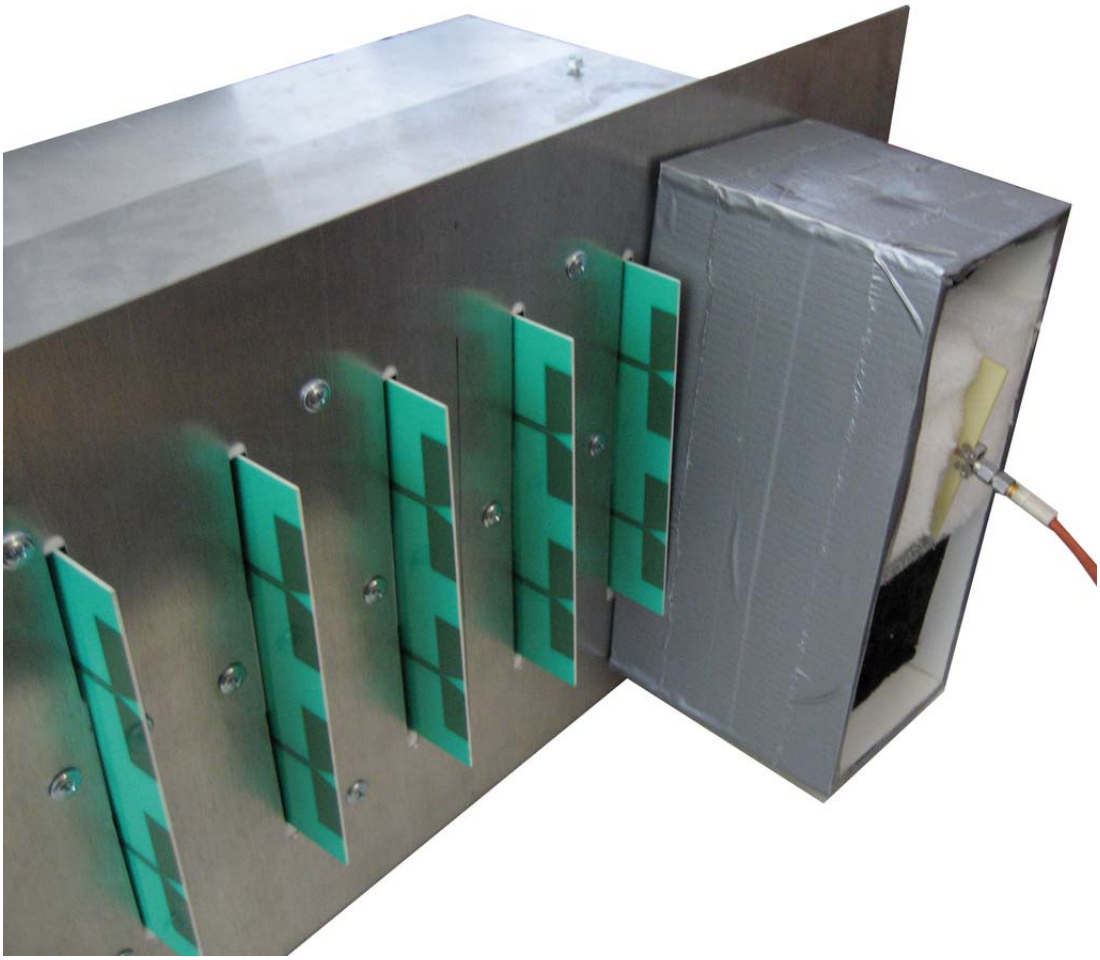

Figure 61. Diagnostic probe for the full system benchtop testing.

The return loss (S_{11}) of the probe at 2.4 GHz was measured and the results are shown in Figure 62. A return loss of 31.58 dB was measured.

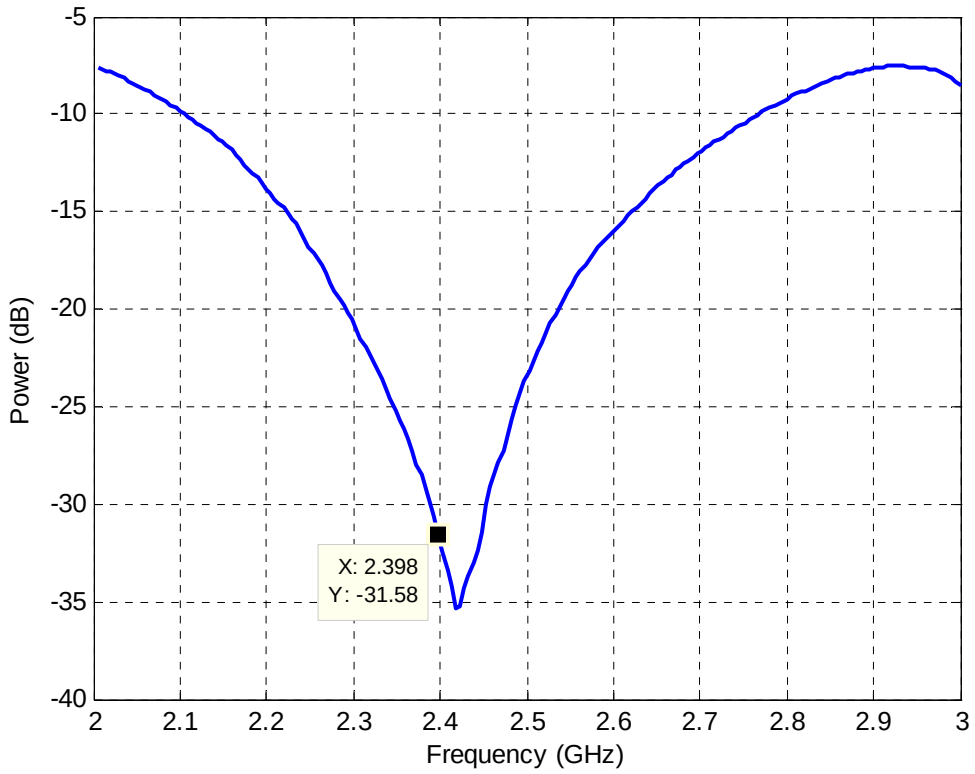

Figure 62. The S_{11} values of the probe at 2.4 GHz.

The emitted signals from the probe antenna simulate a UAV and were captured by the six-element phased array located on the benchtop. The incident signals were digitized and then processed using RNSN DF and monopulse DBF. The system block diagram, including hardware and software modules, is shown in Figure 63.

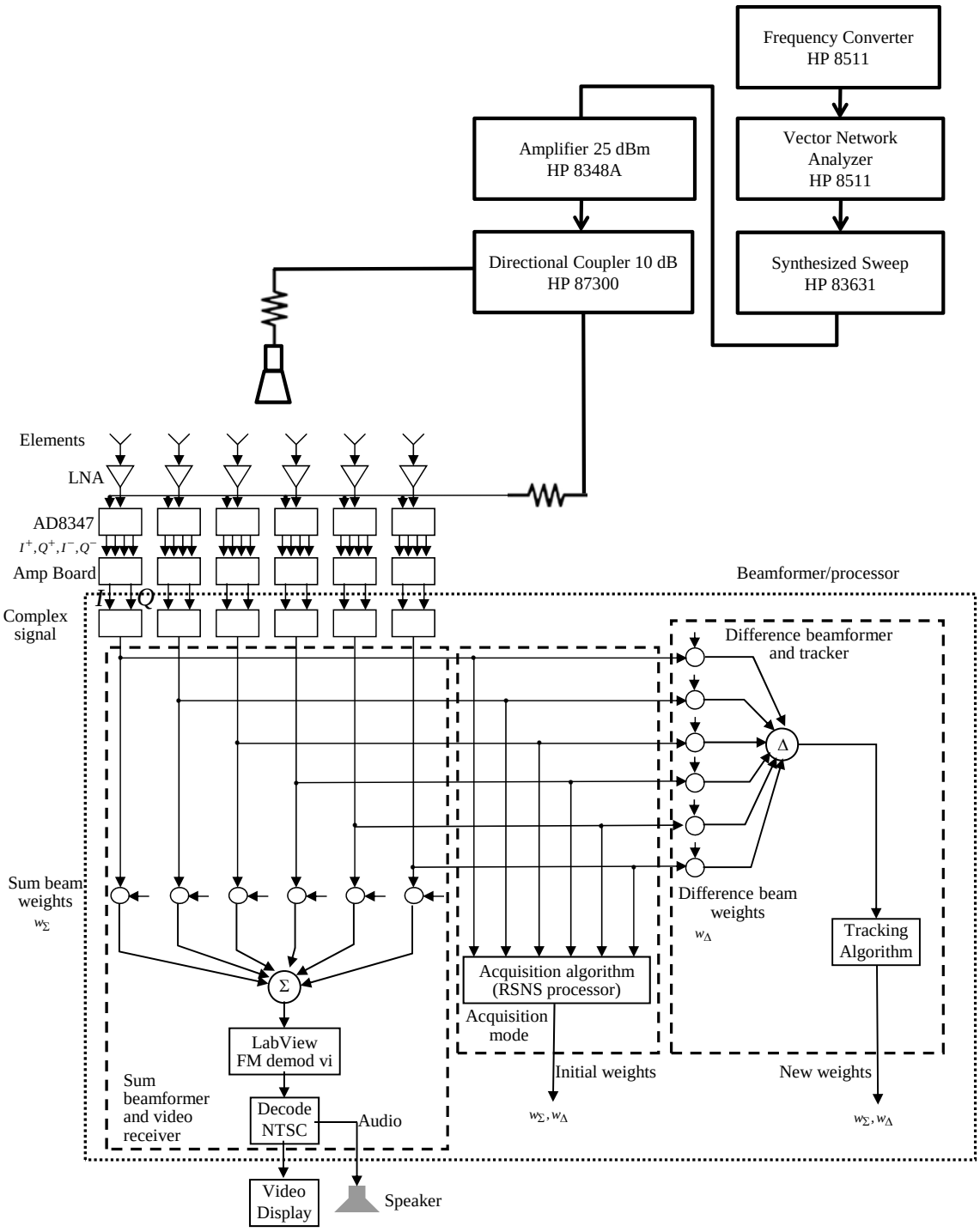

Figure 63. Complete block diagram of the digital tracking array configured for the benchtop system test (after [11]).

All hardware items were tagged in order to avoid misconnection between the elements and the digitizer cards. The detailed setup, including element name, DAQ number, channel number, DC offset values and path name in LabView are listed in Table 6.

Table 6. Mapping of antenna element to DAQ number, channel number, DC offset values and path name (after [11]).

Antenna	PXI-5112	Channel Number	DC Offset (V)	Path Name in LabView
Element 1	DAQ 2	0	I: 0.291598	Master
		1	Q: 0.228723	
Element 2	DAQ 3	0	I: 0.467246	Slave 1
		1	Q: 0.397841	
Element 3	DAQ 5	0	I: 0.950052	Slave 2
		1	Q: 0.536271	
Element 4	DAQ 6	0	I: 0.383027	Slave 3
		1	Q: 0.428907	
Element 5	DAQ 7	0	I: 1.05652	Slave 4
		1	Q: 0.014059	
Element 6	DAQ 8	0	I: 0.575009	Slave 5
		1	Q: 0.517006	

The main purpose of this benchtop system test was to implement the RSNS DF with monopulse DBF tracking system and demonstrate the operation of the testing platform. After several test cycles, it was determined that the system components and software were functioning. This enabled testing to proceed to the anechoic chamber.

E. ANECHOIC CHAMBER

The anechoic chamber can reduce the reflection of electromagnetic waves significantly and provide a low noise environment. It simulates the free space environment and also provides an environment to measure antenna radiation patterns and parameters such as HPBW and gain. The effects of multipath diminish the angle accuracy of measurements as explained in Chapter III. A tracking system needs to receive signals from the emitter without multipath interference to accurately determine the AOA. If there is reflection, an image may confuse the tracker causing loss of track [8].

A layout of the anechoic chamber at the Naval Postgraduate School (NPS) is shown in Figure 64.

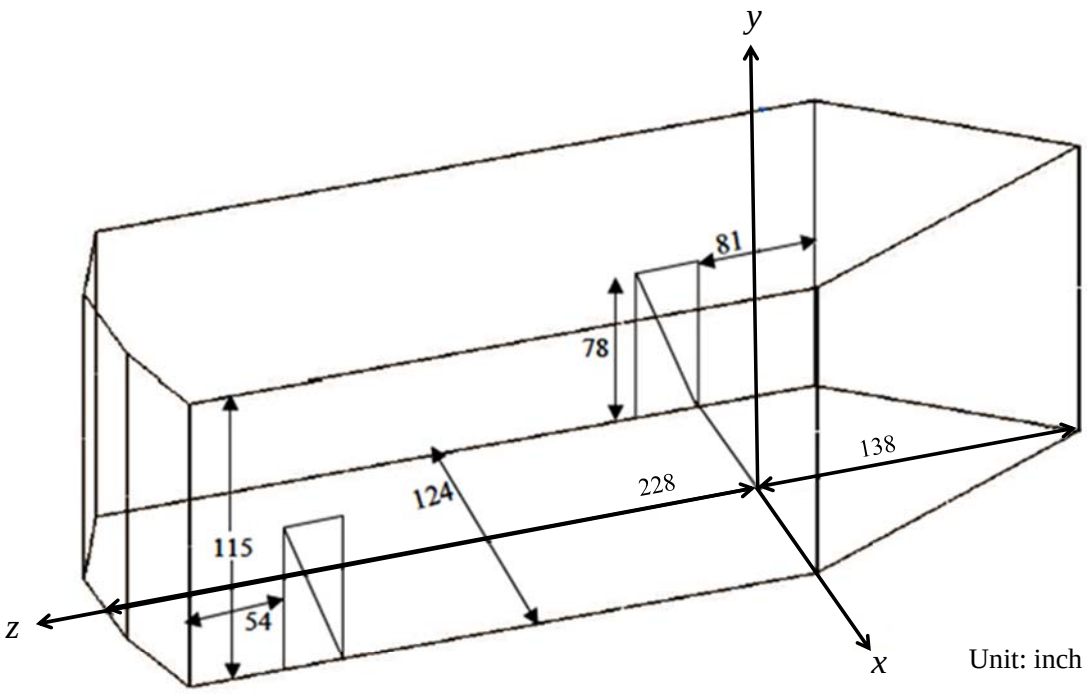

Figure 64. Anechoic chamber at the Naval Postgraduate School (after [11]).

The chamber is designed to operate above 3 GHz. Since the system demonstrated for this thesis is operated at 2.4 GHz, slightly higher reflection levels from the walls are experienced. Further, the chamber is not symmetrical in shape due to space constraints.

The distance between the transmit horn antenna and the phased array under test is 228 inches ($R = 5.8$ m). Recall that the three far-field conditions are [25]

$$R > 2D^2 / \lambda = 1.5625, \tag{56}$$

$$D >> \lambda = 0.125, \tag{57}$$

and

$$R >> \lambda = 0.125 \tag{58}$$

where D is the total length of the array $\left(D \approx (N-1)d\right)$. The testing platform is operated in the far-field, which means the wavefronts are spherical and there is a negligible radial component to the field [13].

In Figure 65, the transmit horn is shown connected to the VNA, which is located outside of the chamber. This horn simulates the emitter on a UAV. The six-element phased array is placed on a rotating pedestal facing the emitter, as shown in Figure 66.

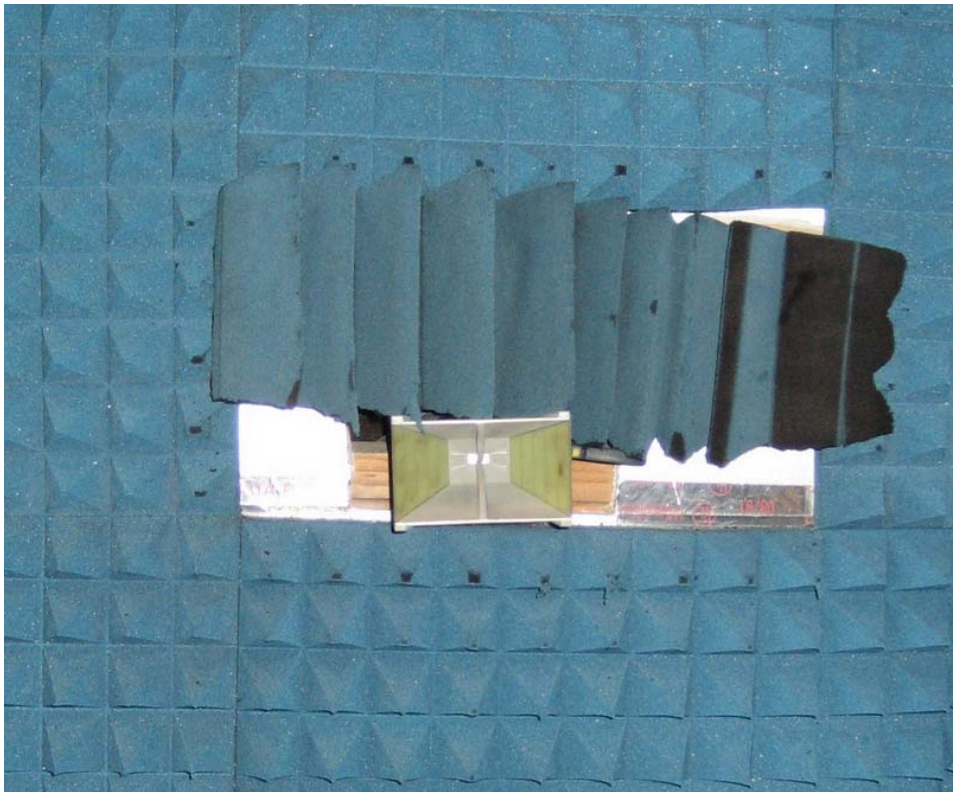

Figure 65. Horn antenna as the emitter.

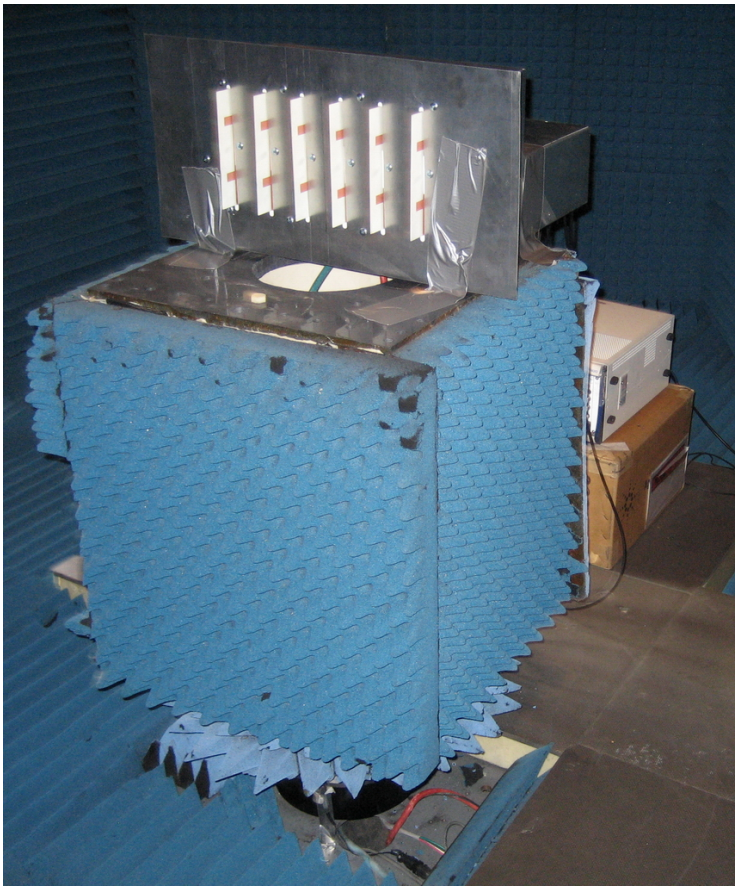

Figure 66. A six-element phased array placed on the pedestal.

The pedestal is operated by a servo computer and rotates from –80° to 80° to simulate the movement of a UAV [8]. Figure 67 is a block diagram of the equipment used in the anechoic chamber.

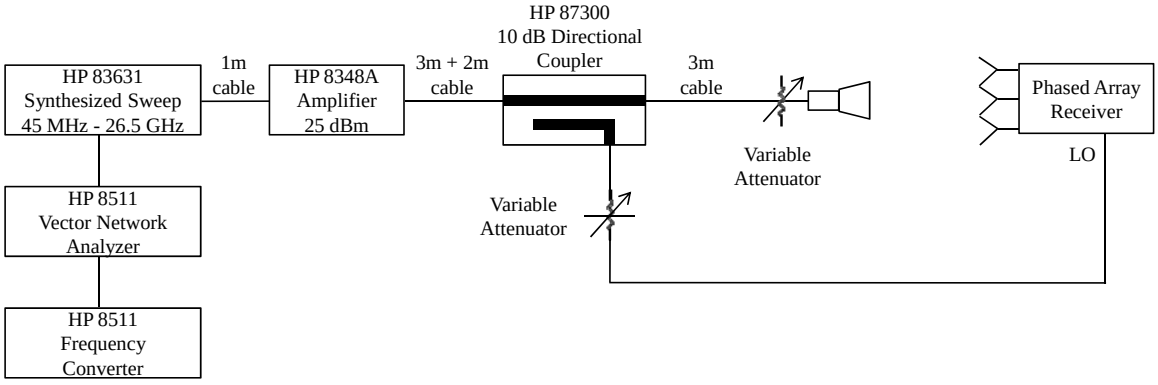

Figure 67. Block diagram of the equipment used in the anechoic chamber (from [11]).

F. CHAMBER TEST RESULTS

In this section, chamber measurements of the array tracking system are reported. Two tracking modes are presented over a range of operating parameters to examine their performance. The data collected is plotted and a comparison of the recorded tracking angles with the pedestal angles is made. The results are analyzed and the performance of the tracking system is determined.

The first part of the chamber test was to find out the maximum RSNS DF range. The initial scan angle provided by the RSNS DF limited the FOV of operation. If the RSNS DF cannot provide a close enough scan angle, the monopulse tracking cannot acquire the signal. The acceptable angle error in the series of tests was defined as less than 20° because within this range, monopulse tracking guarantees an accurate updated tracking angle. At the beginning of the test, the tracker's capability was unknown so a smaller FOV (from -80° to 80°) was tested. Further, a variety of element phase differences (one phase difference, or averaging three phase differences or five phase differences) were tested and comparisons provided. The goal in averaging the phase differences was to reduce the effect of errors in the individual channels, as well as mutual coupling. The results of the combined RSNS and monopulse DBF mode using one phase difference (elements 3-4), three phase differences (elements 1-2, 3-4, 5-6 and elements 2-3, 3-4, 4-5) and five phase differences (elements 1-2, 2-3, 3-4, 4-5, 5-6) with 1 degree steps are shown in Figures 68 to 71, respectively.

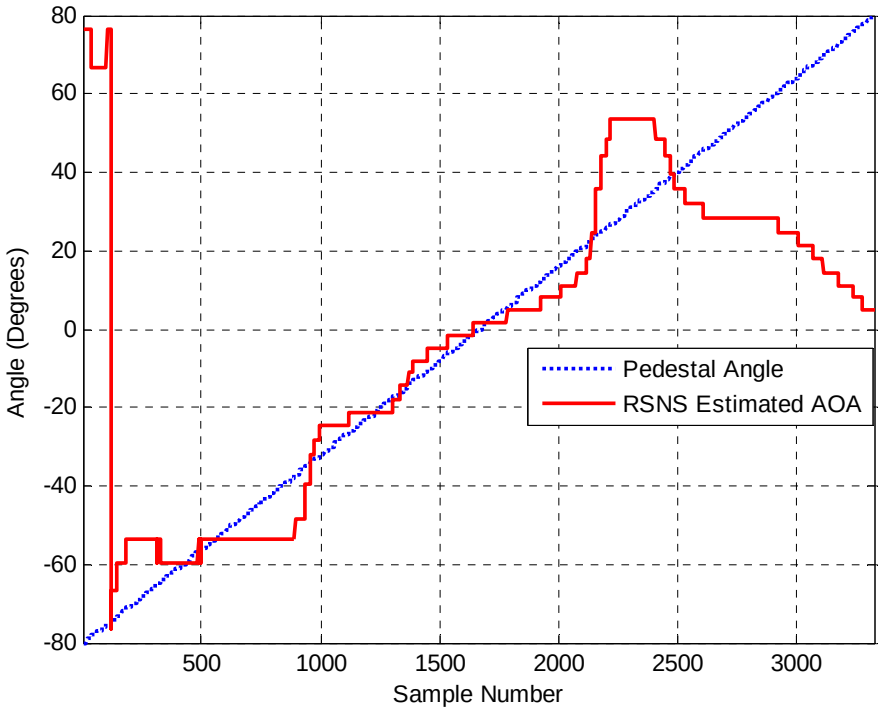

Figure 68. Tracking with RSNS mode using one phase difference (elements 3-4) and 1 degree steps.

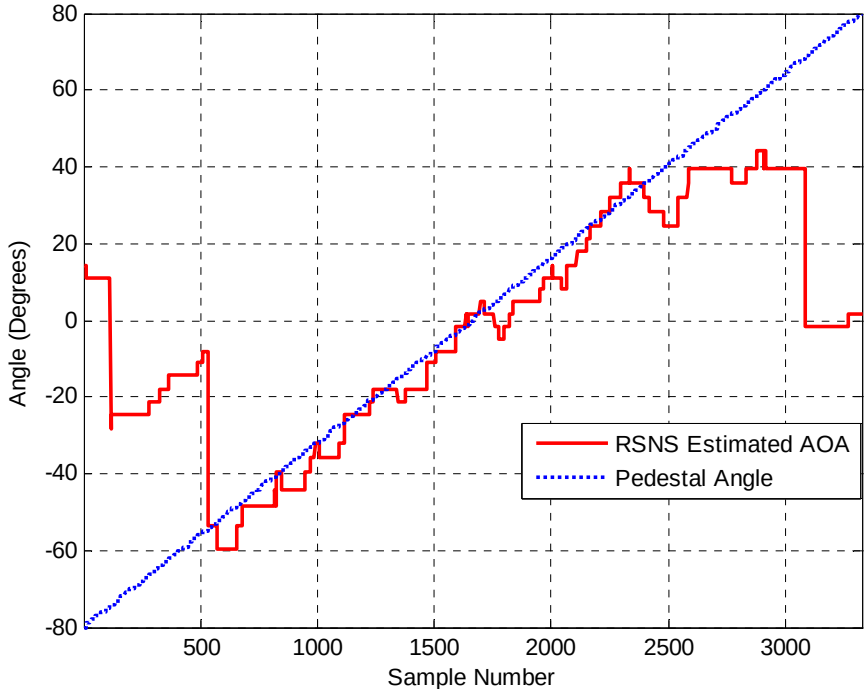

Figure 69. Tracking with RSNS mode using three phase differences (elements 1-2, 3-4, 5-6) and 1 degree steps.

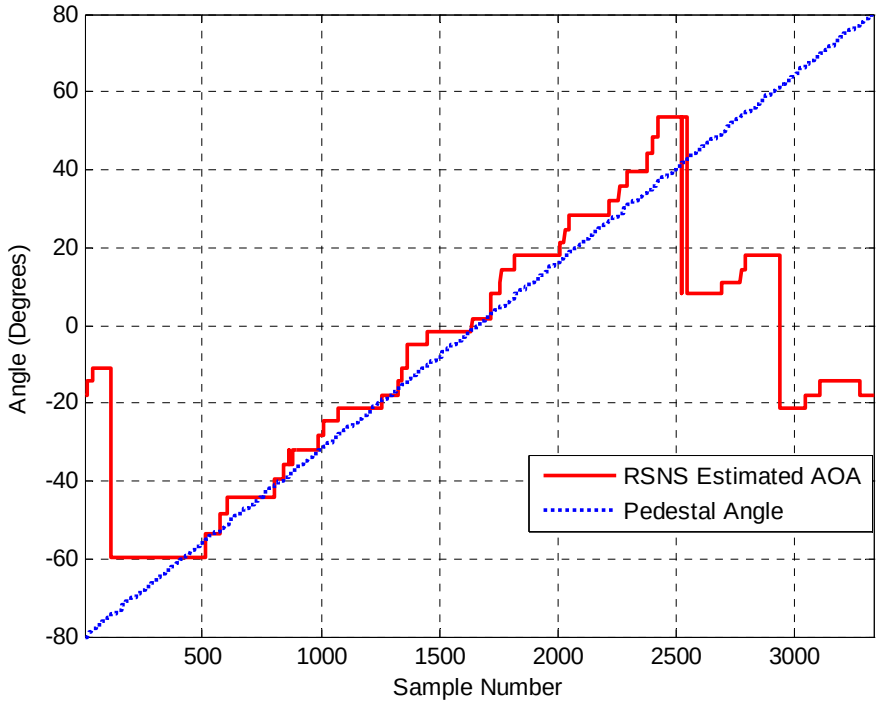

Figure 70. Tracking with RSNS mode using three phase differences (elements 2-3, 3-4, 4-5) and 1 degree steps.

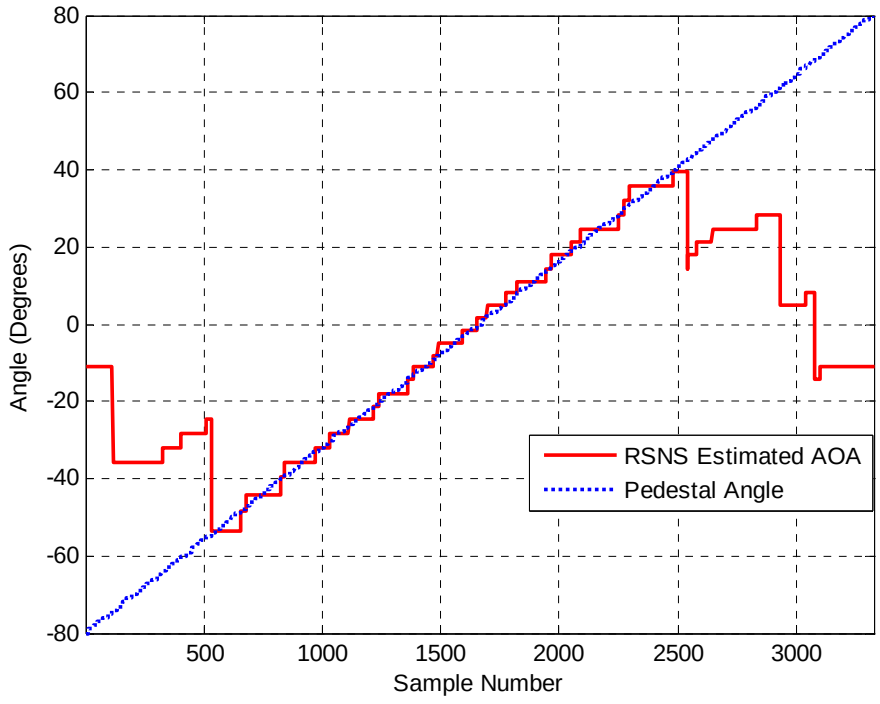

Figure 71. Tracking with RSNS mode using five phase differences (elements 1-2, 2-3, 3-4, 4-5, 5-6) and 1 degree steps.

The results are summarized and shown in Table 7. The one phase difference RSNS approach can provide a scan angle from the very beginning of -76.46°, but from 25° to 35.6° there is a region that is outside the angle error limitation. Within this region, monopulse tracking cannot acquire the signal and will point to an incorrect angle. The array may track in a sidelobe null instead of the mainlobe null.

The results show that the three phase differences RSNS approach (elements 1-2, 3-4, 5-6) can provide a wide FOV of 115°; although, it cannot provide a maximum continuous range like the other three phase differences (elements 2-3, 3-4, 4-5). It can, however, provide symmetric DF from -55° to 60°. The RMS errors are also the lowest at a range of -80° to 80° and -50° to 50°.

The five phase differences approach was expected to give the best results. However, the mutual coupling phase variation was much larger than expected for the edge elements, especially at wide angles. Therefore, it is proposed that it may be best to discard the data from the edge elements.

Table 7. Results of tracking with RSNS DF mode.

	One Phase Difference	Three Phase Differences	Three Phase Differences	Five Phase Differences
Phased Array Elements	3-4	1-2, 3-4, 5-6	2-3, 3-4, 4-5	1-2, 2-3, 3-4, 4-5, 5-6
Start Tracking Angle	–76.46°	–55°	–74°	–55°
End Tracking Angle	25°	60°	41.43°	42.53°
Maximum Continuous Tracking Range	101.46°	115°	115.43°	97.53°
RMS (–80° to 80°)	36.4173°	31.9450°	35.7984°	32.8421°
RMS (–70° to 70°)	16.8417°	19.5789°	26.5191°	22.0799°
RMS (–60° to 60°)	12.4996°	12.5066°	16.1248°	12.7128°
RMS (–50° to 50°)	10.5736°	6.2898°	12.3253°	7.2884°

The second tracking mode of the array (RSNS acquisition and monopulse DBF) was evaluated using one phase difference (elements 3-4), three phase differences (elements 1-2, 3-4, 5-6), three phase differences (elements 2-3, 3-4, 4-5) and five phase differences (elements 1-2, 2-3, 3-4, 4-5, 5-6) with 1 degree steps. The results are shown in Figures 72 to 75, respectively.

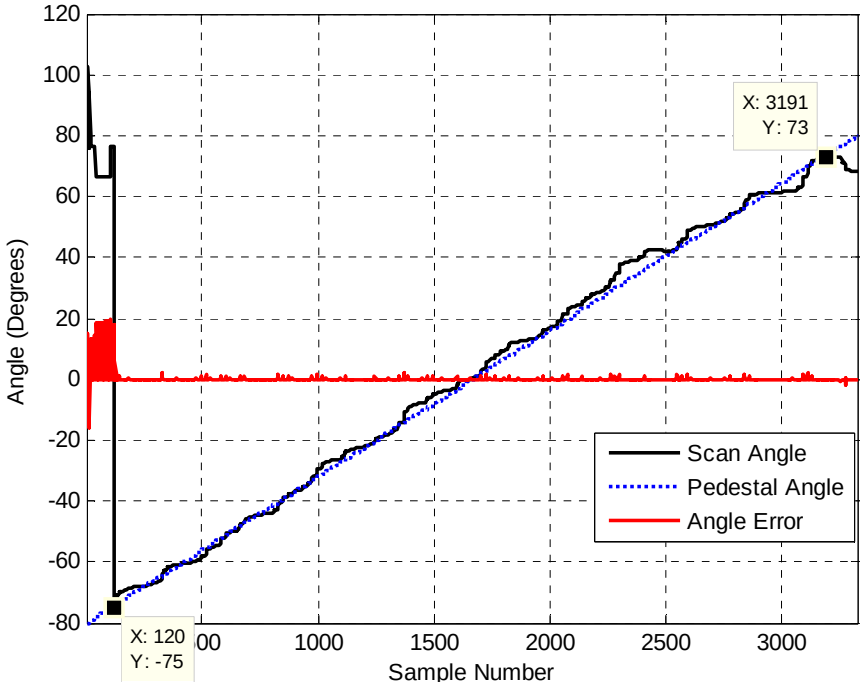

Figure 72. Tracking with RSNS and monopulse DBF mode using one phase difference (elements 3-4) and 1 degree steps.

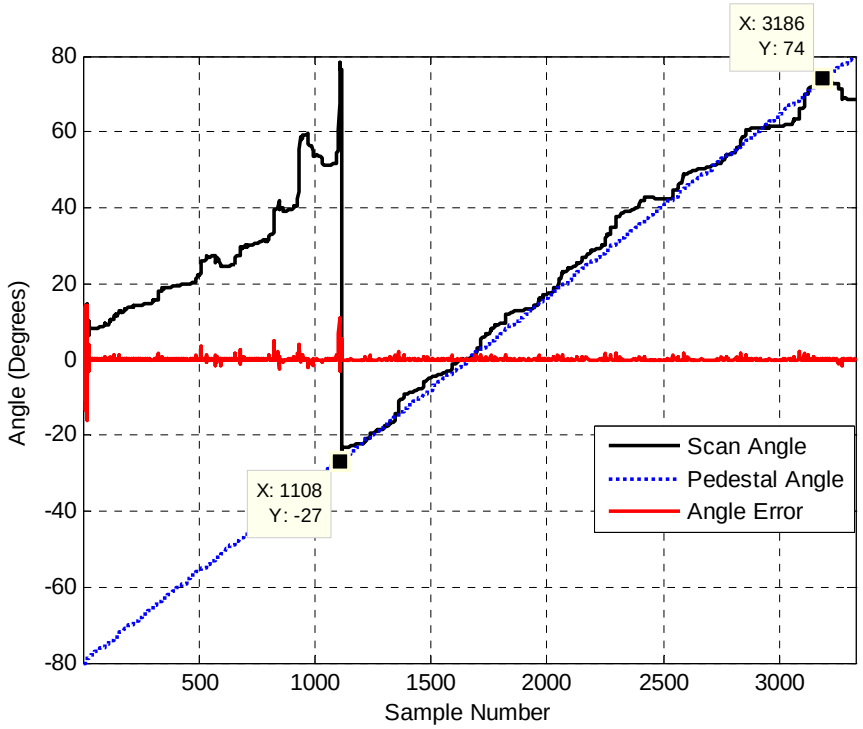

Figure 73. Tracking with RSNS and monopulse DBF mode using three phase differences (elements 1-2, 3-4, 5-6) and 1 degree steps.

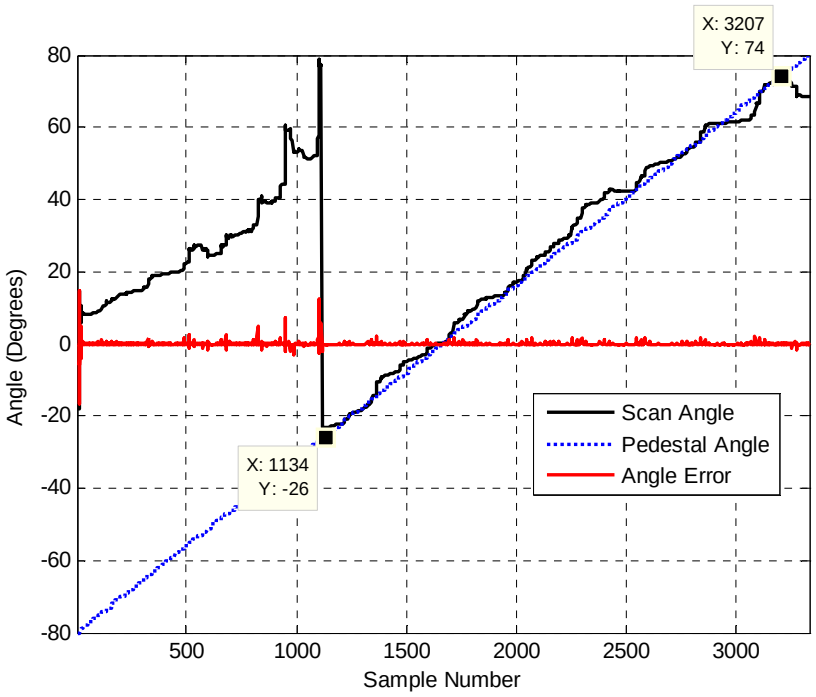

Figure 74. Tracking with RSNS and monopulse DBF mode using three phase differences (elements 2-3, 3-4, 4-5) and 1 degree steps.

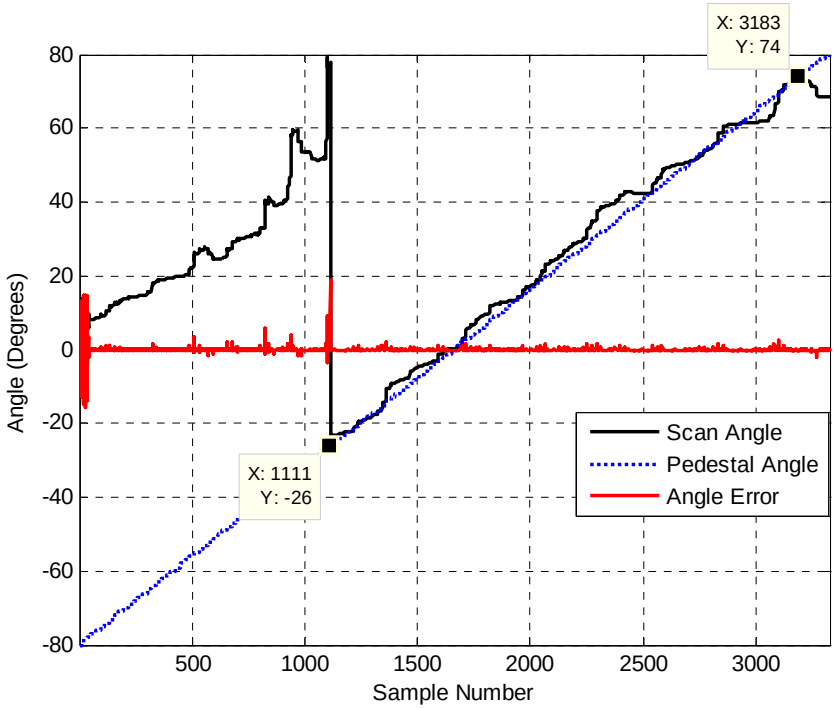

Figure 75. Tracking with RSNS and monopulse DBF mode using five phase differences (elements 1-2, 2-3, 3-4, 4-5, 5-6) and 1 degree steps.

The results are summarized and shown in Table 8. The initial scan angle is very important for the tracking system, as indicated by the test results. From the previous test, the one phase difference RSNS DF provided a correct scan angle from -76°, showing that monopulse tracking could implement tracking from the very beginning of a sweep. The results show that it could track from -75° to 73° and has a tracking range of 148°. On the other hand, the RSNS DF with other phase differences did not provide a correct scan angle in the beginning of the sweep and gave the monopulse tracker a wrong direction. The wrong direction is likely near a sidelobe null, so the tracker locks into the sidelobe null. It maintained the lock until around -26°, where the angle errors were over the limit or the SNR dropped. This forced the tracker to reacquire a new scan angle from the RSNS DF. At -26°, the RSNS provided a sufficiently accurate AOA.

The angle error displayed in the plots is the difference between the current scan angle and the new scan angle based on the most recent I and Q data. It is not the difference between the scan angle and pedestal angle.

The one phase difference has the best RMS errors performance from -80° to 80°, -50° to 80°, -20° to 80° and 10° to 80°, but the RMS differences are very close for track initiation angles larger than -20°. This is because all of the trackers can track signals after -26° and this should result in no significant difference.

Table 8. Results of tracking with RSNS and monopulse DBF mode.

	One Phase Difference	Three Phase Differences	Three Phase Differences	Five Phase Differences
Phased Array Elements	3-4	1-2, 3-4, 5-6	2-3, 3-4, 4-5	1-2, 2-3, 3-4, 4-5, 5-6
Start Tracking Angle	–75°	–27°	–26°	–26°
End Tracking Angle	73°	74°	74°	74°
Tracking Range	148°	101°	100°	100°
RMS (–80° to 80°)	28.8093°	46.9470°	46.6417°	46.7666°
RMS (–50° to 80°)	2.9305°	34.4132°	34.2354°	34.3468°
RMS (–20° to 80°)	3.2319°	3.2454°	3.2626°	3.2754°
RMS (10° to 80°)	3.5656°	3.5692°	3.5935°	3.6100°

The second series of tests required a change to some of the parameters and with an examination of the resultant performance. The five phase differences (elements 1-2, 2-3, 3-4, 4-5, 5-6) RSNS DF setup were used to test the effects of the movement of the pedestal. The pedestal step size was adjusted to 2°, 5° and 10°. This change in step size is equivalent to changing the update rate of the tracker. A larger step size simulates the UAV moving farther between samples. The results are shown in Figures 76 to 78.

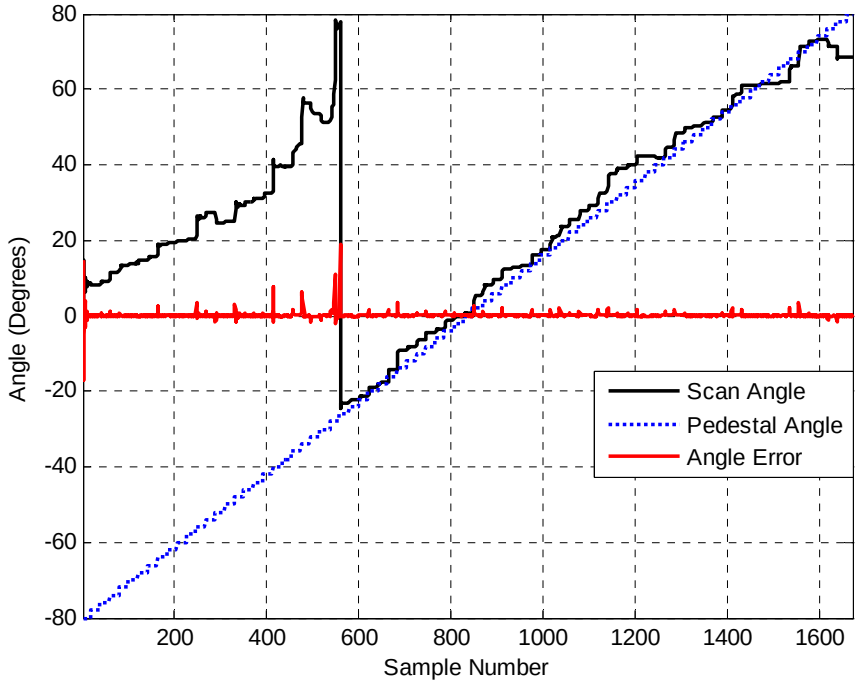

Figure 76. Tracking with RSNS and monopulse DBF mode using five phase differences (elements 1-2, 2-3, 3-4, 4-5, 5-6) and 2 degree steps.

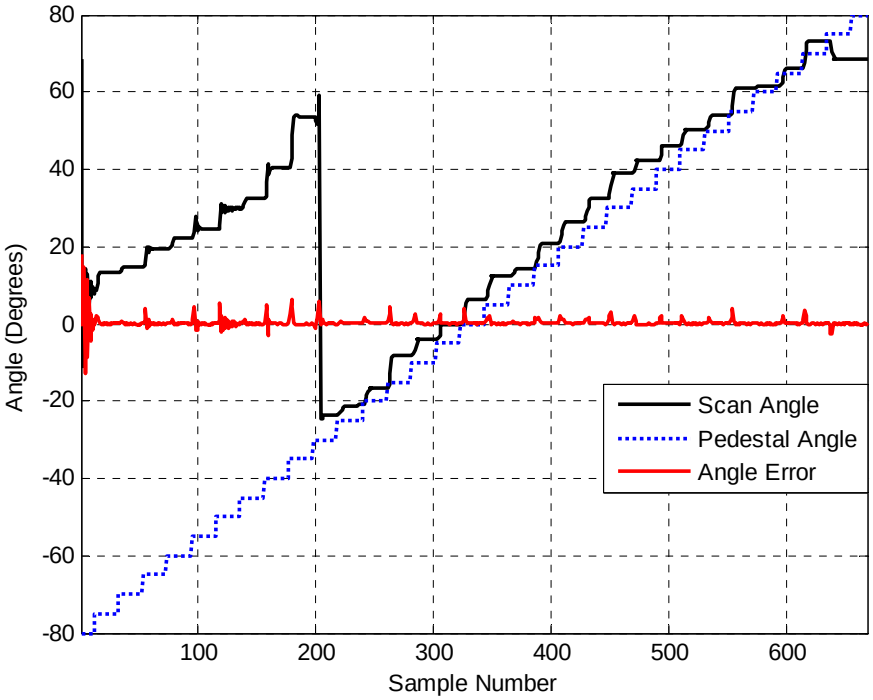

Figure 77. Tracking with RSNS and monopulse DBF mode using five phase differences (elements 1-2, 2-3, 3-4, 4-5, 5-6) and 5 degree steps.

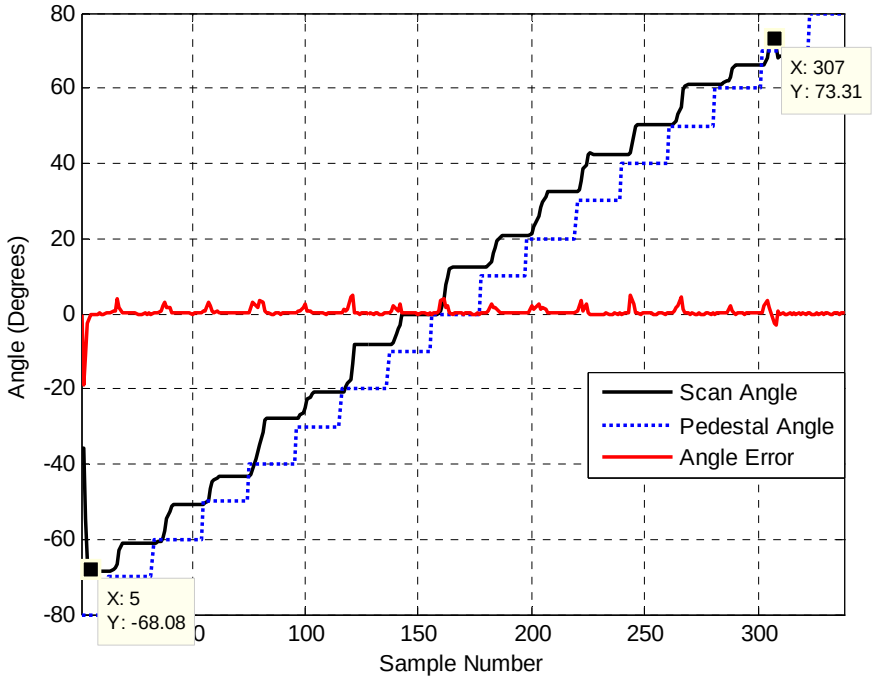

Figure 78. Tracking with RSNS and monopulse DBF mode using five phase differences (elements 1-2, 2-3, 3-4, 4-5, 5-6) and 10 degree steps.

There are two features that are noteworthy. First, increasing the step size of the pedestal also increases the angle error. Second, some of the angle errors are over the angle error limitation, forcing the monopulse tracker to reacquire the new scan angle from the RSNS DF. These effects can be seen in Figure 78. Essentially, the RSNS is used continuously and operates from -68.08° to 73.31°.

Another test was conducted by lowering the limitation of the angle errors from 20° to 10° and examining the results. The five phase differences (elements 1-2, 2-3, 3-4, 4-5, 5-6) RSNS DF were used for the test, and the pedestal was rotated in steps of 2°, 5° and 10°. The results are shown in Figures 79 to 81, respectively.

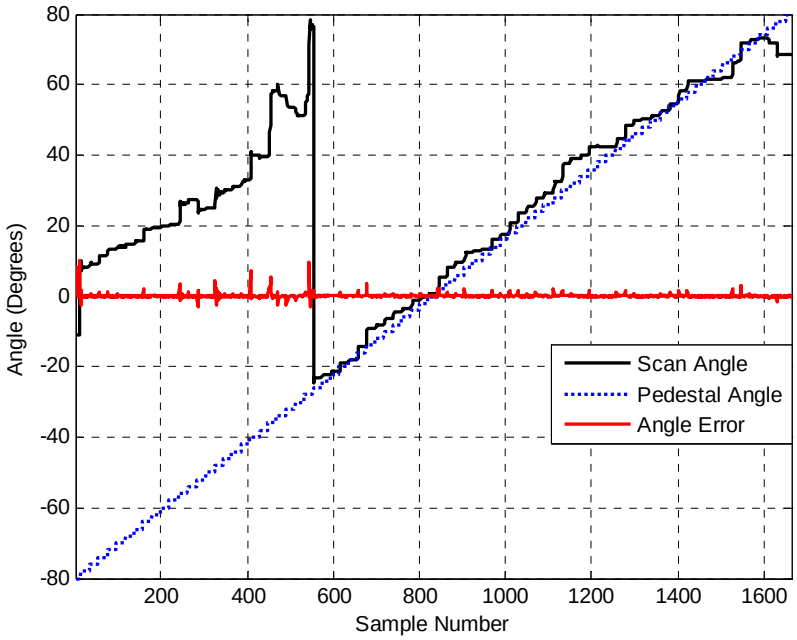

Figure 79. Tracking with RSNS and monopulse DBF mode using five phase differences (elements 1-2, 2-3, 3-4, 4-5, 5-6), 2 degree steps and 10° angle error limitation.

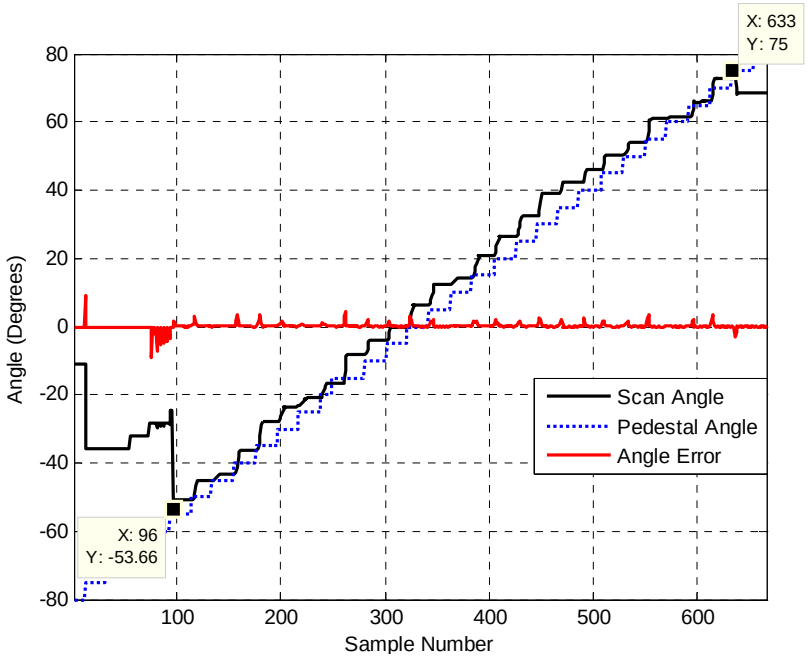

Figure 80. Tracking with RSNS and monopulse DBF mode using five phase differences (elements 1-2, 2-3, 3-4, 4-5, 5-6) , 5 degree steps and 10° angle error limitation.

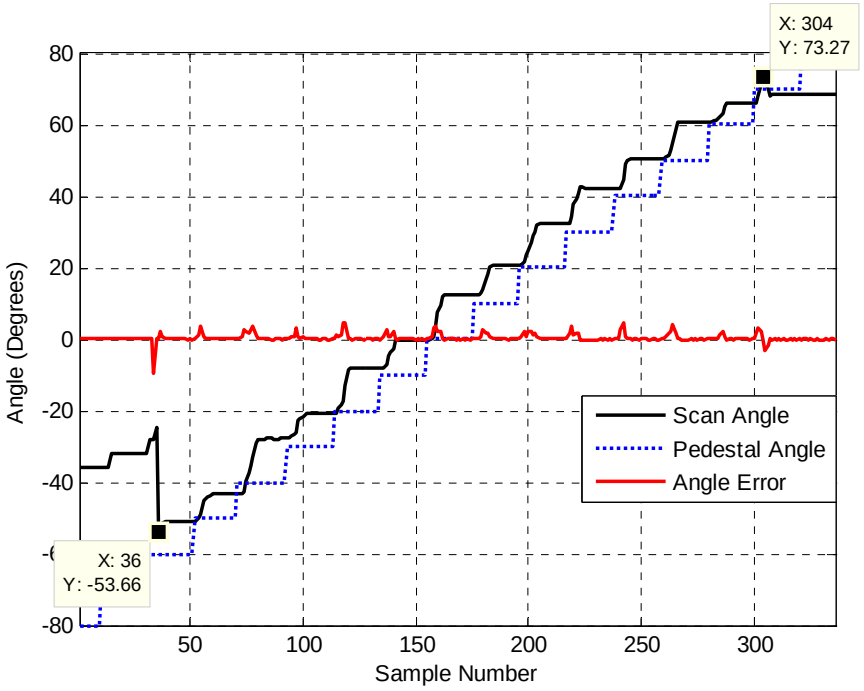

Figure 81. Tracking with RSNS and monopulse DBF mode using five phase differences (elements 1-2, 2-3, 3-4, 4-5, 5-6) , 10 degree steps and 10° angle error limitation.

With lowering of the angle errors from 20° to 10°, the results were the same as increasing the pedestal steps. The plots in Figures 80 and 81 show a track initiation angle around –53.66°, approximately 27° earlier than the 2 degree step case displayed in Figure 79.

Finally, the monopulse slope constant was fixed to -0.0822467, which was the slope constant at boresight. The results are compared to those for a slope constant that changes with the scan angle. The one phase difference (elements 3-4) and five phase differences (elements 1-2, 2-3, 3-4, 4-5, 5-6) RSNS DF were used for the test, and the pedestal was rotated by steps of 1°. The results are shown in Figures 82 and 83, respectively.

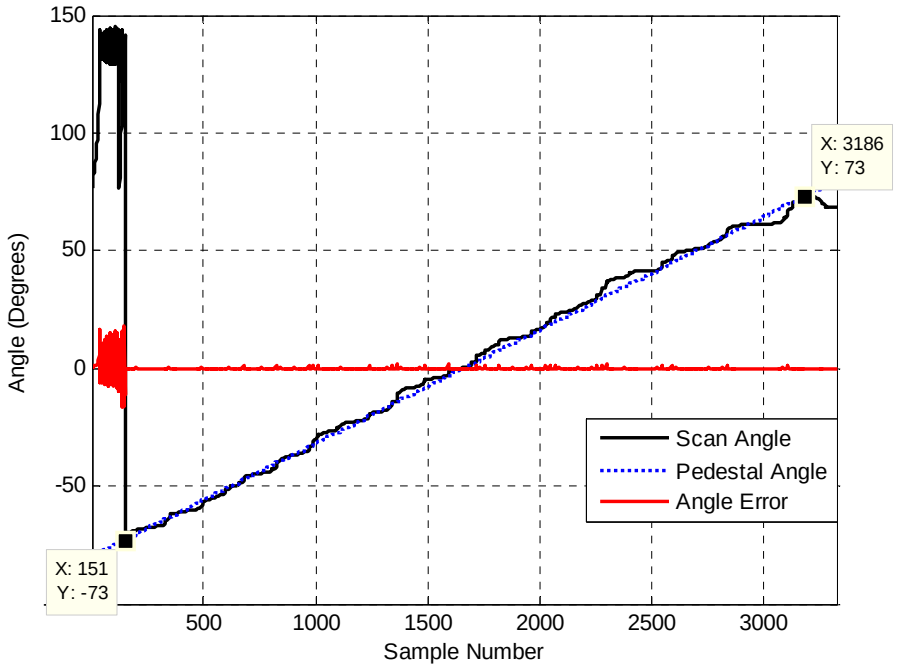

Figure 82. Tracking with RSNS and monopulse DBF mode using one phase difference (elements 3-4) , 1 degree steps and fix monopulse slope constant (-0.0822467).

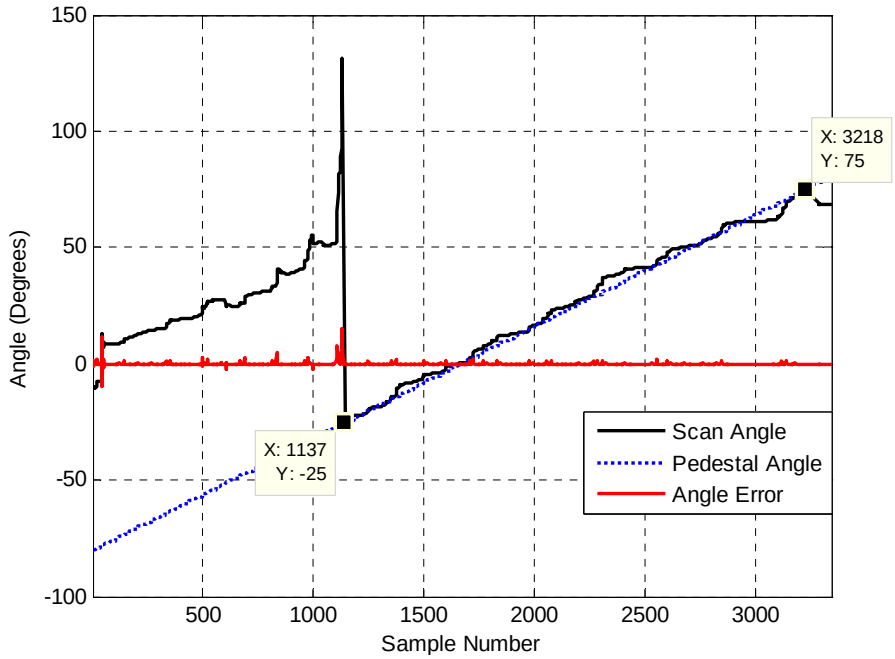

Figure 83. Tracking with RSNS and monopulse DBF mode using five phase differences (elements 1-2, 2-3, 3-4, 4-5, 5-6) , 1 degree steps and fix monopulse slope constant (-0.0822467).

The results were collected and are shown in Table 9. The improvement when the changing monopulse slope constant near the boresight is not significant. Some ranges such as 0° to 20°, 20° to 40° and 40° to 60° show that the fixed slope constant has better RMS errors than the variable slope constant. However, when the scan angle goes to 60° to 80°, the results show that the variable slope constant has better RMS errors.

Table 9. Results of tracking with RSNS and monopulse DBF mode.

	One Phase Difference	One Phase Difference	Five Phase Differences	Five Phase Differences
Phased Array Elements	3-4	3-4	1-2, 2-3, 3-4, 4-5, 5-6	1-2, 2-3, 3-4, 4-5, 5-6
Monopulse Slope Constant	Change with Scan Angles	Fixed	Change with Scan Angles	Fixed
Start Tracking Angle	-75°	-73°	-26°	-25°
End Tracking Angle	73°	73°	74°	75°
Tracking Range	148°	146°	100°	100°
RMS (0° to 20°)	2.1361°	2.0491°	2.1336°	2.0260°
RMS (20° to 40°)	4.1878°	3.4557°	4.2634°	3.3669°
RMS (40° to 60°)	1.7902°	1.6456°	1.8358°	1.6188°
RMS (60° to 80°)	4.7646°	5.1917°	4.6938°	5.1797°

VI. SUMMARY, CONCLUSIONS AND RECOMMENDATIONS

A. SUMMARY

This thesis is a continuation of the research addressed in references [8, 10, 11, 12]. The objective of this project was to design, build and test a six-element phased array using RSNS DF and monopulse DBF tracking. The tracking system should have the ability to accurately acquire transmitted signals from a UAV and track the video signal source continuously. There are two parts to this thesis. The first illustrates the RSNS DF algorithm and demonstrates the concept by hardware tests. The theory of the RSNS DF algorithm is explained in Chapter II and the hardware simulation in Chapter IV. The second portion examines angle tracking techniques, different types of tracking systems and implements the RSNS DF with monopulse DBF tracking system. The theory of the tracking system is described in Chapter III and the results of the tracking system demonstration are provided in Chapter V. The hardware components are COTS items to lower cost. Simulations are implemented in MATLAB, and the calibration, control, data acquisition and beamforming modules are built using LabView software.

The first task was to simulate and validate the RSNS algorithms used in DF. The implementation is for the single-channel RSNS DF system. The received baseband I and Q signals are recovered by direct downconversion demodulation. A bench top setup for the RSNS DF method is used to measure AOA and then do comparisons between the measured values and the true value (from the VNA). The analysis is performed to assess the impact of noise on the AOA estimates. Different SNRs from 10 dB to 90 dB in increments of 20 dB are examined to see which SNR values are acceptable for the DF accuracy.

The second task investigates angle tracking techniques, examines different types of tracking systems and implements the RSNS DF and monopulse DBF tracking algorithms. A six-element phased array was used for the tracking system demonstration. The hardware of the digital tracking array was assembled and tested. The tracking system uses RSNS DF to first find the rough AOA and then passes the scan angle to the

monopulse DBF module to do continuous tracking. The tracking measurements were taken in an anechoic chamber to reduce interference from multipath and the measured data are stored to do offline analysis. The first test was to find the maximum RSNS DF field-of-view for a variety of element phase differences (one phase difference, or averaging three phase differences or five phase differences). A FOV from -80° to 80° was tested. The second test examined the pedestal movement effects and rotation steps for 2°, 5° and 10°. Finally, the comparison of changing monopulse slope constant versus fixed monopulse slope constant is provided.

B. CONCLUSIONS

For the RSNS DF benchtop test, it was found that the resultant AOAs were in very close agreement with the known values computed from the measured phase difference. The results prove the single-channel RSNS DF system works properly and can be used to provide an initial AOA estimate for the monopulse tracking system.

A Monte Carlo simulation of the RSNS DF with SNRs from 10 dB to 90 dB showed that a SNR of approximately 30 dB is acceptable, and 30 dB is realistic for actual operations. For SNRs greater than 50 dB the performance is essentially ideal.

For the tracking part, the RSNS DF provides the monopulse DBF tracking system an initial AOA. Chamber measurements were presented for a range of operating parameters to examine their effects.

The first test determined the maximum RSNS DF FOV. A horn transmitter was used while the antenna was rotated in 1 degree steps. A variety of element phase differences (1 phase difference, or averaging 3 phase differences or 5 phase differences) were tested. The best results showed that a maximum continuous tracking range of 148° and a minimum RMS of 2.9305° was achieved using one phase difference.

Variations in the rotation rate and data collection rate were investigated. The five phase differences (elements 1-2, 2-3, 3-4, 4-5, 5-6) RSNS DF setup was used to test the effects of the movement of the pedestal. The pedestal was rotated with step sizes of 2°,

5° and 10°. This simulated a UAV moving farther between beamforming updates. This increased angle errors due to the additional latency in the system. More instances of large angle errors occurred, which forced the monopulse tracking to reacquire the new scan angle from the RSNS DF.

Finally, adding a variable monopulse slope constant was compared with the fixed monopulse slope constant. The improvement of the changing monopulse slope constant near the boresight was not significant. Some ranges such as 0° to 20°, 20° to 40° and 40° to 60° showed that the fixed slope constant had better RMS errors than the variable slope constant.

C. RECOMMENDATIONS FOR FUTURE WORK

There are several areas that need to be investigated to provide the tracking system better capabilities. One area is the effect of frequency drift between the source and local oscillator (LO) on performance. The current design is an open loop LO. The design does not work well because the frequency drift between the LO and the incoming signal causes a phase shift. One solution is to add a phased locked loop (PLL). The performance of such a tracking system could be simulated in MATLAB and then tested with a hardware build.

A second area of consideration is modification of the antenna to handle possible saturation conditions due to strong signals. Strong signals may come from a short operating range or high power transmission.

A third area for future work is embedding the pedestal rotation with the tracking module. For chamber measurements, the computer used to control the pedestal is not the same as the tracking computer. The pedestal rotation Sub-VI can be embedded into the tracking module so data logging can be automated.

THIS PAGE INTENTIONALLY LEFT BLANK

LIST OF REFERENCES

[1] "MQ-9 Reaper Hunter/Killer UAV," Available: http://defense-update.com/products/p/predatorB.htm. [Accessed October 17, 2010].

[2] "Unmanned aerial vehicle," October 14, 2010. [Online]. Available: http://en.wikipedia.org/wiki/Unmanned_aerial_vehicle. [Accessed October 17, 2010].

[3] Warren L. Stutzman and Gary A. Thiele, *Antenna Theory and Design,* 2nd edition, John Wiley & Sons, Hoboken, NJ, 1998.

[4] Merrill I. Skolnik, *Introduction to Radar Systems*, 3rd edition, McGraw-Hill, New York, NY, 2001.

[5] David C. Jenn, "Digital Antennas," Naval Postgraduate School, Monterey California, 2006 (unpublished notes).

[6] Merrill I. Skolnik, "Introduction to Radar Systems" 3rd Edition, pp. 248–266, McGraw-Hill, New York, NY, 2001.

[7] Toby Haynes, "A primer on digital beamforming," Spectrum Signal Processing, 1998.

[8] Berat Levent Gezer, "Multi-Beam Digital Antenna for Radar, Communications, and UAV Tracking Based on Off-The-Shelf Wireless Technologies," Master's Thesis, Naval Postgraduate School, Monterey, California, September 2006.

[9] Eng, Chun Heong, "Design and Development of an Automated Demodulator Calibration Station," Master's Thesis, Naval Postgraduate School, Monterey, California, December 2009.

[10] Jessica A. Benveniste, "Design and Development of a Single-Channel RSNS Direction Finder," Master's Thesis, Naval Postgraduate School, Monterey, California, March 2009.

[11] I-Hsiang Leslie Tan and Devieash James Pandya, "UAV Digital Tracking Array Design, Development and Testing," Master's Thesis, Naval Postgraduate School, Monterey, California, December 2009.

[12] Fevzi Aytac Kaya, "Development of a Receiver Processor for UAV Video Signal Acquisition and Tracking Using Digital Phased Array Antenna," Master's Thesis, Naval Postgraduate School, Monterey, California, September 2010.

[13] Anthony Lee, “Variable Resolution Direction Finding Using the Robust Symmetrical Number System,” Master’s Thesis, Naval Postgraduate School, Monterey, California, December 2006.

[14] David C. Jenn, “RSNS Processing Using a Single Channel,” Naval Postgraduate School, Monterey California, 2006 (unpublished notes).

[15] Simon Haykin and Michael Moher, *Introduction to Analog & Digital Communications*, 2nd edition, John Wiley & Sons, Hoboken, NJ, 2007.

[16] James H. Mcclellan, Ronald W. Schafer and Mark A. Yoder, *Signal Processing First*, 1st edition, Pearson Prentice Hall, Upper Saddle River, NJ, 2003.

[17] Jui-Chun Chen, “A Virtual RSNS Direction Finding Antenna System,” Master’s Thesis, Naval Postgraduate School, Monterey, California, December 2004.

[18] Anonymous, “AN/SPY-1D,” Available: http://pl.wikipedia.org/wiki/AN/SPY-1, accessed October 14, 2010.

[19] D. C. Jenn, “Microwave devices & radar,” vol. II, pp. 111–115, 2009 (unpublished lecture notes).

[20] Pace P. E., Wickersham D., Jenn D., and York N., “High Resolution Phase Sampled Interferometry Using Symmetrical Number Systems,” IEEE Transactions on Antennas and Propagation, Vol 49, No. 10, pp. 1411–1423, 2001.

[21] Kazimierz Siwiak and Yasaman Bahreini, *Radiowave Propagation and Antennas for Personal Communications*, 3rd edition, Artech House, Norwood, MA, 2007.

[22] D. C. Jenn, “Radio Propagation – Propagation near the Earth’s Surface,” pp. 2–10, 2010 (unpublished lecture notes).

[23] K.W. Kwai, P. E. Pace, D.C. Jenn, J. C. Chen, “Robust Symmetrical Number System Direction Finding Arrays With Virtual Spacing,” Naval Postgraduate School, Monterey California, 2004 (unpublished notes).

[24] David M. Pozar, *Microwave Engineering*, 3rd edition, John Wiley & Sons, Hoboken, NJ, 2005.

[25] D. C. Jenn, “Microwave devices & radar,” vol. III, pp. 34–102, 2010 (unpublished lecture notes).

[26] D. C. Jenn, “Approximate monopulse slope constant for a uniform array,” pp. 1–7, 2010 (unpublished handwritten notes).

INITIAL DISTRIBUTION LIST

1. Defense Technical Information Center
   Ft. Belvoir, Virginia

2. Dudley Knox Library
   Naval Postgraduate School
   Monterey, California

3. Chairman, Code EC
   Naval Postgraduate School
   Monterey, California

4. Professor David C. Jenn
   Department of Electrical and Computer Engineering
   Naval Postgraduate School
   Monterey, California

5. Professor Roberto Cristi
   Department of Electrical and Computer Engineering
   Naval Postgraduate School
   Monterey, California

6. Robert D. Broadston
   Department of Electrical and Computer Engineering
   Naval Postgraduate School
   Monterey, California

7. Professor Kevin Jones
   Department of Aeronautics and Astronautics
   Naval Postgraduate School
   Monterey, California

8. Professor Phillip E. Pace
   Department of Electrical and Computer Engineering
   Naval Postgraduate School
   Monterey, California

9. ShihYuan Yeh
   Department of Electrical and Computer Engineering
   Naval Postgraduate School
   Monterey, California